Carrier Transport in Auger-Suppressed Infrared Detector Materials

by

Justin Lavaughn Easley

A dissertation submitted in partial fulfillment
of the requirements for the degree of
Doctor of Philosophy
(Applied Physics)
in the University of Michigan
2019

Doctoral Committee:

Professor Jamie D. Phillips, Chair
Professor Pallab. K. Bhattacharya
Professor Rachel S. Goldman
Associate Professor Pei-Cheng Ku
Associate Professor Lu Li

Justin L. Easley

jleasley@umich.edu

ORCID iD: 0000-0001-5150-9817

© Justin L. Easley 2019

DEDICATION

To my parents.

ACKNOWLEDGMENTS

First, I would like to thank my advisor, Professor Jamie Phillips, for investing his time and energy into helping me develop as a young researcher throughout my time at the University of Michigan. He has been a mentor and a friend, and has pushed me to do great things while still respecting me as a person and a peer. There are many great researchers in the world, but I feel truly lucky to have been able to work alongside Professor Phillips, and if I had to do it all over again, I cannot see myself working for anyone else.

Second, I want to extend my thanks to my research collaborators at Teledyne Scientific and Imaging. Dr. Michael Carmody and his team gave me the opportunity to do research in a world class industry environment, allowed me to study very exciting material, and have provided support and guidance throughout my graduate career.

I would also like to thank my collaborators Martin Ettenberg and Chris Martin at Princeton Infrared Technologies Inc. for their trust in me on our projects, and for their guidance in navigating the world of III-V semiconductors.

Next, I would like to thank all of my research groupmates, both past and present. The conversations and discussions we've had throughout the years are one of the intangible aspects of my graduate career that I couldn't have survived without. Specifically, Dr. Chihyu (Jimmy) Chen and Dr. Alan Teran, thank you for showing me how to be a successful graduate student while balancing real life. To Hannah Masten,

Michael Barrow, and Eun Seong Moon, thank you for helping me out on my projects whevener possible, and for keeping the workplace fun and interesting.

I also want to thank all of my teachers and professors in the past who have motivated me, challenged me, and pushed me to be the scientist I am today. Specifically, I have to thank Dr. Charles Garner, my calculus teacher at the Rockdale Magnet School for Science and Technology, for supporting me and offering life advice and guidance, even to this day.

I would like to thank my wife, Ashley Easley, who has been supportive, patient, and understanding throughout my graduate career, all while striving for her own goals in her graduate career. I love you.

Finally, I would like to thank my family: my mother, Pamela, my father, Timothy, and my brother Cameron, who have supported me and cheered me on through every step of my school career. I would not be where I am without them, and I am very grateful to have all of you in my life. This thesis is dedicated to you.

.

TABLE OF CONTENTS

DEDICATION . . . . **ii**

ACKNOWLEDGMENTS . . . . **iii**

LIST OF FIGURES . . . . **ix**

LIST OF TABLES . . . . **xvi**

ABSTRACT . . . . **xvii**

CHAPTER

1 Introduction **1**

1.1 Background of IR Technology 1

1.2 IR Detector Basics 2

1.3 Performance Characteristics 8

1.4 Future direction of IR 11

2 Properties of HgCdTe **14**

2.1 MBE Growth of HgCdTe 14

2.1.1 Growth Defects 17

2.1.2 Point Defects 19

2.1.3 Doping 21

2.2 Electronic and Optical Properties 23
2.2.1 Band Structure 23
2.2.2 Effective Mass 25
2.2.3 Dielectric Constant 26
2.2.4 Electron Affinity 26
2.2.5 Intrinsic Carrier Concentration 26
2.2.6 Mobility 27
2.2.7 Optical Properties 29
2.2.8 Summary of Material Properties 31
2.3 Generation-Recombination Processes 31
2.3.1 Radiative Recombination 32
2.3.2 Shockley-Read-Hall Recombination 33
2.3.3 Auger Recombination 35

3 HgCdTe Device Technology 38
3.1 Standard HgCdTe Device Architectures 38
3.2 Rule 07 39
3.3 Auger Suppression 44
3.3.1 Non-equilibrium Devices 45
3.3.2 Barrier Detectors 47

4 HgCdTe Carrier Transport 49
4.1 Magnetotransport 49
4.1.1 Van der Pauw Method 49
4.1.2 Variable-Field Hall Effect 52
4.1.3 Multi-Carrier Fitting 53
4.1.4 Mobility Spectrum Analysis 56

4.2 Experimental Results . . . 60
4.2.1 Experimental Setup . . . 60
4.2.2 Initial MCF Experiments . . . 63
4.2.3 FMSA + MCF Experiments . . . 72
4.2.4 Mobility Analysis . . . 77
4.2.5 Quantum Hall Effect . . . 80

5 II-V T2SL Properties . . . 83
5.1 SWIR Technology . . . 83
5.1.1 InGaAs . . . 83
5.1.2 HgCdTe . . . 85
5.2 Development of Type II Superlattices . . . 87
5.2.1 InAs/GaSb based Superlattices . . . 89
5.3 SWIR Type II Superlattices . . . 91
5.4 T2SL Device Modeling . . . 94
5.5 InGaAs/GaAsSb T2SL Lattice Matched to InP . . . 96
5.5.1 Effective Bandgap . . . 96
5.5.2 Optical Absorption . . . 98
5.5.3 Carrier Transport . . . 102
5.5.4 Recombination Properties . . . 104
5.5.5 Dark Current Density . . . 106
5.5.6 Quantum Efficiency . . . 107
5.6 InGaAs/GaAsSb Strained-Layer Superlattice . . . 109
5.6.1 Strain Balance . . . 109
5.6.2 Desired SLS Structure . . . 112
5.6.3 Optical Absorption . . . 114

5.6.4 Quantum Efficiency 115

6 Conclusions and Future Work 117

Bibliography 122

LIST OF FIGURES

Figure 1.1 Electromagnetic spectrum, highlighting the infrared region ([1]) 2

Figure 1.2 Applications of Infrared Technology [2] 2

Figure 1.3 Infrared atmospheric transmission spectrum [3] 3

Figure 1.4 Band diagrams displaying a) Intrinsic absorption b) extrinsic absorption and c) intersubband absorption in a quantum well. (Based on [4]) 4

Figure 1.5 Schematic of a slab photoconductor device 5

Figure 1.6 Diagram of a p-n junction photodiode, as well as the corresponding band diagram and electric field profile. [2] 6

Figure 1.7 Current-Voltage characteristic of a p-n junction photodiode [2] 6

Figure 1.8 Diagram of a typical p-i-n photodiode. 7

Figure 1.9 Diagram of a HgCdTe focal plane array utilizing a) indium bump contacts or b) loophole interconnects. [5] 8

Figure 1.10 Diagram comparing detectivity as a function of wavelength of various materials (at the indicated temperature). The dashed lines also show the detectivity for an ideal photovoltaic, photoconductive, and thermal detector. [2] 11

Figure 1.11 Diagram comparing the operating temperature of various infrared devices, as well as the cooling technologies required to reach the desired temperature. ([6] 12

Figure 2.1 Pressure - Temperature diagram for growth of $Hg_{1-x}Cd_xTe$ bulk growth [9] 15

Figure 2.2 Comparison of growth conditions among bulk and epitaxial HgCdTe growth methods [2] 17

Figure 2.3 Diagram of optimal growth temperature ranges for MBE growth of HgCdTe [9] 18

Figure 2.4 Relationship between measured 77K hole concentration and the partial pressure of Hg, *P(Hg)*, at various annealing temperatures. [10] 20

Figure 2.5 Table displaying various elements and whether they act as donors or acceptors. From [11] 21

Figure 2.6 Relationship between arsenic diffusion coefficients and Hg partial pressure for MWIR and LWIR HgCdTe. From [7] 23

Figure 2.7 Band structure for HgTe, HgCdTe, and CdTe near the center of the Brillouin zone. Bandgap, curvature, and valence band offset are all displayed for each material. [**?**] 24

Figure 2.8 Band gap energy, E_g, and Cutoff wavelength, λ_c, as a function of CdTe mole fraction for 77K and 300K. Lattice constant variation is also displayed. [6] 25

Figure 2.9 Mobility as a function of temperature for n-type HgCdTe as a sum of alloy, ionized impurity, neutral impurity, and optical phonon scattering. [8] 29

Figure 2.10 Summary of the various material properties of $Hg_{1-x}Cd_xTe$ at various compositions. Also included are properties of HgTe and CdTe binary alloys. [6] 31
Figure 2.11 Diagram of the most probable Auger recombination pathways [12] 35

Figure 3.1 Diagram of a typical HgCdTe P-on-n planar heterojunction photodiode [2] 39
Figure 3.2 Comparison between Rule 07 empirical model and other measured HgCdTe photodetectors. Also included are typical InGaAs and InSb detectors. [13] 42
Figure 3.3 Radio of Rule 07 predicted dark current to background radiation limited dark current as a function of λ_c. [13] 43
Figure 3.4 Predicted dark current densities from Rule 07 and Auger 1 recombination. [14] 43
Figure 3.5 Depiction of the carrier density in a P-on-n photodiode in a) zero bias condition and b) reverse bias condition. [15] 46
Figure 3.6 Ratio of Auger-suppressed dark current to Auger recombination current as a function of temperature and absorber level doping density. [15] 47
Figure 3.7 Device architecture of a nBn photodetector, both under reverse bias and at flat band condition. [16] 48

Figure 4.1 Diagram depicting charge build-up in bulk material, resulting in the observation of an effective Hall voltage, V_H. [17] 50
Figure 4.2 Common contact geometries for van der Pauw measurements [18] 51

Figure 4.3 Hall coefficient as a function of magnetic field in HgCdTe. The sign of the Hall coefficient changes sign around 0.1T, indicating the presence of both electrons and holes. [19] 53
Figure 4.4 Plot of conductivity tensor components, σ_{xx} and σ_{xy} vs magnetic field for a representative HgCdTe sample 55
Figure 4.5 Flow chart of the FMSA iteration process. [20] 58
Figure 4.6 Plot of total error, χ^2, as a fucntion of the total number of FMSA iterations. The spikes correspond to increases in the mobility spectral resolution, and the total error converges at a value near $\chi^2 = 10^{-5}$. 59
Figure 4.7 Sample mobility spectrum fit to synthetic data with two electron and two hole species. [20] 60
Figure 4.8 A standard device structure for MBE-grown HgCdTe, with a low doped, narrow bandgap absorber layer and a higher doped, wide bandgap buffer and cap layer. [8] 61
Figure 4.9 Diagram of a Hall bar sample geometry. 62
Figure 4.10 Multi-carrier fits to σ_{xx} and σ_{xy} for two HgCdTe samples at 77K. [21] 64
Figure 4.11 a) Carrier concentration versus temperature data for sample L1.b. b) Mobility versus temperature data for sample L1.b [21] 66
Figure 4.12 a) Carrier concentration versus temperature data for sample H1. b) Mobility versus temperature data for sample H1 [21] 69
Figure 4.13 FMSA fit to measured σ_{xx} and σ_{xy} data for a representative HgCdTe sample [8] 73

Figure 4.14 Mobility spectra for a representative sample taken at two different temperatures (175K and 77K). The two primary electron peaks correspond to the buffer and absorber layers, and a significant low mobility hole peak is also present. [8] 74
Figure 4.15 a) Carrier density vs reciprocal temperature and b) mobility versus reciprocal temperature [8] 76
Figure 4.16 Mobility for LWIR HgCdTe with x=0.209 and $N_d = 4 \times 10^{13}$ cm^2/Vs based on alloy, ionized impurity, neutral impurity, and optical phonon scattering. [8] 79
Figure 4.17 Comparison between measured mobility values, empirical model in Equation 4.22, and theoretical scattering model. [8] 80
Figure 4.18 Calculated band diagram for low-doped, LWIR HgCdTe absorber layer on top of wide gap, HgCdTe buffer layer. 2DEG formation is possible at the interface at 3 μm. [8] 81
Figure 4.19 Measured resistance vs magnetic field at $T = 500mK$. [8] . . . 82
Figure 5.1 a) Quantum efficiency as a function of wavelength and b) Dark current as a function of bias voltage for standard SWIR InGaAs focal plane array [22] 84
Figure 5.2 Tie diagram displaying lattice constant of InGaAs at various compositions, compared to lattice constant of InP 85
Figure 5.3 Plot of Lattice Constants and Coefficient of Thermal Expansion (CTE) for various materials that have been considered as alternative substrates. [23] 86
Figure 5.4 Plot of dark current density and quantum efficiency for HgCdTe/Si with $\lambda_c = 2.67\mu m$ fabricated into FPAs with a 30 μm pitch. [24] . . . 87

Figure 5.5 Band alignment for a standard InAs/GaSb superlattice. [25] . 88
Figure 5.6 Dispersion relation comparison between bulk HgCdTe (a) and a strained InAs/InGaSb superlattice (b). [26] 90
Figure 5.7 Comparison of carrier lifetime mechanisms in a) MWIR HgCdTe which is dominated by SRH recombination and b) LWIR HgCdTe which is dominated by Auger recombination [27] 92
Figure 5.8 a) Quantum efficiency and b) dark current density of a InGaAs/GaAsSb type-II superlattice focal plane array with 200 μm diamater pixels. [28] 94
Figure 5.9 Standard device structure for simulating InGaAs/GaAsSb Type-II superlattice infrared detectors. Buffer and Cap layers are comprised of $In_{0.53}Ga_{0.47}As$, all grown on an InP substrate. [29] 95
Figure 5.10 Band structure of the of 5 nm $In_{0.53}Ga_{0.47}As$/5 nm $GaAs_{0.51}Sb_{0.49}$ superlattice, displaying the lowest hole and higest electron energy level, as well as wavefunctions. The associated effective bandgap is 0.494 eV, corresponding to a cutoff wavelength of $\lambda_c = 2.51\mu$ m. [29] 97
Figure 5.11 Calculated Energy dispersion relation for 5 nm $In_{0.53}Ga_{0.47}As$/5 nm $GaAs_{0.51}Sb_{0.49}$ T2SL. 98
Figure 5.12 Absorption coefficient vs. wavelength diagram for 5 nm $In_{0.53}Ga_{0.47}As$/5 nm $GaAs_{0.51}Sb_{0.49}$ T2SL. Steps in the spectrum correspond to optical transitions between electron and hole energy levels. [29] 100
Figure 5.13 Absorption coefficient vs. wavelength diagram including InGaAs, HgCdTe and InGaAs/GaAsSb T2SL. 101
Figure 5.14 Diagram of various carrier transport mechanisms in a Type-II superlattice. 102

Figure 5.15 Minority carrier lifetime vs temperature including Auger, Radiative, and Shockley-Read-Hall recombination contributions. $\tau - SRH$ is plotted as a function of trap density, N_T [29] 105
Figure 5.16 Dark current density vs inverse temperature including Shockley-Read-Hall and radiatively limited Type-II superlattices, extended range $In_{0.83}Ga_{0.17}As$, and the Rule 07 prediction for $\lambda_c = 2.2\mu m$ [29, 30] . . . 107
Figure 5.17 Quantum efficiency vs wavelength for 5 nm $In_{0.53}Ga_{0.47}As$/5 nm $GaAs_{0.51}Sb_{0.49}$ T2SL and $Hg_{0.51}Cd_{0.49}Te$ [29] 108
Figure 5.18 Tie diagram depicting the necessary changes for InGaAs and GaAsSb compositions in order to create a strained layer superlattice . 111
Figure 5.19 Allowed composition combinations for InGaAs/GaAsSb SLS with various layer thicknesses. 112
Figure 5.20 Calculated band diagram for 5 nm $In_{0.50}Ga_{0.50}As$ / 6 nm $GaAs_{0.49}Sb_{0.51}$ SLS system with $\lambda_c = 2.58\mu m$. 113
Figure 5.21 Calculated absorption spectrum for 5 nm $In_{0.50}Ga_{0.50}As$ / 6 nm $GaAs_{0.49}Sb_{0.51}$ SLS system with $\lambda_c = 2.58\mu m$. 114
Figure 5.22 Critical thickness versus GaSb composition in $GaAs_{1-x}Sb_x$. Horizontal lines indicate SLS layer thicknesses. 115
Figure 5.23 Quantum efficiency vs wavelength for the 5 nm $In_{0.50}Ga_{0.50}As$ / 6 nm $GaAs_{0.49}Sb_{0.51}$ SLS system. The quantum efficiency near the cutoff is significantly higher than in the similar, unstrained T2SL case. 116

LIST OF TABLES

Table 4.1 Comparison of MCF results alongside van der Pauw, 4-point Hall effect measurements for 3 different anneal conditions. [21] 71

Table 4.2 Comparison between Van der Pauw, FMSA, and MCF results for a representative low doped HgCdTe sample. [8] 75

ABSTRACT

State of the art infrared detectors can operate at high efficiency and low noise throughout the infrared wavelength range. However, MWIR and LWIR detectors are still limited by very low operating temperatures in order to achieve low noise, and SWIR detectors are either prohibitively expensive or limited to small wavelength ranges.

Mercury cadmium telluride (HgCdTe, or MCT) with low n-type indium doping concentration offers a means for high performance infrared detection in the mid-wave and long-wavelength range. Characterizing carrier transport in materials with ultra low doping ($N_D = 10^{14}$ cm^{-3} and lower), as well as multi-layer material structures designed for infrared detector devices, is particularly challenging using traditional Van der Pauw Hall methods. Hall effect measurements with swept magnetic field were used in conjunction with a multi-carrier fitting procedure and Fourier-domain mobility spectrum analysis (FMSA) to analyze multi-layered MCT samples. Using low temperature measurements (77 K), we were able to identify multiple carrier species, including an epitaxial layer (x = 0.2195) with n-type carrier concentration of n = 1×10^{14} cm^{-3} and electron mobility of μ = 280,000 cm^2/Vs. The extracted electron mobility matches or exceeds prior empirical models for MCT, illustrating the outstanding material quality achievable using current epitaxial growth methods, and motivating further study to revisit previously published material parameters for MCT carrier transport. The high material quality is further demonstrated via observation

of the quantum Hall effect at low temperature (5 K and below).

For short-wave absorption, type II superlattices (both lattice matched and strained) based on $In_{0.53}Ga_{0.47}As/GaAs_{0.51}Sb_{0.49}$ grown on InP substrates were simulated and investigated for short wavelength infrared detection. Eight band $k{\cdot}p$ simulations were utilized to extract information on the electronic band structure, which were in turn used to calculate the optical absorption spectrum of the superlattice. The effective band gap is calculated, and cutoff wavelengths greater than 2 μm were observed. Quantum efficiency was calculated for a standard InGaAs/T2SL/InGaAs p-i-n device structure, where quantum efficiency exceeding 50% at 2 μm may be achieved. Dark current was calculated considering Auger, radiative, and Shockley-Read-Hall generation-recombination, where Shockley-Read-Hall recombination-generation was found to be the limiting mechanism for a trap density greater than 5×10^{14} cm^{-3}, and radiatively limited performance is predicted for a lower trap density. The estimated dark current density is expected to be comparable to existing HgCdTe technology, while outperforming extended-range InGaAs by more than an order of magnitude.

The work outlined in this thesis provided some of the first evidence that low doping levels and high mobilities in HgCdTe devices could be measured electrically in a multilayer structure, which helped to pave the way for Auger-suppressed detectors. The high mobility and early evidence of quantum Hall effects (at temperatures as high as 4K) indicate HgCdTe is a great candidate for future QHE experiments. Also, the work on both lattice matched and strained superlattices provide a roadmap and methodology for future SWIR superlattice detector design.

Chapter 1

Introduction

1.1 Background of IR Technology

Infrared (IR) light refers to photons whose wavelengths on the electromagnetic spectrum range from $\tilde{7}00$nm (the end of the visible light region) to 1 mm (microwave radiation) (Fig 1.1). IR detectors are devices designed to interact with photons within the infrared range. The infrared range is of particular interest in a variety of applications, as the longer wavelengths (compared to visible light) allow for radiation to be transmitted for longer distances without significant attenuation. Modern applications for IR technology include commercial and scientific uses, such as wireless communications, ground and space based astronomy, and medical imaging, as well as military applications in night vision, thermal imaging, and missile guidance and detection. A variety of different types of infrared detector technologies are employed across this range of applications (Figure 1.2).

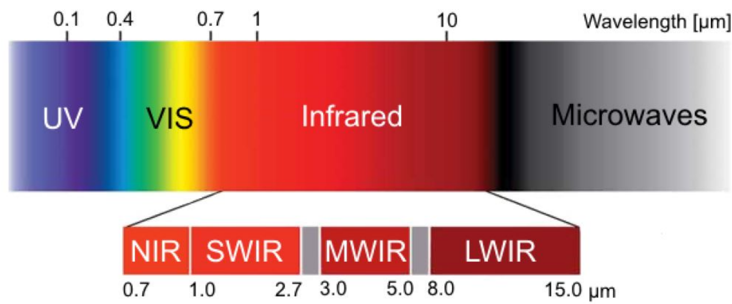

Figure 1.1: Electromagnetic spectrum, highlighting the infrared region ([1])

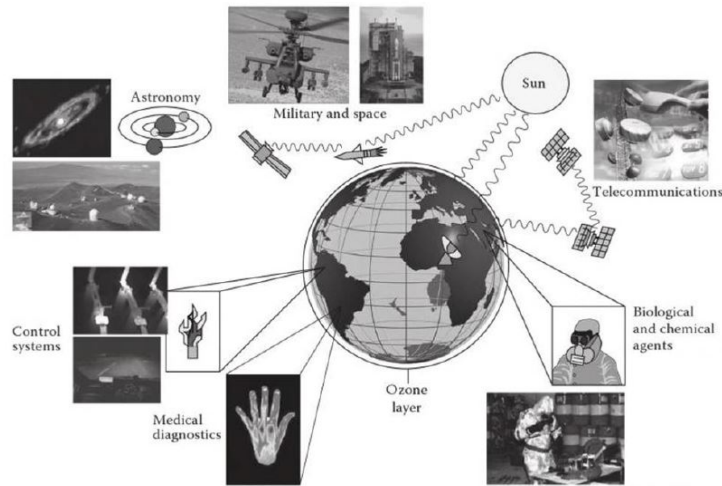

Figure 1.2: Applications of Infrared Technology [2]

While detectors can be designed to absorb infrared radiation of any potential wavelength, only certain wavelength ranges are possible for propagation through air. Water and other molecules in the atmosphere will absorb nearly 100% of infrared radiation of certain energies (Fig 1.3), so transmission is typically defined in three major regions: Short-wave (SWIR) from 1-3 μm, Mid-wave (MWIR) from 3-5 μm, and Long-wave infrared (LWIR) from 8-14 μm. Each region has a different set of competing technologies for high performance operation.

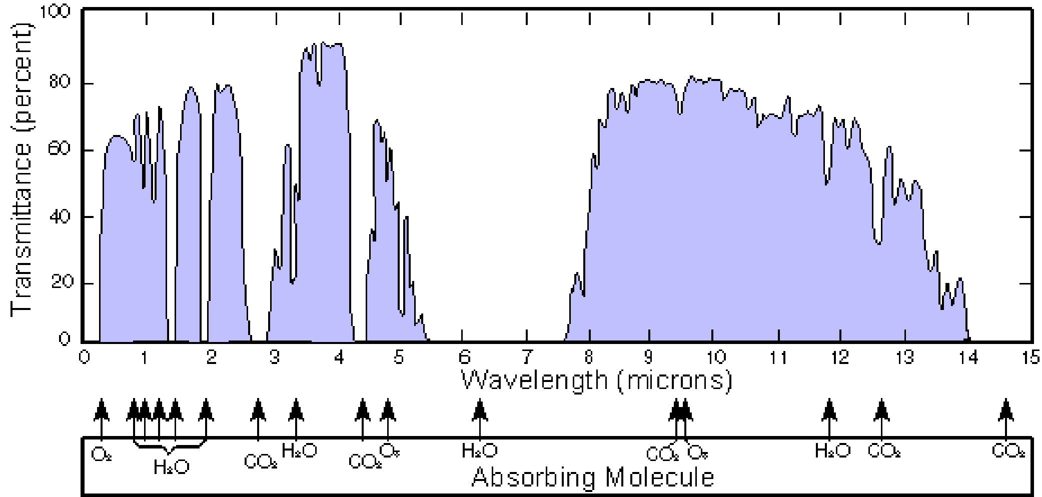

Figure 1.3: Infrared atmospheric transmission spectrum [3]

1.2 IR Detector Basics

Historically, infrared energy was first observed by the use of thermometers and bolometers in the 1800s that measured temperature changes from objects that radiated in the IR [6]. These early thermal detectors operated by measuring material properties that changed with a proportional increase in temperature, such as electrical conductivity (bolometers) or thermoelectric effects (thermocouples). These detectors (made from Pb, Se or Bi, or other binary compounds) operated with high sensitivity, but no spectral information could be extracted. Many thermal infrared technologies exist are still in use today due to the fact that they can easily operate near room temperature and can be manufacturated easily, but high performance detectors that require spectral sensitivity operate via converting absorbed photons into electrical current. [6]

The other primary type of IR detectors are photon detectors. Absorbed photons are converted into electrons and holes via photogeneration. Since absorption can only occur at certain allowed energies (as determined by the band structure of the mate-

rial) photon detectors can also give spectral information about the incident light. In a semiconductor material, the lowest possible allowed energy (and maximum possible wavelength) of light that can be absorbed is typically equal to the band gap energy, E_g, unless there are possible energy states within the forbidden band gap. The maximum wavelength is referred to as the cutoff wavelength, λ_c. Below that cutoff, the absorption strength at a particular wavelength is specific to each material, and the full absorption spectrum is useful for determining how well a material can convert incident photons into photocurrent, also known as the material's efficiency, η.

There are multiple types of photon absorption methods utilized for IR detection. Intrinsic (or direct bandgap) absorption is common in materials such as InSb, PbSe, InGaAs, and HgCdTe, where infrared light is absorbed at or near the bandgap energy. Extrinsic detectors, such as Silicon or Germanium doped with arsenic, indium, or sulfur, can absorb light at energies below the bandgap by exciting electrons to and from deep level trap states, and are often used for very long wavelength detection. Quantum well detectors are a specific type of extrinsic detectors that absorb light at energies corresponding to intersubband transitions within a quantum well structure. They can have various band alignments, and the most common materials are HgTe/CdTe and InAs/GaSb based. A schematic comparing the various methods of absorption is shown in Figure 1.4. [31]

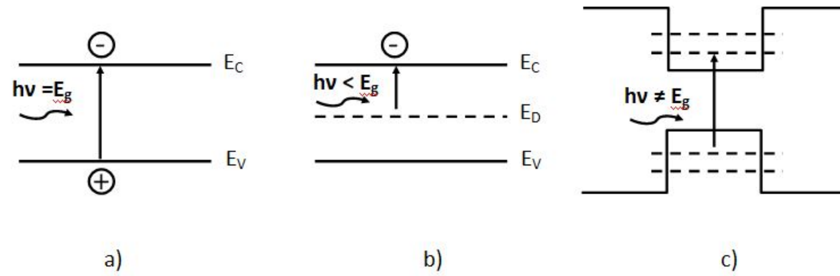

Figure 1.4: Band diagrams displaying a) Intrinsic absorption b) extrinsic absorption and c) intersubband absorption in a quantum well. (Based on [4])

There are two main types of photon detectors in use today, photoconductors (PC) and photodiodes [4]. Photoconductors are the simpler of the two devices, and they operate by measuring a change in conductivity of a material in the presence of light. The absorbed light will crease electron-hole pairs in the exposed area, increasing the number of free carriers, and thus the conductivity. If a photoconductor is held at a particular bias, the resulting change in current due to photogeneration can be observed (Fig 1.5)

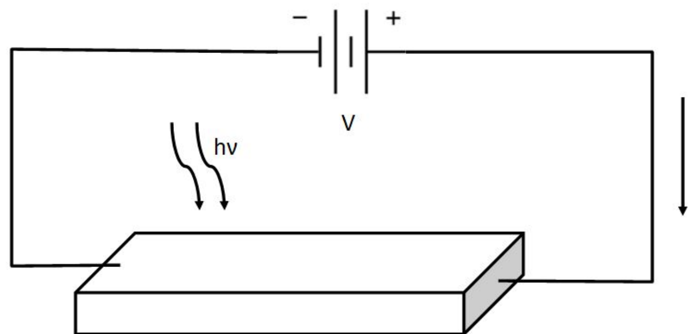

Figure 1.5: Schematic of a slab photoconductor device

Photodiodes, in constrast to photoconductors, are diodes with a material interface

between a p-type and n-type semiconductor (p-n junction). Homojunction diodes are comprised of the same semiconductor material with regions of different doping, and heterojunction diodes have an interface between two different materials. Current in an standard diode follows the ideal diode equation,

$$I = I_0 \left(e^{\frac{qV}{k_B T}} - 1 \right) \tag{1.1}$$

where V is the applied voltage bias. [32] In forward bias (V $>$ 0), the current increases exponentially with voltage, and in reverse bias (V $<$ 0), the current is equal to I_0, also referred to as the dark current. For use as a photodiode, these devices are typically operated under reverse bias conditions, and when no light is incident on the detector, the only current flowing is the dark current. When light of appropriate wavelengths hits the detector, electron-hole pairs are generated , which can be swept across the p-n junction and out to the contacts to create a photogenerated current. Figures 1.6 and 1.7 show a schematic of a standard, p-n junction photodiode, as well as the I-V characteristic.

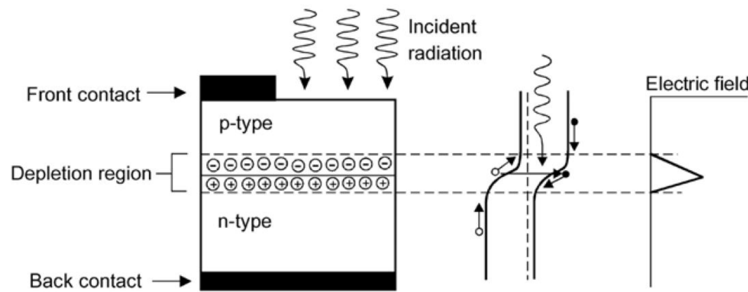

Figure 1.6: Diagram of a p-n junction photodiode, as well as the corresponding band diagram and electric field profile. [2]

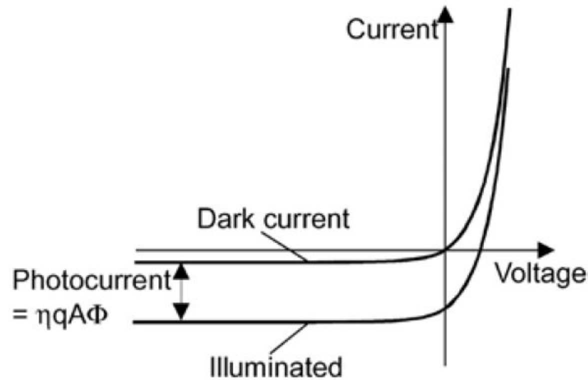

Figure 1.7: Current-Voltage characteristic of a p-n junction photodiode [2]

There are two important photodiode architectures that will be considered. The first is a P-on-n planar heterojunction. This is common in HgCdTe photodetectors, where substrate purity and lattice mismatch are common issues, and it is difficult to grow intrinsic material. A wide bandgap, transparent buffer layer is first grown on top of the substrate to prevent impurities and defects from spreading into the active region of the device. A wide bandgap, n-type cap layer is grown on top of the active layer, and the p-n junction is formed via ion implantation since p-type HgCdTe is difficult to grow accurately via common epitaxy techniques. This structure is physically similar to the general structure in Figure 1.6, with the n-type side being significantly thicker than the p-type implant region.

The second important device architecture is the p-i-n (or PIN) photodiode. These are common in III-V detectors, such as InGaAs on InP. In a traditional p-n junction diode, light is absorbed all throughout the device. However, only carriers that are created within the depletion region surrounding the junction (and within a diffusion length from the depletion region) can be swept away to the contacts and collected as current, as all other carriers will recombine before they reach the junction. Adding

an intrinsic region between the p-type and n-type layers can increase the measured photocurrent because a very small bias is necessary to fully deplete the intrinsic region, effectively creating a much larger total depletion region [4]. A diagram of this type of photodetector is shown in Figure 1.8.

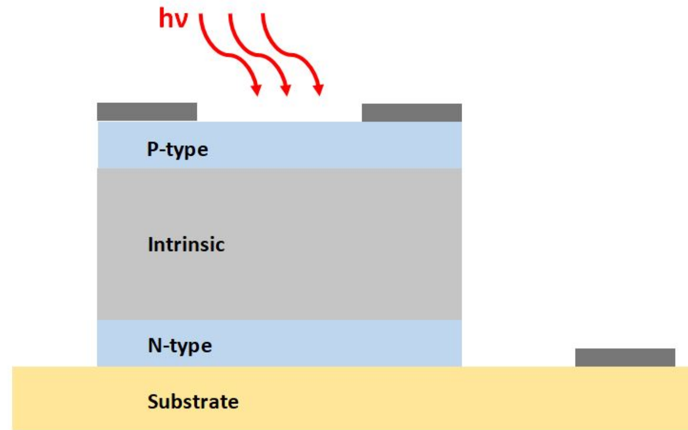

Figure 1.8: Diagram of a typical p-i-n photodiode.

A common method to employ IR detectors in practice is to utilize a focal plane array (FPA). FPAs will utilize multiple detectors at a time by treating each contact on a detector as a pixel, similar to a camera. A schematic of a FPA structure is shown in Figure 1.9. A large area epitaxially grown detector structure is constructed, then an array of contacts (often in the form of metallic bumps) are patterened, which are then connected to a read-out integrated circuit (ROIC) [5]. Focal plane arrays, when combined with wavelength filters, can be used for scanning and imaging applications, such as space telescopes or night vision, and are the most common application for many high performance infrared devices.

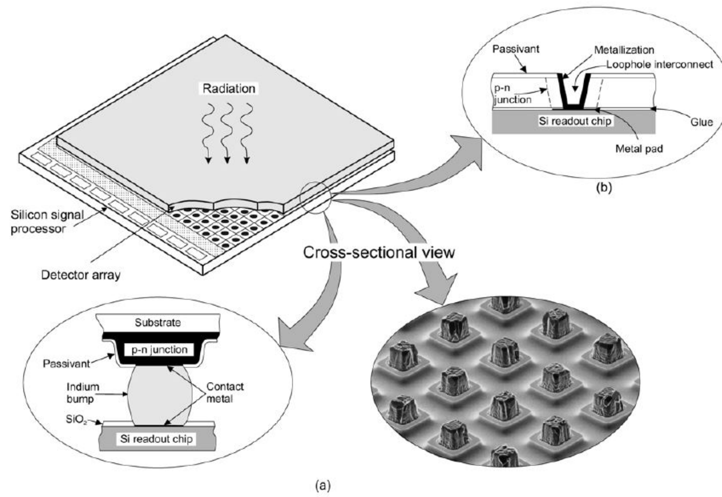

Figure 1.9: Diagram of a HgCdTe focal plane array utilizing a) indium bump contacts or b) loophole interconnects. [5]

1.3 Performance Characteristics

As described in the previous section, infrared detectors can operate in a variety of different ways utilizing a wide range of different materials. In order to compare various detectors and determine which are best suited for a particular application, there are a few characteristics and figures of merit that can be measured. The responsivity and quantum efficiency detail the total amount of signal that is created in a detector. The dark current is a measure of the amount of noise that is inherently present, and the detectivity gives a ratio of the signal to noise ratio.

Responsivity is commonly defined as the current response to an incident input power, and has units of A/W (amps per Watt) [31]. Similarly, the quantum efficiency, or QE, is a ratio that determines the number of electon/hole pairs created per photon incident on a device. Various expressions and models for these parameters will be described in later chapters. Both of these metrics define the capacity for a device to

convert photons into signal, which is critical to ensure that enough signal is present to surpass the noise floor.

The dark current density of the diode (as described in Section 1.2) is the amount of current flowing in a reverse biased photodiode when no light is incident on the detector. In order to measure small signals, a device needs to have a very low dark current density. There multiple forms of generation and recombination that can be limiting to a device's dark current, including Auger, radiative, and Shockley-Read-Hall recombination. A general expression for the dark current density, J_D is given by

$$J_D = \frac{qWn_i}{\tau_0} \tag{1.2}$$

$$\frac{1}{\tau_0} = \frac{1}{\tau_{Auger}} + \frac{1}{\tau_{Rad}} + \frac{1}{\tau_{SRH}} \tag{1.3}$$

where W is the depletion region width in the diode, n_i is the intrinsic carrier concentration, and τ_0 is the average minority carrier lifetime. Expressions for these lifetimes will be explored for the relevant material systems in future chapters.

The best comparison metric for devices is the detectivity, D^*. Detectivity is a measure of the normalized signal to noise ratio of the device, as a function of wavelength, and it is given by [31]

$$D^* = \frac{\eta}{2h\nu}\left(\frac{1}{G_{th} + \Phi_B}\right)^{1/2} \tag{1.4}$$

where η is the quantum efficiency, h is Planck's constant, ν is the frequency of light, G_{th} is the thermal generation rate, and Φ_B is the incident background radiation flux. Figure 1.10 [2] shows a comparison of the detectivity of a wide variety of detectors as

a function of wavelength. Thermal detectors and photoconductors have a much lower D^* than photovoltaic devices (such as photodiodes). Also, this chart illustrates what materials have the highest possible performance in certain wavelength ranges. In the SWIR range, InGaAs and HgCdTe are the top performers, in the MWIR range, InAs, InSb, and HgCdTe are relevant, and in the LWIR, HgCdTe outperforms all other materials.

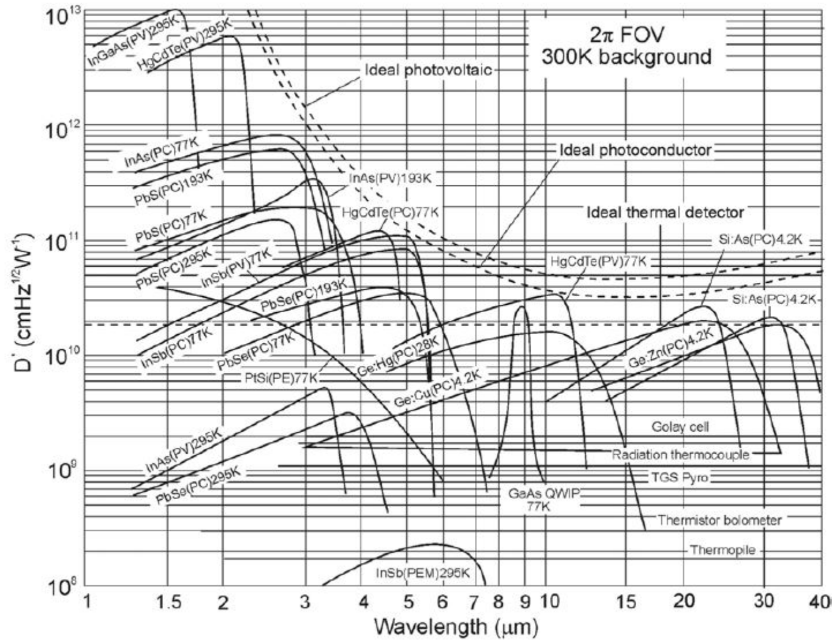

Figure 1.10: Diagram comparing detectivity as a function of wavelength of various materials (at the indicated temperature). The dashed lines also show the detectivity for an ideal photovoltaic, photoconductive, and thermal detector. [2]

While the previous metrics are strictly related to device performance, another practical parameter is the operating temperature of the device. This can be seen on Figure 1.10, where short wave detectors have a higher operating temperature than longer wavelength and thermal detectors. At higher operating temperatures, more carriers are thermally generated in the active region of a device. In order to measure a

photogenerated current, you must have a minimum intensity of incident light to create more carriers than are thermally generated, thus the defined operating temperature is the maximum temperature that a IR device can operate while still maintaining a high detectivity. Since longer wavelengths correspond to smaller bandgap energies, LWIR devices have much lower operating temperatures, since less thermal energy is required in order to excite carriers above the bandgap.

1.4 Future direction of IR

Current research in infrared detector systems has one primary goal: to bring the overall cost of infrared material systems down. Simpler thermal detectors are relatively cheap, as they can be fabricated from bulk silicon or germanium, and can often be operated near room temperature. Higher performance detectors not only have much more expensive fabrication methods (via molecular beam epitaxy (MBE) or other chemical vapor deposition (CVD) techniques), but also must have associated cooling systems in order to reach cryogenic temperatures for long wavelength devices.

One primary area of constant research for LWIR devices is development of high operating temperature (HOT) devices. Figure 1.11 shows a summary of the cooling systems required to reach certain operating temperatures. There are a variety of approaches that researchers are taking to drive the operating temperature of devices up, including lowering the doping concentration to suppress Auger recombination ([15], [21], [8]), introducing quantum well structures [33], [34] and other novel device architectures such as nBn barrier devices [35], [36]. By reducing cooling requirements, detectors can move from costly cryogenic systems to simpler and cheaper thermoelectric (TE) cooling methods.

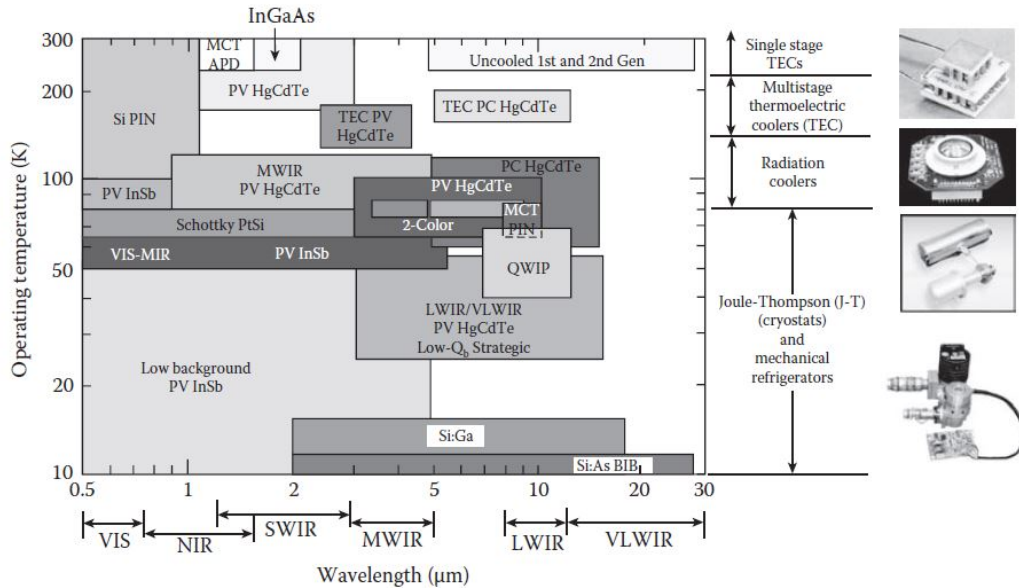

Figure 1.11: Diagram comparing the operating temperature of various infrared devices, as well as the cooling technologies required to reach the desired temperature. ([6]

The other research area related to reducing cost is introducing novel device architectures to compete with traditional materials. Quantum well infrared photodetectors (QWIPs) made from GaAs/AlGaAs were originally introduced in order to compete with HgCdTe, primarily in the LWIR region. InAs/GaSb superlattice detectors have predicted dark current density values that are orders of magnitude lower than the lowest realized in HgCdTe devices. Resesarch is also being conducted into other III-V superlattice detectors to compete in the SWIR and MWIR regions as well. If expensive HgCdTe detectors can be replaced with cheaper, III-V technology that utilizes cheaper substrates and more mature growth technology, significant cost savings can be realized.

The focus of the work presented in the upcoming chapters is to provide an experimental demonstration low doping levels necessary for Auger suppression in LWIR

detectors, and a theoretical prediction for new, cost effective device structures to compete with the existing high performance SWIR detector market. Chapters 2 and 3 will describe the material properties and device technology utilized for HgCdTe detectors, with a focus on LWIR detection and parameters relevant for observing Auger suppression. Chapter 4 describes magnetotransport experiments utilized to observe low doping and high mobility values that are important for high operating temperature (HOT) devices. Chapter 5 details relevant parameters for SWIR detectors, with a focus on existing superlattice detector technology. This chapter finishes with theoretical predictions for performance of type-II superlattice detectors. Overall, this study provides evidence of exceeding previous boundaries in HgCdTe, and provides a roadmap for similar progress in SWIR superlattice detectors.

Chapter 2

Properties of HgCdTe

2.1 MBE Growth of HgCdTe

Mercury Cadmium Telluride has historically been grown with a variety of bulk and epitaxial methods. In the 1960s and 1970s, bulk growth techniques, such as solid state recrystallization(SSR) and the Bridgman method were among the predominant growth methods [9]. They required high temperatures (> 700C) and high Hg pressures (up to 100 atm) (see Fig 2.1), and it was not possible to produce high quality heterostructures. While a handful of groups may still use bulk growth methods for photoconductors, they have been largely replaced with epitaxial growth methods.

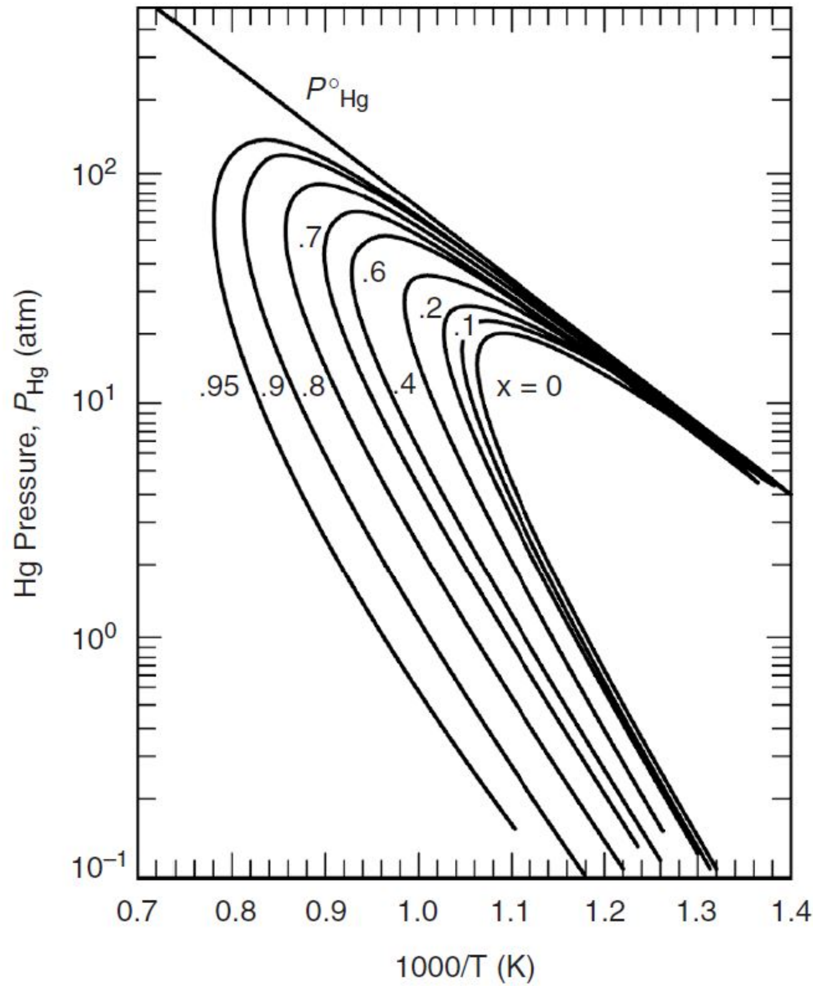

Figure 2.1: Pressure - Temperature diagram for growth of $Hg_{1-x}Cd_xTe$ bulk growth [9]

There are three modern epitaxial growth methods in use today: Liquid phase epitaxy (LPE), metal organic chemical vapor deposition (MOCVD), and molecular beam epitaxy (MBE). Liquid phase epitaxy was developed in the 1970s as a replacement for the bulk methods. It can be achieved using either a Te or Hg melt solution with dissolved Cd to control composition. Growth temperatures are much lower (350-550C), and large area growth is possible. However, LPE has issues with defects related to

morphology and lattice matching, making complex multi-layer architectures difficult. Regardless, LPE is still widely used for HgCdTe growth today, but high performance detectors are traditionally growth using vapor phase epitaxial methods. [37]

MOCVD is the primary competitor for MBE with regards to growth of high performance MCT. It has a higher growth rate than MBE (up to 10 μm/hr), instrument maintenance is simpler and faster, and more flexibility exists when changing source and reactor configurations. A major drawback is that CdZnTe substrates can not be used for MOCVD due to higher growth temperatures (280-350C) that allow for impurities to migrate from the substrate into the epitaxial MCT layer. Thus, GaAs or Si substrates with CdTe buffer layers are used, which leads to dislocations related to the lack of lattice matching. [9]

MBE growth of HgCdTe takes place under ultra-high vacuum conditions (10^{-6} Torr or lower) in order to minimize background contaminants and reduce scattering and collisions between source atoms. Beams of these atoms are directed toward a heated substrate. These atoms are physically adsorbed to the substrate, and move along the surface in a self-assembly process. The substrate temperature is set to be high enough to allow sufficient thermal energy for atoms to propagate along the surface, but these temperatures are typically below 200C, which minimizes interdiffusion of atoms within the substrate and grown layers. The sublimation process is slow (with a deposition rate of 1-3 monolayers/second) which allows for layers to grow epitaxially, while also allowing precise control of the device stoichiometry. Abrupt composition changes can be obtained by opening and closing shutters on the effusion cells, allowing for heterojunction formation and complex device structures to be realized. These factors give MBE an advantage over other modern growth techniques with regard to high quality material, a summary of which can be seen in Figure 2.2.

	Bulk						
		Travelling heater method		Liquid phase epitaxy		Vapour phase epitaxy	
	SSR	HCT melt	Te melt	Hg melt	Te melt	MOCVD	MBE
Temperature (°C)	950	950	500	350–550	400–550	275–400	160–200
Pressure (Torr)	150 000	150 000	760–8000	760–11 400	760–8000	300–760	10^{-3}–10^{-4}
Growth rate (μm h^{-1})	250	250	80	30–60	5–60	2–10	1–5
Dimensions w (cm)	0.8–1.2 dia	0.8–1.2 dia	2.5 dia	5	5	7.5 dia	7.5 dia
l (cm)	—	—	—	6	5	4	4
t (cm)	15	15	15	0.0002–0.0030	0.0005–0.012	0.0005–0.001	0.0005–0.001
Dislocations (cm^{-2})	$<10^5$	—	$<10^5$	$<10^5$	$<10^5$–10^7	5×10^5–10^7	$<5 \times 10^4$–10^6
Purity (cm^{-3})	$<5 \times 10^{14}$	$<5 \times 10^{14}$	$<5 \times 10^{14}$	$<5 \times 10^{14}$	$<5 \times 10^{14}$	$<1 \times 10^{15}$	$<1 \times 10^{15}$
n-type doping (cm^{-3})	N/A	N/A	N/A	1×10^{14}–1×10^{18}	1×10^{15}–1×10^{16}	5×10^{14}–5×10^{18}	5×10^{14}–1×10^{19}
p-type doping (cm^{-3})	N/A	N/A	N/A	1×10^{15}–1×10^{18}	1×10^{15}–5×10^{16}	3×10^{15}–5×10^{17}	1×10^{16}–5×10^{18}
X-ray rocking curve (arc sec)	—	—	20–60	<20	<20	50–90	20–30
Compositional uniformity (Δx)	<0.002	<0.004	<0.005	<0.002	<0.002	±0.01–0.0005	±0.01–0.0006

Figure 2.2: Comparison of growth conditions among bulk and epitaxial HgCdTe growth methods [2]

The HgCdTe layers utilized in the experiments detailed in Chapter 4 were grown via MBE at Teledyne Imaging Sensors in Camarillo, CA. I spent months training at their fabrication facility, studying growth methods on their Riber 32P MBE systems. Growths were typically conducted on the slower side of the possible growth rates (1-3 μm/hr) in order to have very precise control over composition and temperature throughout the growth. The fabrication details and electrical properties of layers similar to those I helped to produce are described in [38].

2.1.1 Growth Defects

Effusion cells containing raw material sources are heated to cause sublimation of atoms and create a controllable material flux. HgCdTe growth utilizes solid CdTe and Te_2 sources, as well as a liquid Hg source. Required growth temperatures are lower than other growth methods, but must be controlled very precisely. Optimal growth temperature is between 185 and 190C. The sticking coefficient of Hg is very low compared to Cd and Te, so small variations in temperature of just a few °C can lead to significant fluctuations of composition and defect densities. If the temperature is too low, excess Hg can accumulate on the surface, which produces microtwin defects

that can affect electrical properties. If the temperature is too high, not enough Hg is present, and void defects can begin to form. A summary of the relevant growth conditions can be seen in Fig 2.3 [9].

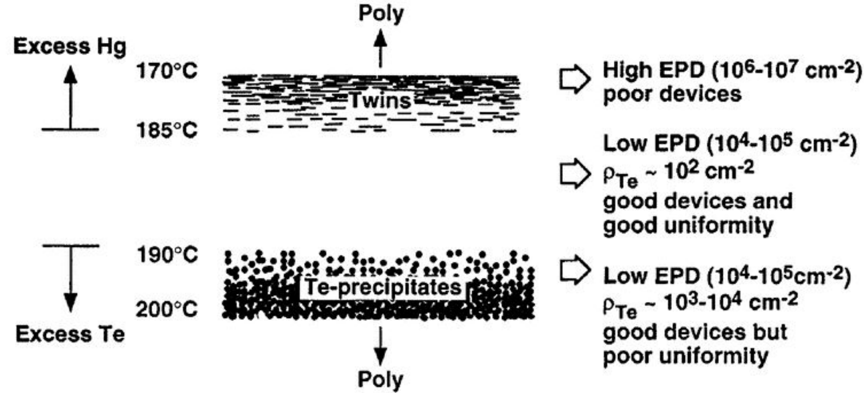

Figure 2.3: Diagram of optimal growth temperature ranges for MBE growth of HgCdTe [9]

MCT requires a very narrow growth window in order to achieve high quality material. Many measurements are made *in situ* in order to verify the growth is proceeding properly. An infrared pyrometer is used to verify and maintain a constant substrate temperature throughout the growth. Reflection-high-energy electron diffraction (RHEED) is used to monitor surface crystallinity, which can also detect the presence of microtwin defects. In order to measure composition to within ±0.002%, spectroscopic ellipsometry is used to monitor the stoichiometry at the surface. [39,40]

After the growth is completed, other characterization techniques include Fourier-transform infrared spectroscpy (FTIR) in order to measure final thickness and layer composition [41], and etch pit density (EPD) measurements to quantify defect densities. EPD measurements can assess the number of microtwin and void defects present near the surface [9], as well as threading dislocations caused by strain relaxation in lattice mismatched layers (such as the substrate/epilayer and heterojunction inter-

faces). [42, 43] To perform an EPD measurement, HgCdTe layers are dipped in a chemical etchant of $NHO_3/K_2Cr_2O_7/HCl/H_2O$, and the density of visible etch pits is counted. A quality layer typically has a $10^4 - 10^5$ EPD count, while lower quality material can range as high as 10^6 [9].

2.1.2 Point Defects

Other defects that can be present in HgCdTe include various types of point defects that occur by omissions or replacements of individual atoms at lattice points. The most important of these are vacancies that can occur during growth. Cation site vacancies occur when there is a missing Cd or Hg atom. Although both a lack of Cd and Hg can lead to a cation vacancy, the enthalpy needed to form a Hg vacancy is lower than that for a Cd vacancy (for x = 0.2, enthalpy = 2.2 eV for Hg and 4.7 eV for Cd) [10]. Thus, any cation vacancy is historically referred to as a Hg vacancy.

Mercury vacancies in as grown, updoped MCT act as acceptors, causing the material to be p-type. The number of vacancies, and also the associated hole concentration, can be described by the partial pressure of the mercury, *P(Hg)*. Post growth, a mercury overpressure thermal anneal is employed to drive more Hg atoms into the vacant sites. Figure 2.4 shows the relationship between *P(Hg)* and hole concentration. A high pressure, low temperature anneal is sufficient for bringing down the as grown hole concentration.

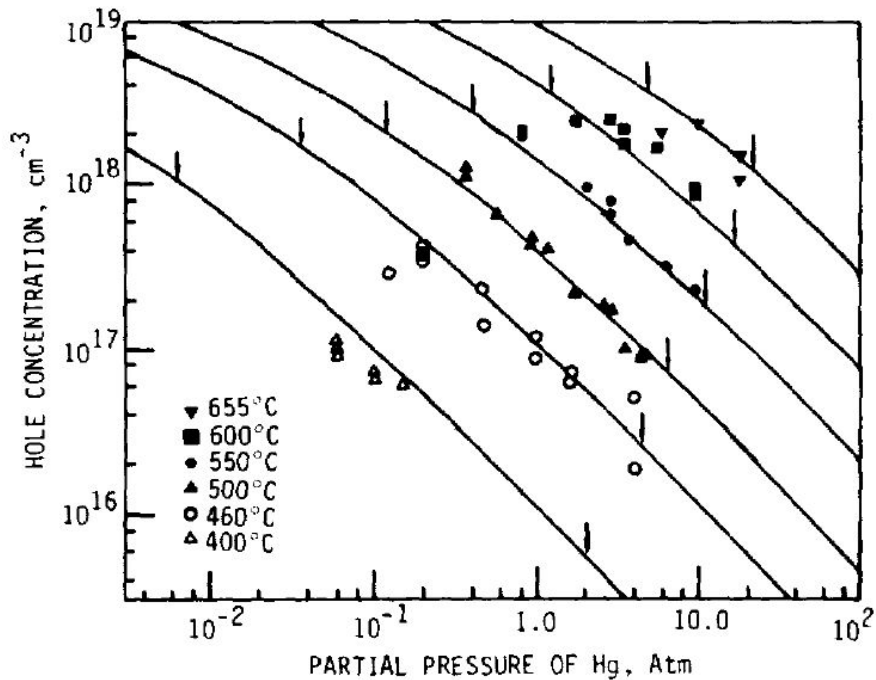

Figure 2.4: Relationship between measured 77K hole concentration and the partial pressure of Hg, *P(Hg)*, at various annealing temperatures. [10]

Another defect that occurs in Tellerium based materials are Te precipitates. They can form in Te rich environments at high temperatures, and are commonly formed during the cool down process after initial preperation and growth. These can also be eliminated during a thermal anneal with Hg overpressure [44]. These precipiates are thought to be SRH trap centers which can increase the dark current in MCT diodes [12]

Background impurities are another important source of defects that can affect electrical performance. Figure 2.5 shows a list of elements and whether they act as donors or acceptors in HgCdTe. Impurities like copper and gold can diffuse from the CdZnTe substrate into the epitaxial layer. In as-grown material, Hg vacancies can compensate for small concentrations of background n-type dopants, although

this leads to reduced overall mobility [9]. Once a Hg anneal has been completed on undoped HgCdTe to reduce Hg vacancies, the material is then type converted to n-type due to these background impurities. This background doping level is not explicitly controllable, and leads to difficulty when attempting to achieve low n-type doping levels in epitaxial HgCdTe [11].

Element	Group	Expected behaviour	Actual behaviour				
			LPE (Hg)	LPE (Te)	MOVPE (Hg)	MOVPE (Te)	MBE (Te)
H	IA	A(m)		A			
Li	IA	A(m)		A			A
Rb	IA	A(m)		I			
Cu	IB	A(m)	A	A			A
Ag	IB	A(m)	A			A	A
Au	IB	A(m)	A				
Zn	IIB	I(m),D(i)	I	I			
B	IIIB	D(m)		D			
Al	IIIB	D(m)	D	D		I/D	D
Ga	IIIB	D(m)	D	D		D	
In	IIIB	D(m)	D	D	D	D	D
Tl	IIIB	D(m)	D				
Si	IVB	D(m),A(t)		D?		D	D
Ge	IVB	D(m),A(t)	D				
Sn	IVB	D(m),A(t)	D?			D	
P	VB	A(t)		I(A)	A	I	
As	VB	A(t)	A	I(A)	A	I	D/A
Sb	VB	A(t)	A	I(A)	A	I/D	D
Bi	VB	A(t)		I			
O	VIB	D(i),I(t)		D			
Mn	VIIA	I(t)	D?				
Cl	VIIB	D(t)		D?			(D)
Br	VIIB	D(t)					(D)
I	VIIB	D(t)		D	D		(D)
Fe	VIII	I(m),D(t)	I				

Figure 2.5: Table displaying various elements and whether they act as donors or acceptors. From [11]

2.1.3 Doping

Various elements have been utilized for both n and p-type doping over the past few decades. For n-type doping, silicon has been utilized and arsenic can act as both as

donor and acceptor depending on which site it incorporates into. Recently, Indium has become the donor of choice, as it is well controlled *in situ*, stable, and can be utilized for a wide range of doping concentrations (from 10^{13} to 10^{19}) [9, 15]. Indium also requires no specific activation anneal, although annealing post growth does help enhance the electrical properties of the material. Near 100% dopant efficiency has been shown for epilayers grown via MBE [12].

For acceptor doping, arsenic has become the primary p-type dopant due to it's large atom size which reduces it's diffusion coefficient, making it more stable and allowing for less interdiffusion across heterojunctions. [45] Arsenic does require a separate activation annealing, as As atoms tend to initially settle into the cation sites, acting as donors instead of acceptors. Figure 2.6 shows arsenic diffusion coefficients as a function of Hg pressure during the anneal, indicating higher *P(Hg)* leads to less arsenic diffusion [7] For this reason, a diffusion anneal is first performed, followed by an short, high temperature (450C) activation anneal, and finally a longer Hg vacancy anneal.

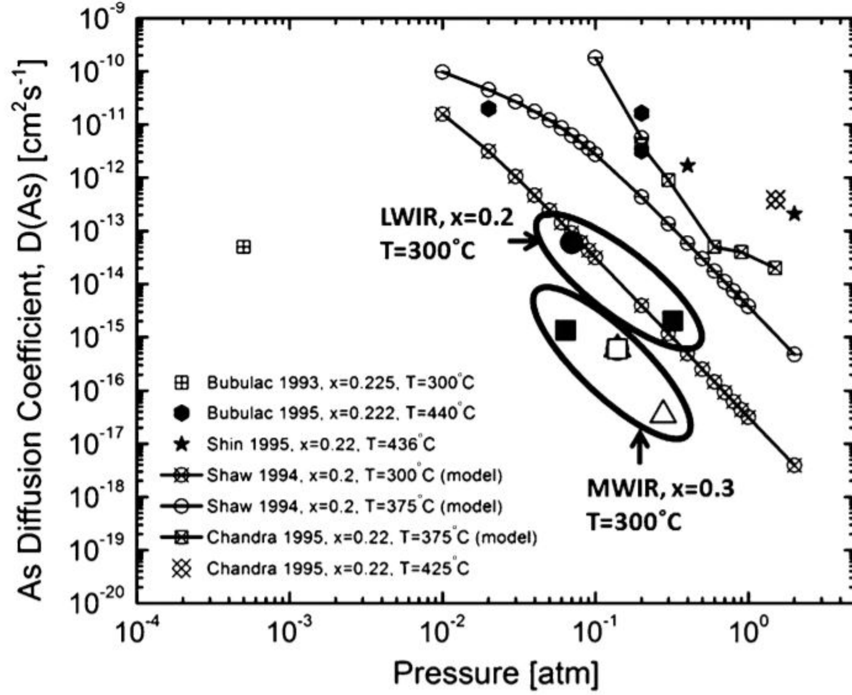

Figure 2.6: Relationship between arsenic diffusion coefficients and Hg partial pressure for MWIR and LWIR HgCdTe. From [7]

2.2 Electronic and Optical Properties

2.2.1 Band Structure

Mercury Cadmium Telluride is comprised of an alloy between semiconductor CdTe (E_g = 1.5 eV) and semimetallic HgTe (E_g = -0.3 eV). It has a zinc-blende structure and a direct bandgap, making it an ideal structure for optoelectronic applications in the infrared range. Figure 4.18 shows a comparison of the Brillouin zone centers for HgTe and CdTe, and also highlights how effective mass changes with composition. By varying the Cd fraction, x, in $Hg_{1-x}Cd_xTe$ the cutoff wavelength can be varied from 1 μm to greater than 20 μm, without a significant change in lattice constant,

as seen in Figure 2.8. This allows for very small lattice mismatch when HgCdTe is grown on CdZnTe substrates. The most widely accepted expression for the energy band gap for $Hg_{1-x}Cd_xTe$ was derived by Hansen [46], and is given by

$$E_g = -0.302 + 1.93x - 0.81x^2 + 0.832x^3 + 5.35 \times 10^4(1 - 2x)T \quad (2.1)$$

Where E_g has units of eV, and T has units of Kelvin.

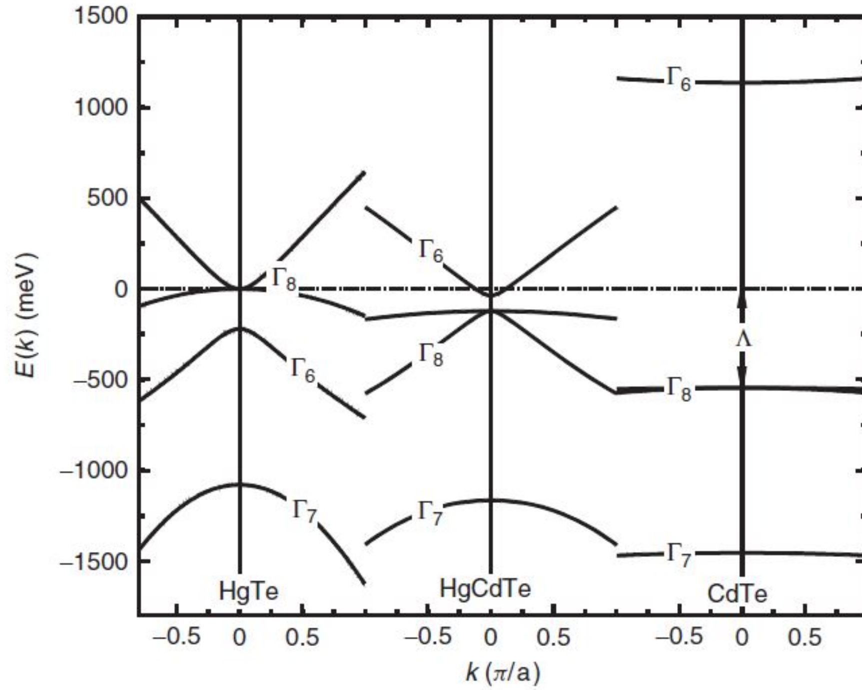

Figure 2.7: Band structure for HgTe, HgCdTe, and CdTe near the center of the Brillouin zone. Bandgap, curvature, and valence band offset are all displayed for each material. [**?**]

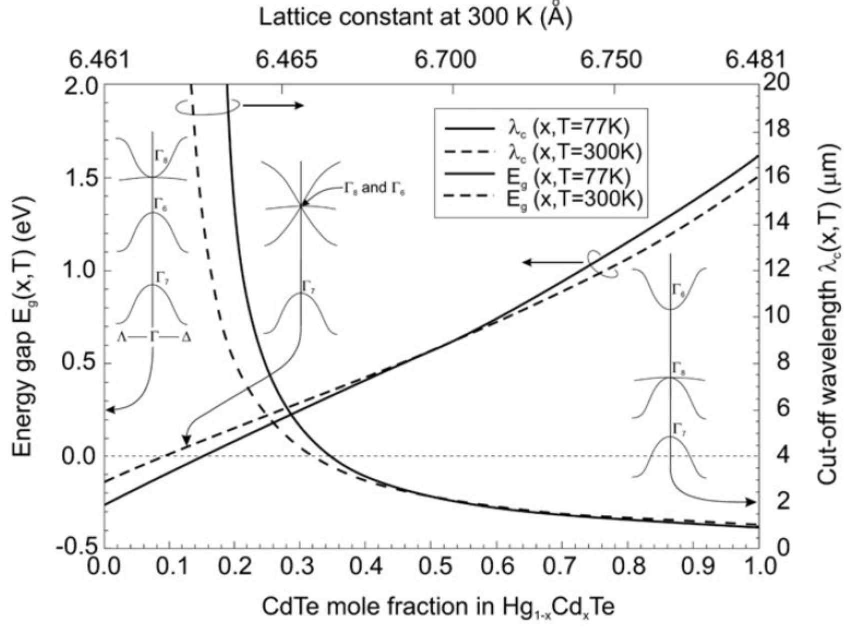

Figure 2.8: Band gap energy, E$_g$, and Cutoff wavelength, λ_c, as a function of CdTe mole fraction for 77K and 300K. Lattice constant variation is also displayed. [6]

2.2.2 Effective Mass

The effective mass of electrons near the conduction band egde has been experimentally defined to primarily be a function composition and temperature. However, due to the non-parabolicity of the conduction band, m_e^* is also a function of of E$_F$ - E$_c$. Weiler et al [47] derived an expression for the electron effective mass

$$m_e^* = m_o \left[1 + 2F + \frac{E_P}{3}\left(\frac{2}{E_g(x,T)} + \frac{1}{E_g(x,T) + \Delta}\right)\right]^{-1} \tag{2.2}$$

where m_o is the electron rest mass in kg, E_P is 19 eV, F is -0.8, and Δ is the split-off band energy of 1 eV. An approximation for m_e^* is given by $m_e^* \approx 0.071E_g$, where E_g is in eV. For heavy holes, the effective mass is typically approximated to

be $m_{hh}^* = 0.55m_o$, although it can range anywhere from 0.3 - 0.7m_o [?]

2.2.3 Dielectric Constant

The dielectric constants are approximated as quadratic functions of composition, x. They have no significant temperature dependence, and are given by [48]

$$\epsilon_{\text{inf}} = 15.2 - 15.6x + 8.2x^2 \tag{2.3}$$

$$\epsilon_0 = 20.5 - 15.6x + 5.7x^2 \tag{2.4}$$

2.2.4 Electron Affinity

The electron affinity, χ, describes the likelihood of the HgCdTe lattice gaining an extra electron. The most common expression from Wenus et al [49] is given below

$$\chi(x,T) = 4.23 - 0.813\left[E_g(x,T) - 0.083\right]. \tag{2.5}$$

2.2.5 Intrinsic Carrier Concentration

The intrinsic carrier concentration in a semiconductor describes the number of electrons and holes that are present in an undoped material, generally as a function of composition and temperature. For HgCdTe, the accepted expression is by Hansen and Schmit [50], which utilizes Equation 2.1 , the $\boldsymbol{k} \cdot \boldsymbol{p}$ method, and $m_{hh}^* = 0.443m_o$,

and is given by

$$n_i = (5.585 - 3.82x + 0.001753T - 0.001364xT) \times 10^{14} E_g^{3/4} T^{3/2} exp\left(\frac{-E_g}{2kT}\right). \quad (2.6)$$

2.2.6 Mobility

Electron mobility is very high compared to most standard semiconductors used for optoelectronics, typically around $10^4 - 10^5$ cm^2/Vs. This is largely due to a very small electron effective mass. In contrast, the heavy hole mobilities are typically orders of manitude lower. These mobility values make HgCdTe particularly suited for high speed devices such as avalanche photodiodes (APDs). These properties of the HgTe/CdTe system also allowed for the possibility of early experiments regarding the quantum spin Hall effect and new topological states [51, 52].

The accepted expression for minority carrier electron mobility is empirically calculated using Hall data on LPE grown HgCdTe from Scott [53]. The mobility is giving below

$$\mu_e = \frac{9 \times 10^8 \left(\frac{0.2}{x}\right)^{7.5}}{Z^{2\left(\frac{0.2}{x}\right)^{0.6}}} \quad (2.7)$$

for compositions ranging from $0.2 \leq x \leq 0.6$. For $T > 50K$, Z = T, while for $Z \leq 50K$

$$Z = \frac{1.18 \times 10^5}{2600 - |T - 35|^{2.07}}. \quad (2.8)$$

For MWIR and LWIR HgCdTe, hole mobilities at room temperature typically

range from 40-80 cm^2/Vs [6]. There is also an expression for hole mobility at 77K [54] given by

$$\mu_h = \mu_0 \left[1 + \left(\frac{p}{1.8 \times 10^{17}} \right)^2 \right]^{-1/4} \tag{2.9}$$

where $\mu_0 = 440 cm^2/Vs$ and p is the hole carrier density. For many simulation and modeling applications, the ratio of $\mu_e/\mu_h = 100$ is assumed for convenience.

The previous expressions for mobility are empirical fits to measured data from LPE and melt grown HgCdTe layers, and still give a reasonable approximation to mobility values in modern devices, even though they do not take into account other factors, such as carrier density and defects, that can affect overall measured mobility. Although these expressions are typically accurate up to within a factor of two, a more accurate picture can be derived from first principles. For n-type HgCdTe, there are 4 competing scattering mechanisms: Alloy, ionized impurities, neutral impurities, and polar optical phonons. Expressions for these scattering mechanisms are from Kinch [31], and Figure 2.9 gives a comparison of the various scattering methods as a function of temperature for LWIR material. For low temperatures (below 77K), ionized impurity scattering is the dominant mechanism, while for temperatures approaching room temperature, optical phonon scattering dominates.

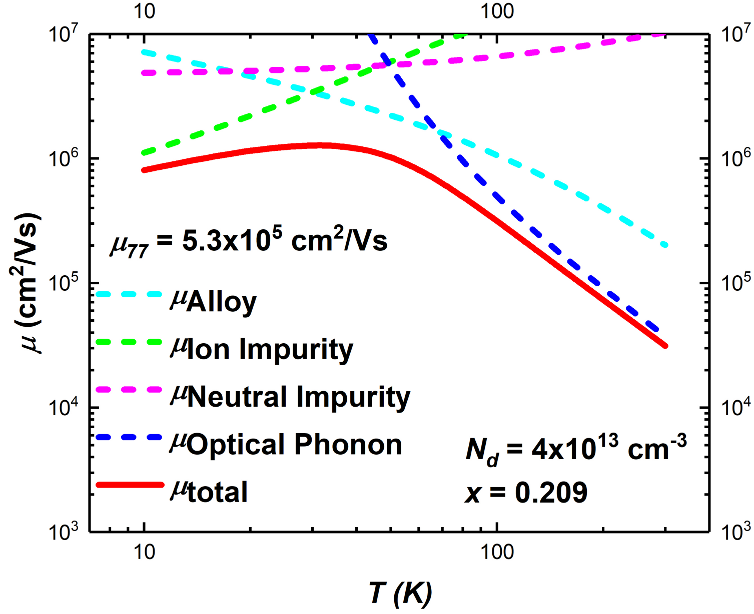

Figure 2.9: Mobility as a function of temperature for n-type HgCdTe as a sum of alloy, ionized impurity, neutral impurity, and optical phonon scattering. [8]

2.2.7 Optical Properties

HgCdTe has excellent optical properties that make it ideal for many optoelectronic applications. There have been a multitude of studies regarding the absorption coefficient, but there is still disagreement between many measured parameters, primarily because differences in composition, defects and impurities, and other material properties can significantly affect absorption. The most widely accepted expression was originally put forth by Finkman and Schacham [55] and further described by Hougens [56], which are based Urbach's rule and a simplified Kane absorption model.

Our work focuses on a model put forth by Moazzami et al [57], which is based upon previous work but uses parameters that are less dependent on material composition,

in order to get a more general expression. For absorption below the band edge ($E_{ph} < E_g$),

$$\alpha = \alpha_0 e^{\frac{\sigma(E - E_0)}{T + T_0}} \tag{2.10}$$

where

$$\alpha_0 = (-0.020366T^2 - 0.46742T + 3878.9)x + (3.9778. * T - 566.4) \tag{2.11}$$

$$T_0 = 81.9 \tag{2.12}$$

$$\sigma = \frac{39103}{T + 55.823} \tag{2.13}$$

For absorption above the band edge ($E_{ph} > E_g$), a quadratic expression based on the Kane model is presented.

$$\alpha = \frac{K\sqrt{(E_T - E_g + c)^2 - c^2}(E_T - E_g + c)}{E_T} \tag{2.14}$$

$$K = 57400E_g + 67260 \tag{2.15}$$

$$c = 0.56667E_g + 0.0013333 \tag{2.16}$$

$$E_g = (-0.00091675x + 0.00049989)T + (1.6624x - 0.27547) \tag{2.17}$$

and E_T is chosen to make the function continuous at the band edge. These expressions are valid for $0.22 < x < 0.61$ and $40K < T < 300K$. HgCdTe has a very sharp increase in absorption right at the band edge, making it great for absorption with energies near the bandgap, while also decreasing the need for very thick absorption layers.

2.2.8 Summary of Material Properties

MCT has many material properties that make it a great absorber and photodiode material. A summary of many of those properties (from Rogalski) [6] is presented below.

Property	HgTe	$Hg_{1-x}Cd_xTe$						CdTe
x	0	0.194	0.205	0.225	0.31	0.44	0.62	1.0
a (Å)	6.461	6.464	6.464	6.464	6.465	6.468	6.472	6.481
	77 K	77 K	77 K	77 K	140 K	200 K	250 K	300 K
E_g (eV)	−0.261	0.073	0.091	0.123	0.272	0.474	0.749	1.490
λ_c (μm)	—	16.9	13.6	10.1	4.6	2.6	1.7	0.8
n_i (cm^{-3})	—	1.9×10^{14}	5.8×10^{13}	6.3×10^{12}	3.7×10^{12}	7.1×10^{11}	3.1×10^{10}	4.1×10^{5}
m_c/m_0	—	0.006	0.007	0.010	0.021	0.035	0.053	0.102
g_c	—	−150	−118	−84	−33	−15	−7	−1.2
$\varepsilon_s/\varepsilon_0$	20.0	18.2	18.1	17.9	17.1	15.9	14.2	10.6
$\varepsilon_\infty/\varepsilon_0$	14.4	12.8	12.7	12.5	11.9	10.8	9.3	6.2
n_r	3.79	3.58	3.57	3.54	3.44	3.29	3.06	2.50
μ_e (cm^2 V^{-1} s^{-1})	—	4.5×10^5	3.0×10^5	1.0×10^5	—	—	—	—
μ_{hh} (cm^2 V^{-1} s^{-1})	—	450	450	450	—	—	—	—
$b = \mu_e/\mu_\eta$	—	1000	667	222	—	—	—	—
τ_R (μs)	—	16.5	13.9	10.4	11.3	11.2	10.6	2
τ_{A1} (μs)	—	0.45	0.85	1.8	39.6	453	4.75×10^3	
$\tau_{typical}$ (μs)	—	0.4	0.8	1	7	—	—	—
E_p (eV)				19				
Δ (eV)				0.93				
m_{hh}/m_0				0.40–0.53				
ΔE_v (eV)				0.35–0.55				

Figure 2.10: Summary of the various material properties of $Hg_{1-x}Cd_xTe$ at various compositions. Also included are properties of HgTe and CdTe binary alloys. [6]

2.3 Generation-Recombination Processes

Generation and recombination processes are important in photodiodes as they are the primary contributors to carrier lifetimes and dark current in HgCdTe detectors. There are 3 relevant G-R processes: Radiative, Shockley-Read-Hall, and Auger. The G-R rates and carrier lifetimes of each process are presented, and then used to calculate

the associated dark current contributions.

2.3.1 Radiative Recombination

Radiative, or direct band-to-band, recombination presents a fundamental limit to overall infrared device performance, as it is not dependent on any tunable parameters, but only intrinsic material properties. Radiative recombination occurs when carriers drop from the conduction to valence band, and give off light (see Figure 1.4a. Radiative generation is the reverse process where light is absorbed and carriers are created. For direct bandgap semiconductors, radiative processes are very common due to the high probability of carriers, and for many MWIR and LWIR devices, radiatively limited devices represent optimal device operation.

The standard expression for the radiative recombination, adapted from Van Roosbroeck and Shockley [31] is presented below

$$\tau_{rad} = \frac{1}{B(n+p)} \tag{2.18}$$

where

$$B = 5.8 \times 10^{-13} \sqrt{\epsilon_{\text{inf}}} \left(\frac{m_0}{m_e + m_{hh}} \right)^{3/2} \left(1 + \frac{m_0}{m_e} + \frac{m0}{m_{hh}} \right) (\left(\frac{300}{T} \right)^{3/2} E_g^2. \tag{2.19}$$

Here, E_g is in units of eV, and expressions for m_e and m_{hh} are given previously in Section 2.2.2. While the radiative limit is typically not geometry specific, the radiative lifetime can be noticeably longer in thicker materials because emitted photons can be reabsorbed back into the material and generate more carriers. The radiative

recombination rate is given below [58]

$$R_{net}^{rad} = B(np - n_i^2). \tag{2.20}$$

2.3.2 Shockley-Read-Hall Recombination

Shockley-Read-Hall, or SRH, recombination is an extrinsic effect that is directly related to material quality. As seen in Figure 1.4b, SRH requires available states to be present in the forbidden region of the band gap. G-R can occur when carriers move through those additional states, known as SRH centers, to transition from the valence band to conduction band (or vice versa), while requiring energies $E < E_g$. The position of these SRH centers can range anywhere from mid gap to very close to the conduction/valence band edges. The concentration of SRH centers located within a given material is expressed by N_r, and the position within the bandgap is expressed by E_r, which is in eV above the valence band. The expressions for SRH lifetime for holes and electrons are [31]

$$\tau_n = \frac{\tau_{po}(n + n_1) + \tau_{no}\left[p + p_1 + \dfrac{N_r p_1}{(p + p_1)}\right]}{n + p + \dfrac{N_r p p_1}{(p + p_1)^2}} \tag{2.21}$$

$$\tau_p = \frac{\tau_{no}(p + p_1) + \tau_{po}\left[n + n_1 + \dfrac{N_r p}{(p + p_1)}\right]}{n + p + \dfrac{N_r p p_1}{(p + p_1)^2}} \tag{2.22}$$

where

$tau_{no} = 1/\gamma_n$ and $tau_{po} = 1/\gamma_p$, γ_n and γ_p are recombination coefficients for electrons and holes into the SRH centers. n_1 and p_1 are given below:

$$n_1 = N_c exp\Big[\frac{-q(E_g - E_r)}{kT}\Big] \tag{2.23}$$

$$p_1 = N_v exp(-qE_r/kT) \tag{2.24}$$

where N_c and N_v are the densities of states for the conduction and valence bands. For modeling and simulations, where extensive knowledge is not known about SRH center densities and energies, a simpler expression for approximating SRH recombination is presented below [59] :

$$\tau_{rad} = \frac{1}{\sigma v_{th} N_r} \tag{2.25}$$

where σ is the electron or hole capture cross section, and v_{th} is the thermal carrier velocity. The G-R rate for Shockley-Read-Hall recombination is based on Equation 2.21 (from [60])

$$R_{net}^{SRH} = \frac{N_r(pn - n_i^2)}{\tau_{po}\Big[n + n_i exp\Big(\frac{E_i - E_r}{kT}\Big)\Big] + \tau_{no}\Big[p + n_i exp\Big(\frac{E_r - E_i}{kT}\Big)\Big]} \tag{2.26}$$

and E_i is the intrinsic energy level, n_i is the intrinsic carrier concentration described above in Equation 2.6. Shockley-Read-Hall recombination is a major contributor to the dark current in many materials, and is the limiting factor in SWIR HgCdTe. However, in high quality MWIR and LWIR, material quality has advanced to a point where SRH recombination is no longer the limiting process.

2.3.3 Auger Recombination

Auger recombination is the most critical of the three G-R processes in many infrared materials, and specifically in HgCdTe. In MWIR and LWIR devices, it accounts for the shortest minority carrier lifetime, and it is also the most difficult process to eliminate. Auger generation, in contrast to SRH and radiative, is a multiple carrier process that can be considered to be the opposite of impact ionization. Beattle and Landsberg (cite) originally described a variety of different possible Auger recombination methods. Here, two methods, Auger 1 and Auger 7, will be highlighted as they have the lowest required threshold energy to occur, and thus the highest frequency of occurrence.

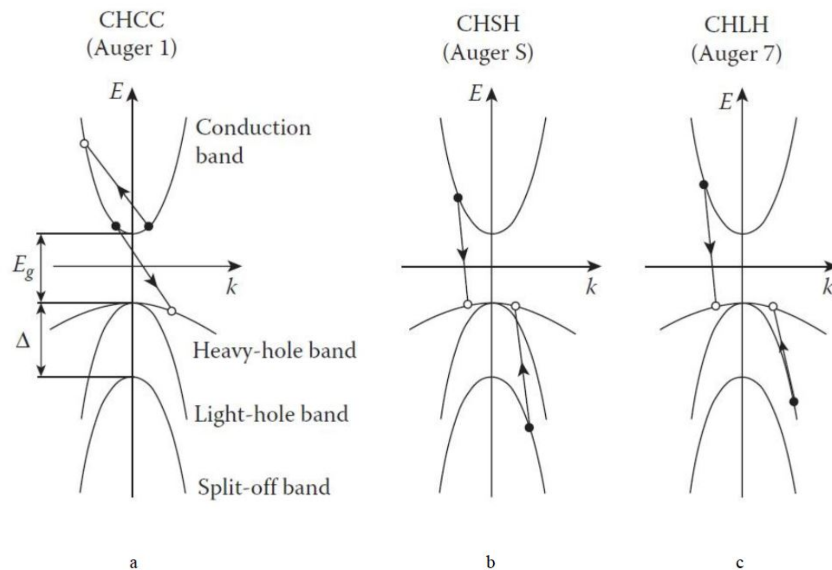

Figure 2.11: Diagram of the most probable Auger recombination pathways [12]

Auger 1 recombination is defined as a collision between two electrons in the conduction band, causing one electron to recombine with a hole in the valence band, and the other gains energy and jumps to a higher energy state in the conduction

band. Figure 2.11a displays the Auger 1 process, which requires two electrons with the proper available energy states, as well as proper available momentum transitions as well. The expression for the Auger 1 recombination lifetime is given by [31]

$$\tau_{A1} = \frac{2\tau_{Ai1} n_i^2}{n(n+p)} \tag{2.27}$$

where τ_{Ai1} is defined as the intrinsic Auger 1 lifetime. The expression for the intrinsic lifetime is given below:

$$\tau_{Ai1} = \frac{7.6 \times 10^{-18} \epsilon^2 (1+\mu)^{1/2} (1+2\mu)}{\frac{m_e}{m_o} |F_1 F_2|^2 \left(\frac{kT}{E_g}\right)^{3/2}} \exp\left[\frac{1+2\mu}{1+\mu} \frac{qE_g}{kT}\right] \tag{2.28}$$

where $\mu = \frac{m_e}{m_{hh}}$ and $|F_1 F_2|$ is the wavefunction overlap matrix integraal, which typically ranges from 0.1 - 0.3 in HgCdTe.

In p-type MCT, Auger 7 is the primary mechanism, involving the recombination of a heavy hole and a minority electron, sending a second heavy hole into the light hole band. There are various explicit expressions for Auger 7 lifetime, but a common approximation of $\tau_{Ai7} \approx \gamma \tau_{Ai1}$ is typically utilized for modeling purposes. The ratio γ ranges from 3-6 for $0.16 \leq x \leq 0.4$ and $50K \leq T \leq 300K$ [61], and has been defined as high as 8 for $x \approx 0.2$ and $T = 295K$ [62].

The total Auger recombination rate, based on Beattie and Landsberg [63] is given by

$$R_{net}^{Aug} = \frac{pn^2 - nn_i^2}{2n_i^2 \tau_{Ai1}} + \frac{np^2 - pn_i^2}{2n_i^2 \tau_{Ai7}} \tag{2.29}$$

Auger recombination is a complicated process to model and quantify, but more and

more methods are becoming available to suppress Auger recombination [15, 35, 64], allowing for MWIR and LWIR devices that can become background limited, even at higher temperatures.

Chapter 3

HgCdTe Device Technology

The performance of a Mercury Cadmium Telluride infrared detector is strongly dependent on a multitude of factors, such as the material parameters and defects, as mentioned in Chapter 2. Common performance metrics such as dark current density (noise in the device), quantum efficiency (signal), and detectivity (signal to noise ratio) vary significantly across different devices. There are limited ways to control and vary these material and device parameters. However, one area that can be entirely controlled is the device geometry. Device architecture can have a significant impact on performance, and is only limited by growth technology.

3.1 Standard HgCdTe Device Architectures

While a variety of standard device technologies are currently in use today, they all have certain aspects in common. Devices are built around a p-n junction between two layers of HgCdTe. The p-n junction can be formed via mechanical methods (such as ion implantation or diffusion), or by incorporation of dopant atoms during the growth process (common for MBE and MOCVD growth). [2]

Another important aspect of device design include surface passivation to reduce

surface recombination. There are a multitude of available options, including deposited dielectrics (including ZnS and anodic oxides) as well as semiconductor heterostructures like CdTe [65]. These passivation materials must not only be effective, but also must be transparent to infrared light. Depending on how the device is designed, some detectors are illuminated from the top of the device (typically near the junction) and some are illuminated from the bottom (through the substrate). Figure 3.1 shows the most common example of a p-n junction photodiode architecture, the Double Layer Planar Heterojunction (DLPH), described in Chapter 2.

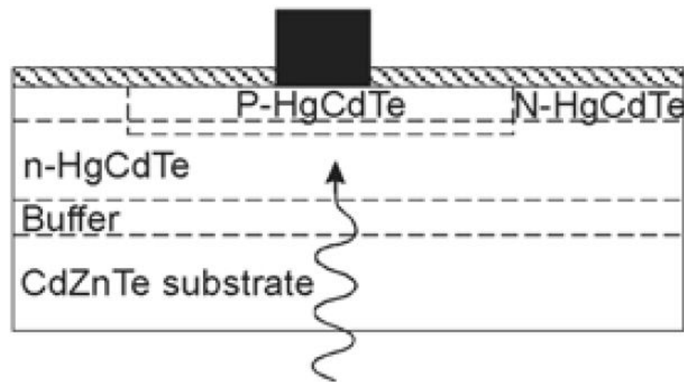

Figure 3.1: Diagram of a typical HgCdTe P-on-n planar heterojunction photodiode [2]

3.2 Rule 07

While there are many figures of merit that describe overall device performance across all infrared material systems (such as dark current and quantum efficiency), the most common metric for HgCdTe devices is known as "Rule 07". Rule 07 is an empirical model that predicts the dark current density of high performance HgCdTe detectors over a wide range of operating temperature and cutoff wavelengths. The model has been shown to be accurate to within a factor of 2.5 for the best detectors grown

at many of the top manufacturers, and offers insight into what mechanisms may be limiting detector performance.

The Rule 07 metric was developed by W. Tennant et. al., and has been described via two seminal publications [13,14]. Initially, a survey was done of 26 of the best MBE grown MCT layers produced by Teledyne Imaging Sensors. These layers utilized the DLPH structure, and the junctions were all created via ion implantation. Base layer doping ranged from 5×10^{14} cm^{-3} to 2×10^{15} cm^{-3} The majority of the layers were grown on CdZnTe substrates, and primarily consist of SWIR devices with $\lambda_c = 2.5\mu m$, MWIR devices with $\lambda_c = 5 - 5.3\mu m$, and LWIR devices with $\lambda_c = 8.6 - 15.6\mu m$, although in [14] the study was expanded to include a wider variety of layers.

The empirical model is a relationship between the product of cutoff wavelength and temperature ($\lambda_c \times T$) and the dark current density, J_D, in units of A/cm^2. A linear relationship was established between J_D and $1/(\lambda_c \times T)$, which was then fit to develop the model. the analytical expression is given by Equation 3.1, where $J_0, Pwr, C, \lambda_{scale}$, and $\lambda_{threshold}$ are all fitting parameters. (from [14])

$$J = J_0 e^{C(1.24q/k\lambda_e T)} \tag{3.1}$$

$$\lambda_e = \lambda_c \text{ for } \lambda_c \geq \lambda_{threshold} \tag{3.2}$$

$$\lambda_e = \frac{\lambda_c}{1 - (\frac{\lambda_{scale}}{\lambda_c} - \frac{\lambda_s cale}{\lambda_{threshold}})^{Pwr}} \text{ for } \lambda_c < \lambda_{threshold} \tag{3.3}$$

$$J_0 = 5315.03A/cm^2$$

$$Pwr = 0.56956$$

$$C = -1.14027$$

$$\lambda_{scale} = 0.21508\mu m$$

$$\lambda_{threshold} = 4.8434\mu m$$

Figure 3.2 shows the fit between various detectors and the Rule 07 prediction, demonstrating the prediction as an lower bound of dark current density for state of the art devices. The fit is accurate over roughly 13 orders of magnitude. For comparison, traditional $In_{0.53}Ga_{0.47}As$ is included, as well as InSb.

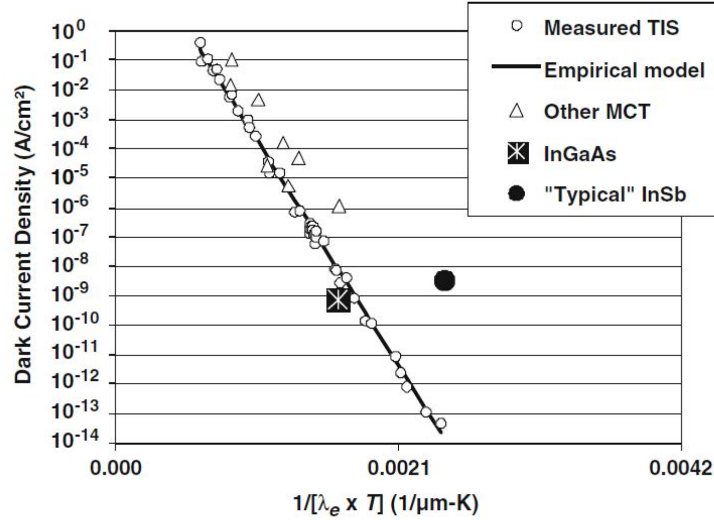

Figure 3.2: Comparison between Rule 07 empirical model and other measured HgCdTe photodetectors. Also included are typical InGaAs and InSb detectors. [13]

While the "Rule 07" heuristic already has significant utility in being able to predict the estimated dark current density for a particular device design, it also shows utility in being able to help explain what the limiting factors for typical HgCdTe devices are. Peak device performance is achieved when SRH and Auger recombination are minimized, and the device is limited only by background radiation. Figure 3.3 shows the ratio between dark current predicted by Rule 07 and dark current in a radiatively limited device. For MWIR devices, the ratio is less than 10, indicating devices are close to optimal performance. For SWIR and LWIR devices, this is not the case. In the case of LWIR, the deviation from background limited performance can be explained by the high presence of Auger recombination. Figure 3.4 shows a comparison between the predictions of Rule 07 and Auger 1 recombination, and they are a very close match.

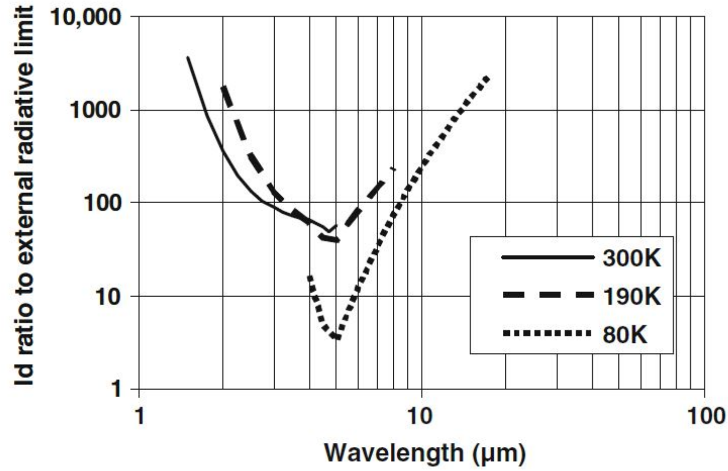

Figure 3.3: Radio of Rule 07 predicted dark current to background radiation limited dark current as a function of λ_c. [13]

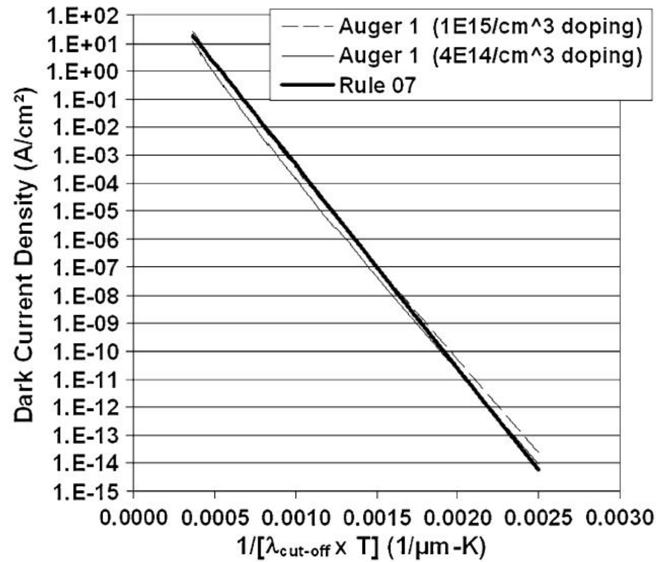

Figure 3.4: Predicted dark current densities from Rule 07 and Auger 1 recombination. [14]

Rule 07 is a great performance baseline to aim for when designing new devices, but it is evident that this does not exhibit any sort of fundamental limit to performance.

Since it's inception, there has been a push not only to create devices that match Rule 07, but to create devices that can surpass the predicted performance. For the case of MWIR and LWIR, the limiting factor that must be addressed is Auger recombination.

3.3 Auger Suppression

As described in Section 2.3.3, Auger recombination is a fundamental, multi-carrier process that causes dark current in photodiodes. It is the dominant recombination process in devices operating in the MWIR and LWIR wavelength ranges. While Auger recombination can not be completely eliminated in a device, there are multiple methods to minimize it's contribution to the overall dark current in a device. Changing the bandstructure of a device, either by spatially separating electrons and holes or splitting the light and heavy hole valence bands via strain, can significantly decrease the rate of Auger recombination. Decreasing the doping density in the absorbing layer of a standard device can also have a similar effect. A decreased dark current can allow for better performance, or similar performance at higher temperatures. Thus, suppressing Auger recombination has been a major research focus for the HgCdTe community, as well as the larger IR field.

In recent years, novel device structures have been introduced to improve the overall quality of IR detectors, primarily by decreasing dark current. Reducing the dark current density in these novel devices has two applications: First, it is useful for very sensitive detectors (such as space based astronomy), but it also allows for detectors that can operate at elevated temperatures with J_D comparable to existing technologies. These proposed High Operating Temperature (HOT) devices can allow for MWIR and LWIR devices that can operate without the need for cryogenic cooling systems. There are a few proposed architectures that are designed to decrease

overall dark current. Low doped, non-equilibrium DLPH detectors offer significnat reduction in Auger recombination, and the introduction of barrier devices can help further decrease dark current by limiting the effects of other processes like surface recombination.

3.3.1 Non-equilibrium Devices

While most HgCdTe devices operate under some reverse bias, they operate very close to equilibrium conditions (zero bias). One method to improve the dark current performance of IR detectors is to operate them at significant bias voltages, thus making these devices significant non-equilibrium. At these strong bias levels, excess carriers are depleted within the active region, making the extrinsically controlled doping level of significant importance.

A recent method for Auger suppression in HgCdTe utilizes lower doping levels in the absorbing layer. In HgCdTe operating at elevated temperatures, the carrier density will be equal to the intrinsic carrier density. A typical p-n photodiode operates at a reverse bias however, which causes many of the holes that are present to diffuse across the junction. Due to charge neutrality conditions, this also causes electrons to be swept out as well. If this process happens faster than carriers can be thermally generated, then the remaining electron density changes from n_i to n_D (Figure 3.5).

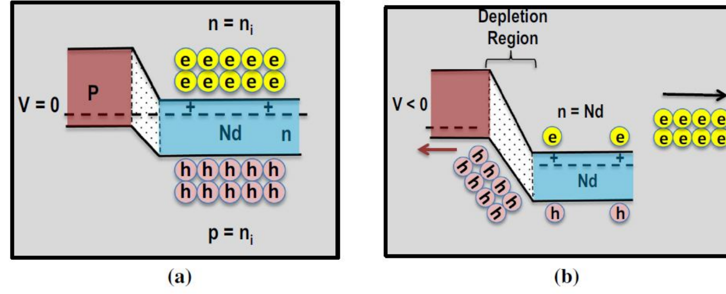

Figure 3.5: Depiction of the carrier density in a P-on-n photodiode in a) zero bias condition and b) reverse bias condition. [15]

In an ideal P-on-n photodetector described by Auger 1 recombination, the dark current density related to Auger recombination is given by

$$J_D = \frac{qn_i^2 d}{n\tau_{A1}} \tag{3.4}$$

where q is the electrical charge, d is the absorber layer thickness, and τ_{A1} is the Auger recombination lifetime given by Equation 2.3.3. When the lifetime is substituted into the equation, the dark current density becomes

$$J_D = \frac{qn_i d}{\tau_{Ai1}} \tag{3.5}$$

which scales linearly with n_i. By sweeping out additional carriers, n_i can be replaced with n_D. Thus, by lowering the extrinsic doping concentration in the absorber region, the dark current density can be decreased as well. This relationship c an be seen as a function of temperature and doping level in Figure 3.6.

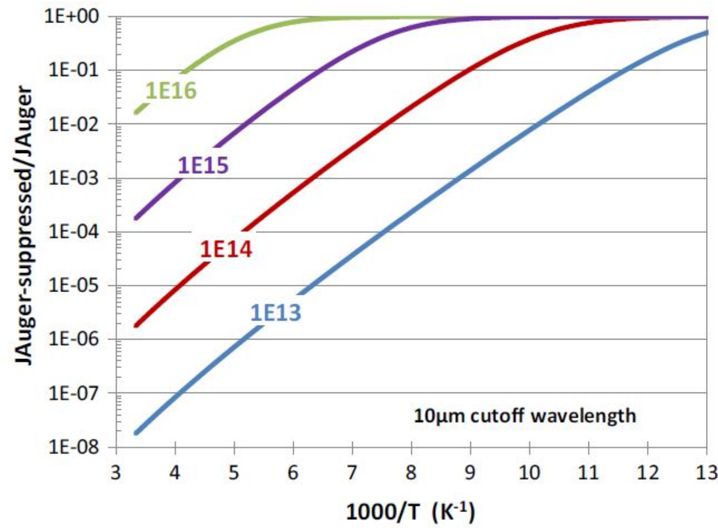

Figure 3.6: Ratio of Auger-suppressed dark current to Auger recombination current as a function of temperature and absorber level doping density. [15]

3.3.2 Barrier Detectors

Barrier devices, more commonly known as nBn devices, involve a recently developed device structure with a wide bandgap barrier layer, an example of which is depicted in Figure 3.7. The barrier layer prevents the flow of majority carriers, but allows minority carriers (in this case, holes) to flow unimpeded. These devices can be made using only a single dopant type, typically utilizing an entirely n-type structure. This architecture offers a manufacturing advantage for systems like HgCdTe where p-type doping is difficult.

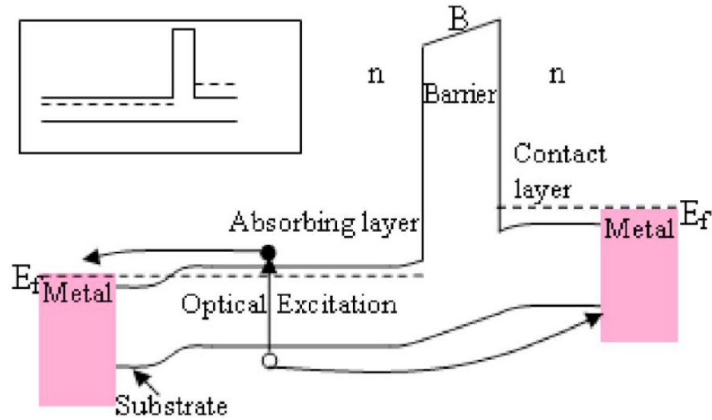

Figure 3.7: Device architecture of a nBn photodetector, both under reverse bias and at flat band condition. [16]

Barrier detectors were one of the first proposed architectures for achiving HOT devices, because the barrier layer effectively eliminates SRH and surface recombination currents. In SWIR and MWIR devices that are limited by these mechanisms, significant increases in operating temperature have been realized. The nBn architecture has been realized in both III-V [16, 66, 67] and HgCdTe devices [68, 69], but to address Auger recombination, barrier architectures have been used in conjunction with another novel detector structure: the strained-layer superlattice.

Theoretical predictions have shown that strained-layer superlattices can exceed the performance of Rule 07, but very few fabricated devices have matched the predicted performance [70, 71] . Some studies have also included barrier structures in their SLS design to help improve dark current in more recent studies [72].

Chapter 4

HgCdTe Carrier Transport

In order to achieve Auger suppression in HgCdTe, low doping levels must be realized in the absorber layer of the device. Traditional MCT detectors have doping levels between 5×10^{14} and $2\times10^{15} cm^{-3}$. If the doping level can be decreased to $1\times10^{14} cm^{-3}$ or lower, there can be a decrease in the associated dark current density by an order of magnitude or more.

Realizing lower doping levels in HgCdTe has historically proven challenging. Impurities in grown materials have lead to a decreased mobility in lower doped samples [73], background impurities can contribute additional carriers, and Hg vacancies can create mixed conduction effects [74]. Recent work done at Teledyne Imaging Sensors has demonstrated the ability to consistently dope materials in the low to mid $10^{13} cm^{-3}$ range, an order of magnitude below the level of many common devices [15].

4.1 Magnetotransport

4.1.1 Van der Pauw Method

Electrical characterization of low doped HgCdTe presents experimental challenges. In bulk materials, electrical properties, such as carrier density and mobility, are mea-

sured via the Hall effect. To observe the Hall effect, a finite sample is placed in a perpendicular magnetic field. When a current is passed through the sample, the force from the magnetic field causes carriers to accumulate on one side of the sample, creating a charge gradient across the material. This charge density leads to an electric field and voltage that is perpendicular to the current flow as well (see Figure 4.1). The Hall voltage, V_H, and the associated Hall coefficient, R_H, is given by Equation 4.1 for a bulk n-type material, and can be measured directly (in conjunction with the resistivity of the material) to extract the carrier density and mobility of a semiconductor [59].

$$V_H = \frac{IB}{qnd} \quad (4.1)$$

$$R_H = \frac{V_H d}{IB} = -\frac{1}{qe} \quad (4.2)$$

$$\rho = \frac{1}{q\mu n} \quad (4.3)$$

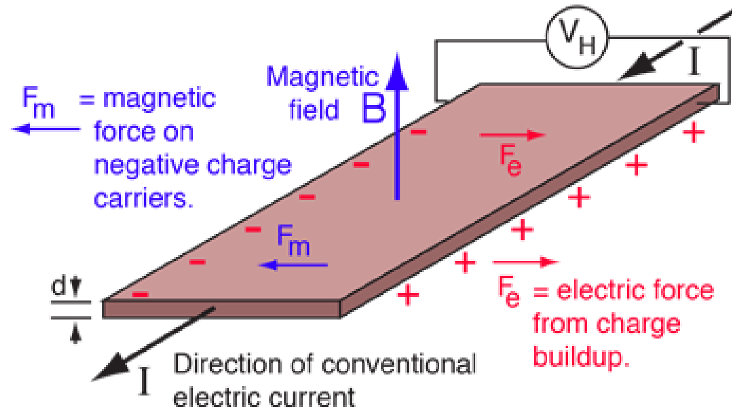

Figure 4.1: Diagram depicting charge build-up in bulk material, resulting in the observation of an effective Hall voltage, V_H. [17]

In order to observe the Hall effect in any semiconductor material, electrical contacts must be applied to the surface of the material. Various orientations are used in practice depending on the desired result. The simplest and most direct method of measurement is the Van der Pauw technique. Based on [75, 76], measurements are made at 4 points. While the van der Pauw method is designed to work with samples of arbitrary shape, the standard geometries are typically squares or cloverleaf shapes, as seen in Figure 4.2. For resistivity measurements, current is passed between two adjacent contacts (ex I_{12}) and voltage is measured between remaining contacts (V_{34}). This is repeated between all remaining contact pairs, and reversed polarities as well, yielding 8 resistance values, which can be averaged together to calculate the resistance of the sample. If the layer geometry is known, this can be converted into a resistivity using $\rho = RA/L$ where A is the cross sectional area and L is the length between contacts.

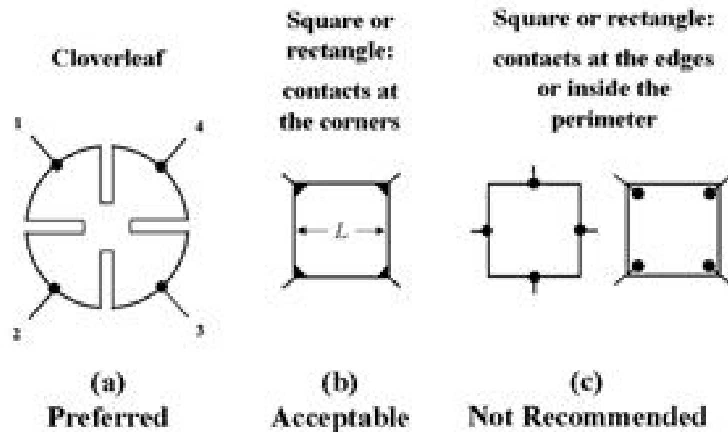

Figure 4.2: Common contact geometries for van der Pauw measurements [18]

To calculate the Hall coefficient, a constant magnetic field is applied perpendicular

to the sample. Current will be applied from contact 1 to 3 (I_{13}), and voltage will be measured from contact 2 to 4 (V_{24}). This measurement is repeated for the 8 possible configurations, and the voltages are averaged in order to calculate the Hall voltage and Hall coefficient. The carrier density and mobility can then be extracted using eqs. (4.1) to (4.3). [18]

4.1.2 Variable-Field Hall Effect

The van der Pauw technique is very versatile and efficient at extracting basic carrier transport data from bulk semiconductors. However, this measurement technique fails when multiple carrier types are present, such as two electron species or the presence of both electrons and holes. The carrier concentration and mobility values that are extracted are an average over the volume of the sample, and if the sample is not uniform and isotropic, those values may not be representative of the true transport properties.

In order to extract carrier transport information from many layered structures with multiple carrier species, the Variable-Field Hall effect is utilized. As described by Gold and Nelson in [19], measurements of Hall voltage and resistivity are made in the same manner as the Van der Pauw technique, but with a varying magnetic field. In a sample with multiple carriers with different mobilities, as the field is increased, carriers with a higher mobility will be swept to the edges of the sample faster than those of lower mobility, making it easier to isolate properties of the lower mobility carriers. Also, depending on their mobility, in a sample with mixed conduction, electrons and holes will be dominant in different magnetic field ranges. In a single-field measurement, this can lead to incorrect identification of the dominant carrier species. An example of this can be seen in Figure 4.3, where the Hall coefficient is

shown to change sign as a function of magnetic field.

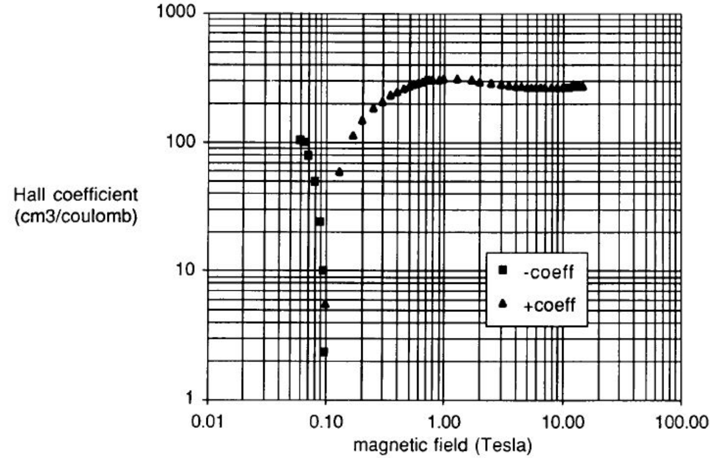

Figure 4.3: Hall coefficient as a function of magnetic field in HgCdTe. The sign of the Hall coefficient changes sign around 0.1T, indicating the presence of both electrons and holes. [19]

4.1.3 Multi-Carrier Fitting

Variable-Field Hall effect measurements allow us to get carrier transport information from multi-layered samples. In order to systematically extract that data, more detailed routines must be investigated. Two methods are utilized in order to extract this information: the Multi-carrier fitting (MCF) procedure, and Mobility Spectrum Analysis (MSA).

Resistivity and Hall coefficient are measured in the aforementioned manner, but this data must be converted into a more convenient form for analysis. The 2-dimensional conductivity tensor is commonly used to represent data in magneto-transport experiments. In a general system with current flow in both the x- and y-directions, the current density can be represented by contributions from electric

fields in both of those directions, as shown in eqs. (4.4) and (4.5).

$$J_x = \sigma_{xx} E_x + \sigma_{xy} E_y \tag{4.4}$$

$$J_y = \sigma_{yx} E_x + \sigma_{yy} E_y \tag{4.5}$$

$$\tag{4.6}$$

Here, J_i is current in the i direction, E_i is the electric field, and σ_{ij} are the conductivity tensor components. From symmetry, $\sigma_{xy} = -\sigma_{yx}$ and $\sigma_{xx} = \sigma_{yy}$, so the conductivity tensor can be represented by

$$\sigma = \begin{bmatrix} \sigma_{xx} & \sigma_{xy} \\ -\sigma_{xy} & \sigma_{xx} \end{bmatrix} \tag{4.7}$$

Following the derivation in [77], we can define the current flow in a Hall effect experiment to be in the x-direction. In steady state, this means that there is no net current flow in the y-direction, so $J_y = 0$. This implies that $E_y = (\sigma_{xy}/\sigma_{xx})E_x$ and

$$J_x = \frac{\sigma_{xx}^2 + \sigma_{xy}^2}{\sigma_{xx}} E_x \tag{4.8}$$

.

Using eqs. (4.1) to (4.3), we can express the Hall coefficient and resistivity as a function of the conductivity tensor components (eqs. (4.9) and (4.10))

$$R_H(B) = \frac{V_H d}{IB} = \frac{\sigma_{xy}/B}{\sigma_{xx}^2 + \sigma_{xy}^2} \tag{4.9}$$

$$\rho(B) = \frac{E_x}{J_x} = \frac{\sigma_{xx}}{\sigma_{xx}^2 + \sigma_{xy}^2} \tag{4.10}$$

and inversely, we can express the conductivity tensor components as a function of measurable parameters

$$\sigma_{xx}(B) = \frac{\rho}{B^2 R_H^2 + \rho^2} \tag{4.11}$$

$$\sigma_{xy}(B) = \frac{B R_H}{B^2 R_H^2 + \rho^2} \tag{4.12}$$

An example of a measured conductivity tensor vs magnetic field is displayed in Figure 4.4.

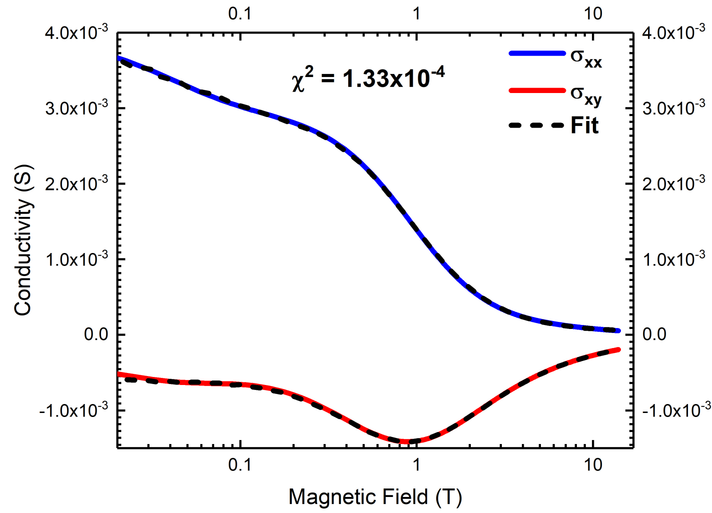

Figure 4.4: Plot of conductivity tensor components, σ_{xx} and σ_{xy} vs magnetic field for a representative HgCdTe sample

In order to extract data from these measurements, the conductivity tensor components can also be expressed as a function of n and μ using the Boltzmann transport equation. If we assume we have m carriers, σ_{xx} and σ_{xy} can be rewritten as

$$\sigma_{xx}(B) = \sum_{i=1}^{m} \frac{qn_i\mu_i}{1+(\mu_i B)^2} \tag{4.13}$$

$$\sigma_{xy}(B) = \sum_{i=1}^{m} S_i \frac{qn_i\mu_i^2 B}{1+(\mu_i B)^2} \tag{4.14}$$

where $S = \pm 1$ for holes and electrons. By assuming the number and type of carriers present in a sample, the Multi-carrier fitting procedure allows for transport information to be extracted by fitting σ_{xx} and σ_{xy} to eqs. (4.13) and (4.14) [77, 78].

4.1.4 Mobility Spectrum Analysis

For the MCF procedure, an assumption must be made about the number of type of carriers that are present in a material. Mobility spectrum analysis allows for extraction of similar data without any assumptions. The technique was initially developed by Beck and Anderson [79] to study multi-layered HgCdTe and III-V quantum well structures. By using an iteration process, the original MSA process was able to calculate an upper bound to the spectrum information. Future algorithms have made significant strides to minimize the overall error [80, 81].

The MSA method utilized in this study is Fourier-domain Mobility Spectrum Analysis (FMSA) developed by Dr. Boya Cui and Prof. Matthew Grayson at Northwestern University [20, 82]. The conductivity tensor components are calculated initially using the measured resistivity and Hall coefficient. Instead of rewriting σ_{xx} and σ_{xy} using crefeq:tensor5,eq:tensor6, they can be expressed as

$$\sigma_{xx}(B_j) = \sum_{i=1}^{k} A_{xx}^{ij} \left[s_p(\mu_i) + s_n(\mu_i) \right] \quad (4.15)$$

$$\sigma_{xy}(j) = \sum_{i=1}^{k} A_{xy}^{ij} \left[s_p(\mu_i) - s_n(\mu_i) \right] \quad (4.16)$$

where B_j are the discrete magnetic field values, and μ_i are the mobility values used to create the spectrum Expressions for A^{ij}, s_p, and s_n are given by eqs. (4.17) to (4.20)

$$A_{xx}^{ij} = \frac{1}{1 + (\mu_i B_J)^2} \quad (4.17)$$

$$A_{xy}^{ij} = \frac{\mu_i B_j}{1 + (\mu_i B_J)^2} \quad (4.18)$$

$$s_p(\mu_i) = p_i q \mu_i \quad (4.19)$$

$$s_n(\mu_i) = n_i q \mu_i \quad (4.20)$$

where p_i and n_i are the hole and electron carrier densities at a given mobility value. At each given mobility value, the s_n and s_p functions are iterated up and down from an initial value, and total error between the initial guess function and the measured conductivity tensor components is calculated. After each iteration, if the error decreases, that value is accepted, otherwise the original value remains. This process takes place for a given number of iterations (typically 1000 or more). A schematic of this process can be seen in Figure 4.5.

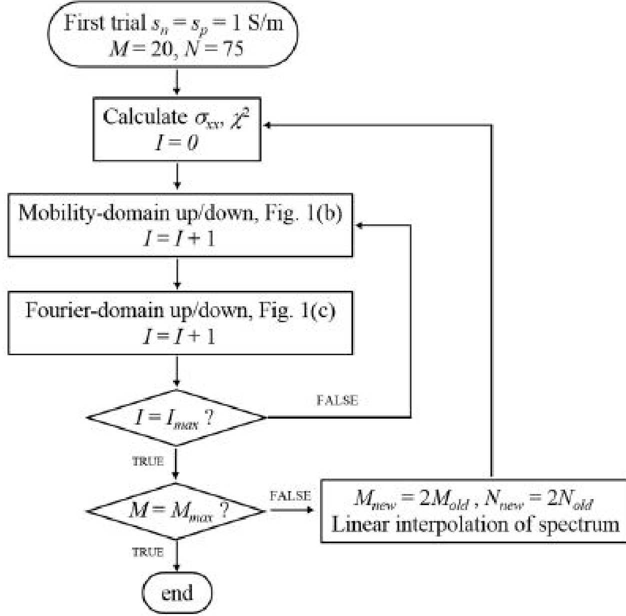

Figure 4.5: Flow chart of the FMSA iteration process. [20]

As seen in the schematic, after a first pass is completed with a given number of spectral mobility points, M and iterations I, the full FMSA process is completed again, with more mobility points resulting in a finer mobility spectrum resolution. To ensure that each consecutive iteration decreases the total error, it is tracked and plotted against the total number of iterations, as shown in Figure 4.6. The spikes in the plot show where M was changed, and it can be clearly seen that the overall error rapidly decreases until it approaches a convergence at a value near $\chi^2 = 10^{-5}$.

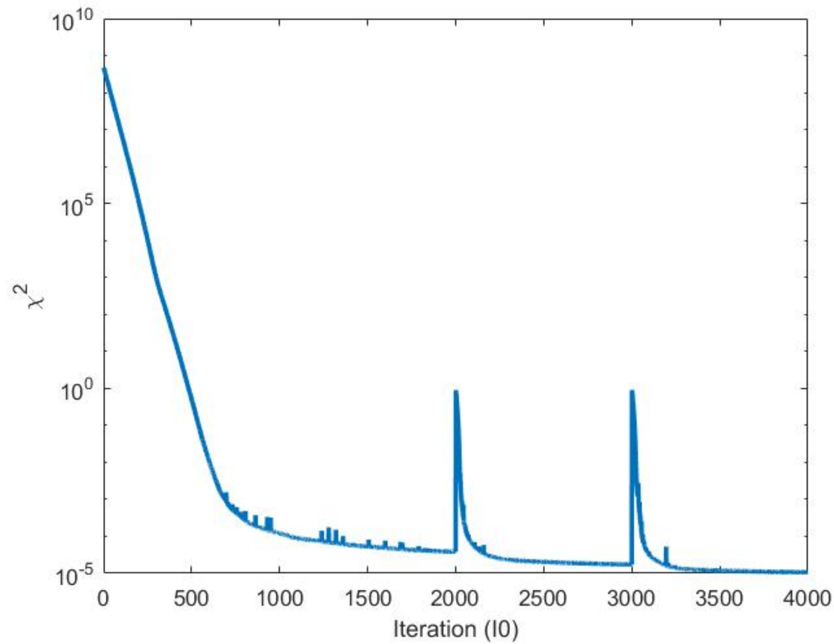

Figure 4.6: Plot of total error, χ^2, as a fucntion of the total number of FMSA iterations. The spikes correspond to increases in the mobility spectral resolution, and the total error converges at a value near $\chi^2 = 10^{-5}$.

The result of this process is a mobility spectrum, which displays peaks corresponding to different carrier species at different mobility values. This process allows for carrier density, mobility, and carrier type to be extracted without the need for any trial function or initial guess related to *a priori* knowledge of the material. [20]. A sample spectrum can be seen in Figure 4.7.

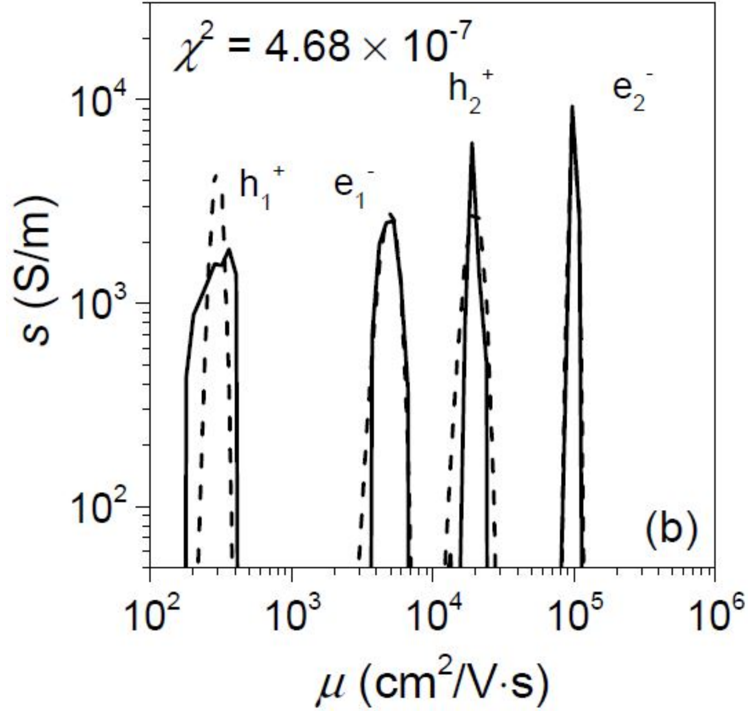

Figure 4.7: Sample mobility spectrum fit to synthetic data with two electron and two hole species. [20]

4.2 Experimental Results

4.2.1 Experimental Setup

Magnetotransport experiments were conducted on multi-layer, MBE grown HgCdTe samples provided by Teledyne Imaging Sensors. Each sample consisted of 3 layers: a wide bandgap, higher doped ($n \approx 10^{15} cm^{-3}$) buffer layer, a low doped absorber layer ($n \approx 5 \times 10^{13} cm^{-3}$), and a wide bandgap cap layer, all grown on a CdZnTe insulating substrate. A schematic of the layer structure can be seen in Figure 4.8.

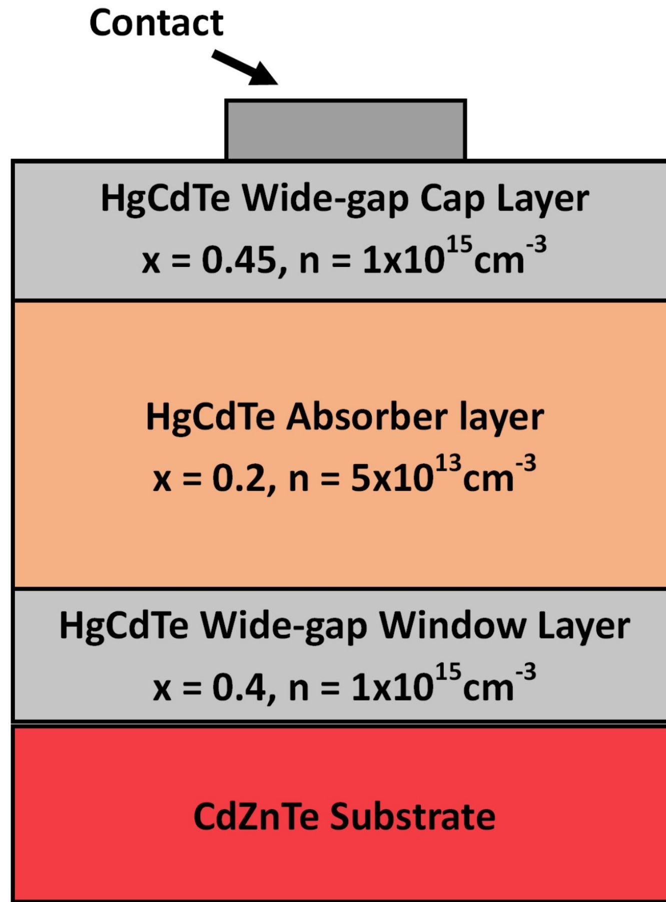

Figure 4.8: A standard device structure for MBE-grown HgCdTe, with a low doped, narrow bandgap absorber layer and a higher doped, wide bandgap buffer and cap layer. [8]

For verification purposes, a standard van der Pauw measurement was completed on each sample using a 4-point probe station. No contact pads were deposited for those measurements. However, for the variable magnetic field measurements, instead of using a standard van der Pauw contact geometry, the MCT samples were fabricated into Hall bar structures. The van der Pauw geometry can introduce systematic measurement error, as carriers can flow anywhere in the material [83], but a Hall bar creates narrow channels for charge carriers to flow, thus reducing overall error.

A diagram of a Hall bar is shown in Figure 4.9. Current can be injected between contacts 1-4, and resistivity can be measured between contacts 2-3 and 5-6, while the Hall voltage can be measured between 2-6 and 3-5.

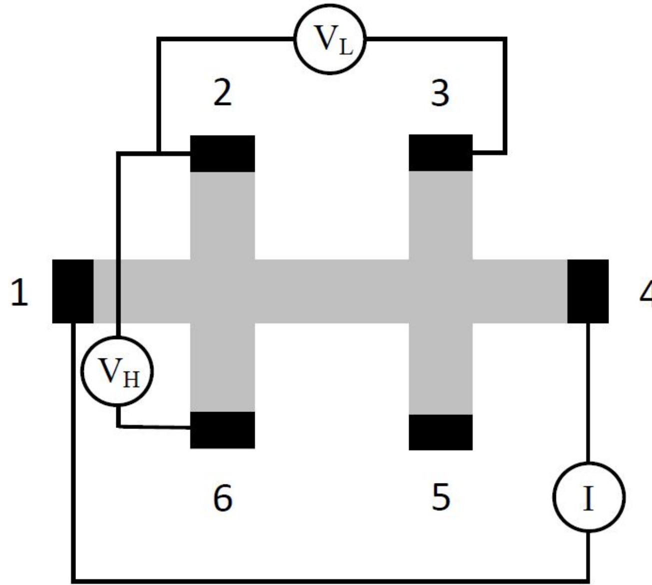

Figure 4.9: Diagram of a Hall bar sample geometry.

In these experiments, Hall bars were fabricated using the University of Michigan Lurie Nanofabrication Facility. Initially, the cap layer of HgCdTe is etched away using a bromine/methanol solution, leaving only the buffer and absorber layers. The Hall bar pattern is defined using photolithography, and surrounding material is etched away using a hydrobromic acid etch. The material is etched down to the insulating CdZnTe substrate so that current is only allowed to flow within the Hall bar structure. Ti/Au ohmic contacts are then deposited.

Experiments were conducted both at the University of Michigan, using the Physical Property Measurement Systen (PPMS) Dynacool by Quantum Design, and also at Northwestern University using the Cryogen-Free Measurement System from Cryo-

genics Limited. These tools offer a range of temperatures from 500 mK to 300K, and magnetic fields that can reach 16T.

4.2.2 Initial MCF Experiments

Variable field Hall and the MCF procedure were applied to multiple HgCdTe samples with a similar structure to Figure 4.8. The results of the multi-carrier fit at 77K for samples L1.a and L1.b are shown in Figure 4.10. Deviations in the fit at small magnetic fields are due to the low density of data points in those regions, and these issues were resolved in later measurements. In both samples, two electron carriers were resolved, one with a density in the low 10^{15} cm^{-3} range, and another near 1×10^{14} cm^{-3}.

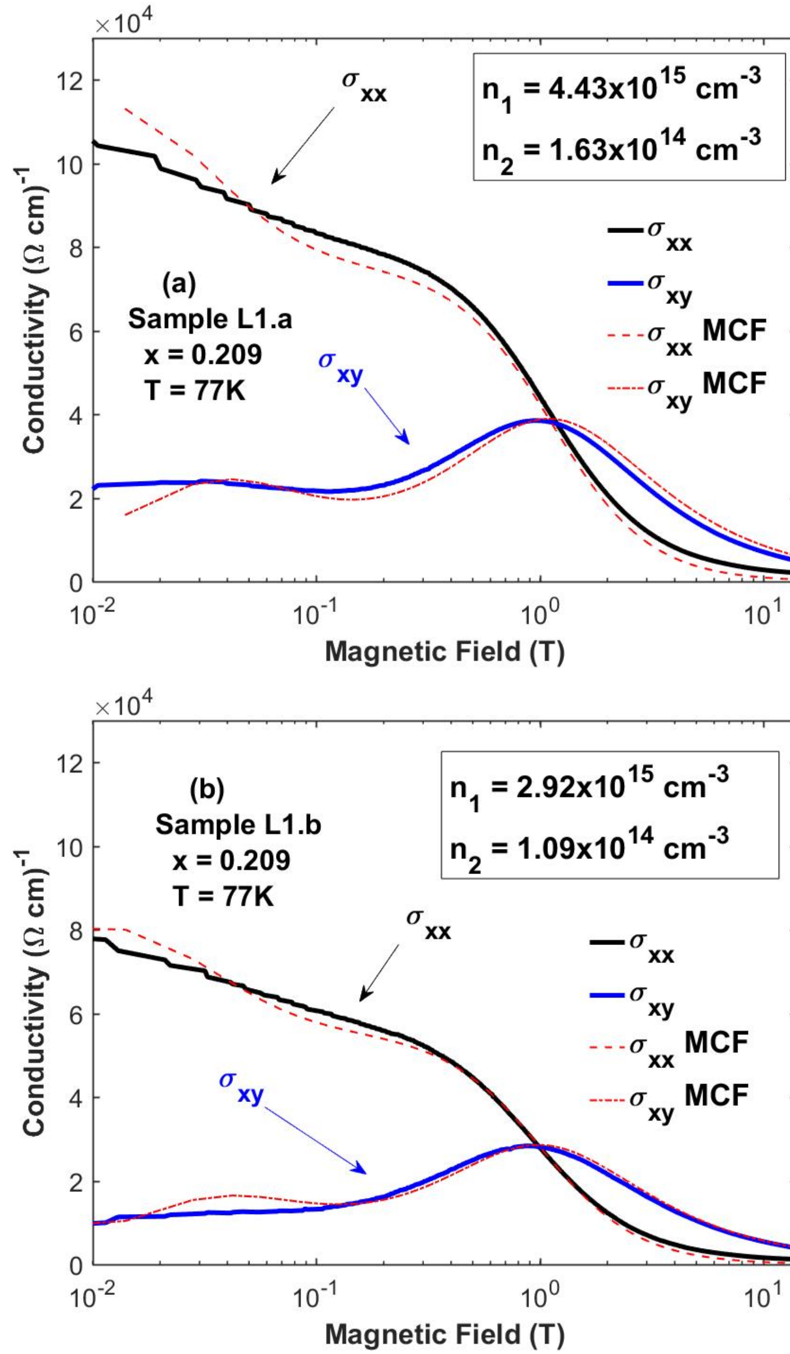

Figure 4.10: Multi-carrier fits to σ_{xx} and σ_{xy} for two HgCdTe samples at 77K. [21]

Temperature dependent measurements were conducted, and both carrier density and mobility were extracted. The temperature dependent carrier density is compared

against Equation 4.21, where n_i is the intrinsic carrier density and N_d is the extrinsic doping level. The doping level in the absorber region follows the intrinsic level until approximation 80K. Temperature dependent mobility is compared to the standard, composition dependent empirical model for HgCdTe (from Rosbeck and Starr [84]) described in Equation 4.22. Figure 4.11 shows the comparison between measured temperature dependence and the standard models for sample L1.b.

$$n(T) = \frac{N_d}{2} + \sqrt{\frac{N_d^2}{4} + n_i^2} \tag{4.21}$$

$$\mu = \frac{9 \times 10^8 (\frac{0.2}{x})^{7.5}}{Z^{2(\frac{0.2}{x})^{0.6}}} \text{ where} \tag{4.22}$$

$$Z = T \text{ if } T > 50K$$

$$Z = \frac{1.18 \times 10^5}{2066 - |T - 35|^{2.07}} \text{ if } T < 50K$$

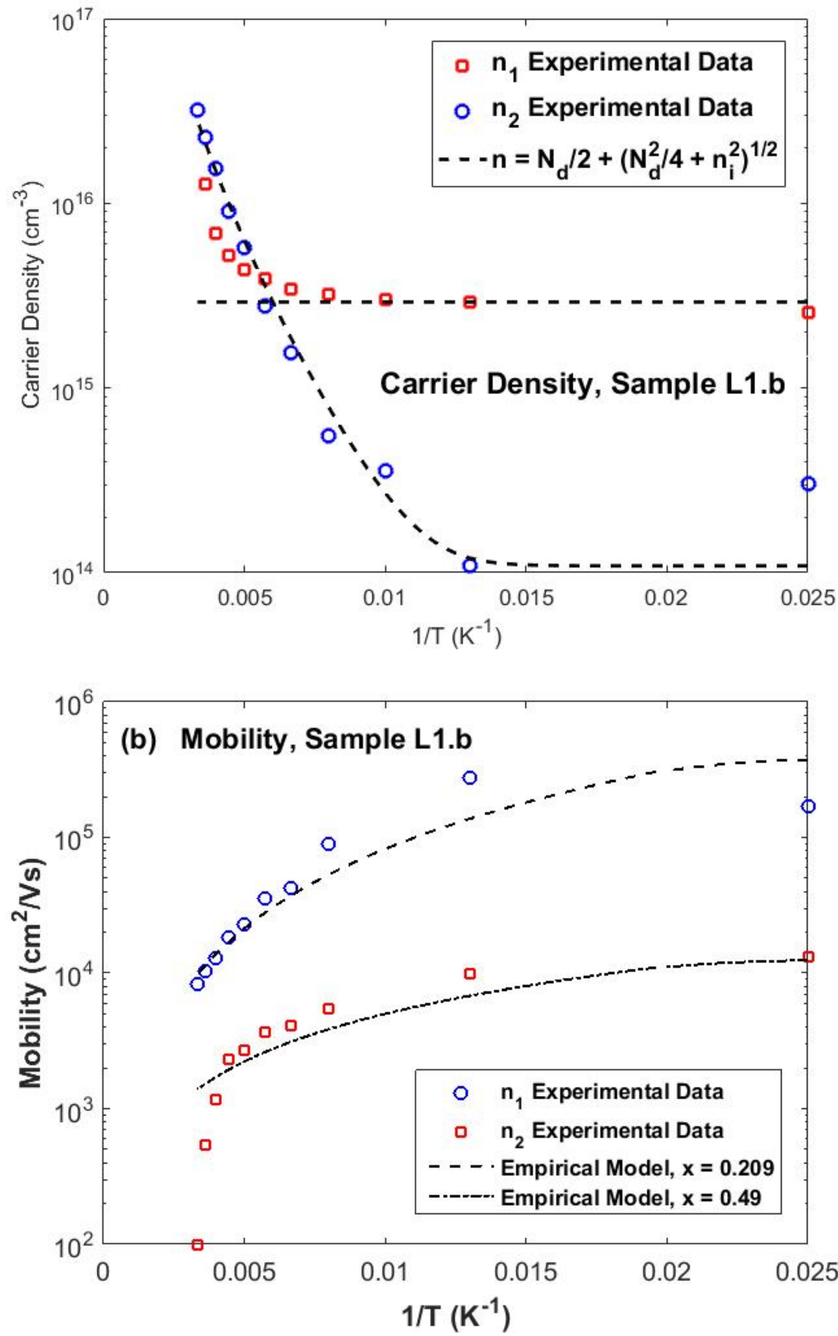

Figure 4.11: a) Carrier concentration versus temperature data for sample L1.b. b) Mobility versus temperature data for sample L1.b [21]

The volume carrier densities were calculated by dividing the sheet carrier densi-

ties by the individual layer thicknesses. These values vary among samples but are approximately 8-10 μm for the absorber layers, and 1-3 μm for the buffer layers. One potential issue that can skew these results is a large depletion region at the interface between the buffer and absorber layers. This was investigated using the standard equation for the depletion layer width [59], and the diffusion layer width was found to be less than 0.1 μm, and was thus not included in the calculations.

Secondary Ion Mass Spectroscopy (SIMS) was used to verify the concentration of indium atoms (n-type dopant) in each layer. While SIMS identified concentrations of $n = 2\times10^{15}$ cm^{-3} and 5×10^{13} cm^{-3} in the two layers, measured values in the absorber layer were in the low 10^{14} range, indicating that some small level of background n-type dopant is still present, potentially caused by impurity ions (aluminum, arsenic, antimony, etc) [11] or point defects.

Another method used to verify that each layer (absorber vs buffer) matched the predicted growth properties was to analyze the temperature dependent carrier density in the intrinsic regime. The intrinsic carrier concentration can also be expressed by Equation 4.23, and by plotting ln(n_i) vs 1/T, the effective bandgap E_g can be extracted from the slope. This method produced a bandgap of 0.105 eV in the absorber region for Sample L1.b, which is consistent with a LWIR HgCdTe device with cutoff greater than 11 μm.

$$n_i = \sqrt{N_c N_v} e^{\frac{-Eg}{2k_B T}} \tag{4.23}$$

For comparison, additional measurements were conducted on higher doped MCT samples (absorber layer doping ranged from mid 10^{14} to low 10^{15}). MCF was still able to identify both carriers, but the mobility values at 77K ($\mu = 102,000$ cm^2/Vs) were lower than the low doped samples ($\mu = 275,000$ cm^2/Vs) by roughly a factor

of 2, which is a larger deviation than predicted by the empirical model ($\mu = 126,000$ and $137,000$, respectively). The temperature dependent results for the higher doped sample (H1) can be seen in Figure 4.12.

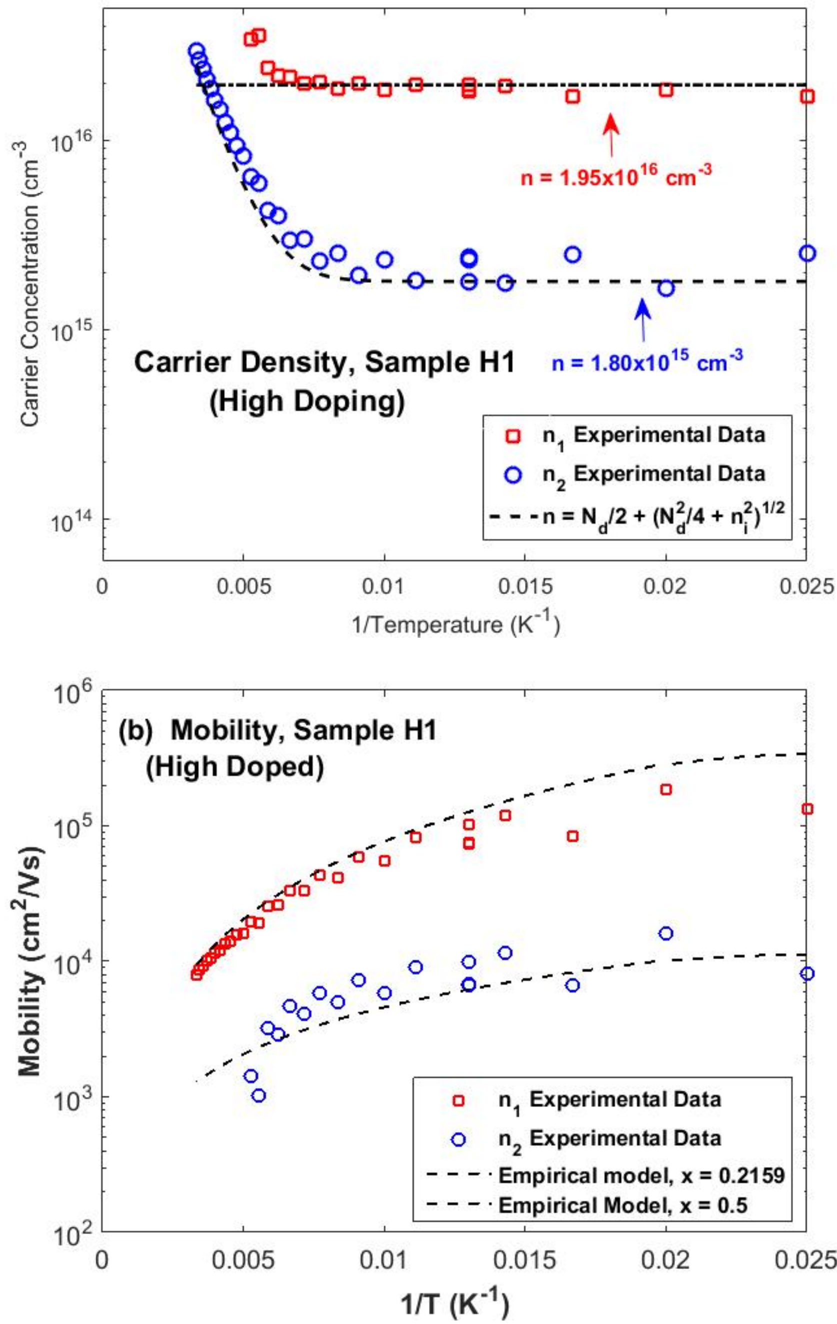

Figure 4.12: a) Carrier concentration versus temperature data for sample H1. b) Mobility versus temperature data for sample H1 [21]

Another factor that was predicted to significantly impact carrier transport was the

post-growth, high temperature Hg anneal. This is necessary to fill excess Hg vacancies that are present immediately after growth, but it is also anticipated that this anneal can alter both the device structure and transport properties due to interdiffusion at the high anneal temperatures. Samples L1.a and L1.b were annealed at Teledyne under 3 different conditions: 300C for 6 hours, 250C for 12 hours, or 200C for 96 hours. Results of the annealing study, as well as full results of the van der Pauw and multi-carrier fit at 77K can be seen in Table 4.1 [21].

Sample	Anneal Temp. (°C)	Anneal Time (h)	4-point Hall (77 K) n (cm^{-3})	4-point Hall (77 K) μ (cm^2/Vs)	Multi-carrier fit (77 K) n_1 (cm^{-3})	Multi-carrier fit (77 K) μ_1 (cm^2/Vs)	Multi-carrier fit (77 K) n_2 (cm^{-3})	Multi-carrier fit (77 K) μ_2 (cm^2/Vs)
L1.a	200	96	2.0×10^{15}	23,500	4.43×10^{15}	8800	1.63×10^{14}	282,000
L1.b	300	6	–	–	2.92×10^{15}	9800	1.09×10^{14}	275,000
L2.a	200	96	1.8×10^{15}	22,000	3.03×10^{15} [a]	7800 [a]	2.79×10^{14} [a]	90,000 [a]
L2.b	250	12	–	–	3.18×10^{15} [a]	6000 [a]	1.40×10^{15} [a]	35,000 [a]
L2.c	300	6	–	–	3.12×10^{15}	7400	8.59×10^{14}	42,000

The lower annealing temperatures show an improved mobility value in both samples. [a] Values extracted at 70 K instead of 77 K.

Table 4.1: Comparison of MCF results alongside van der Pauw, 4-point Hall effect measurements for 3 different anneal conditions. [21]

It can be seen that mobility shows an increase at 77K compared to samples with higher doping levels, a result that is not predicted via the empirical mobility model. Also, the various annealing temperatures did not have a significant impact on the overall carrier transport properties, indicating that the longer, low temperature anneals yield similar results to the standard, shorter high temperature anneals.

4.2.3 FMSA + MCF Experiments

The multi-carrier fitting procedure is a very robust analysis technique for extracting transport information in multi-layered structures. However, the assumption of the type and number of carriers must be correct in order to yield sensible data. This works in many situations, but fails when attempting to analyze samples with mixed conduction or surface carriers, as those are typically not consistent from sample to sample. In order to address that issue in low-doped HgCdTe, where low level background p-type doping may be present, Fourier-domain Mobility Spectrum Analysis (FMSA) is used in conjunction with MCF to first identify the type and number of carriers.

Experiments were conducted on samples with a similar structure (see Fig 4.8) to previous studies. The σ_{xx} and σ_{xy} were calculated in the standard way, then FMSA was applied to fit the measured conductivity tensor data, as shown in Figure 4.13. The resulting mobility spectrum is shown in Figure 4.14. Conductivity peaks corresponding to the expected mobility values for the buffer and absorber layer are present, as well as some contribution from a low mobility hole species as well. There are other features in the mobility spectrum that are relevant. There is a high mobility peak at 10^6 cm^2/Vs that is present in every fit that is assumed to be a boundary condition artifact of the fitting procedure. There are other peaks present in the

simulation, largely focused in the low mobility regions. These peaks have a low conductivity (below 10^{-6} S, and thus do not contribute significantly to the conduction, and are thus ignored for this analysis.

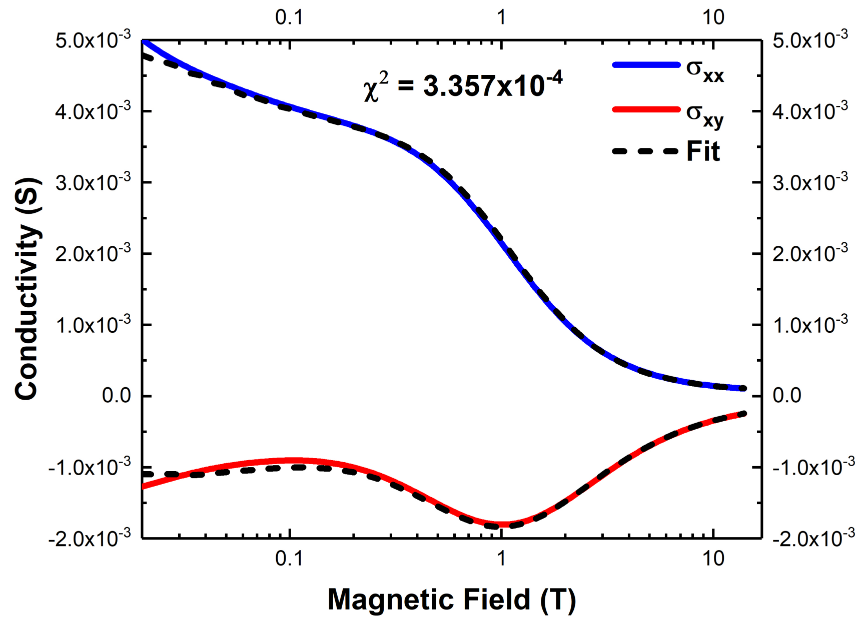

Figure 4.13: FMSA fit to measured σ_{xx} and σ_{xy} data for a representative HgCdTe sample [8]

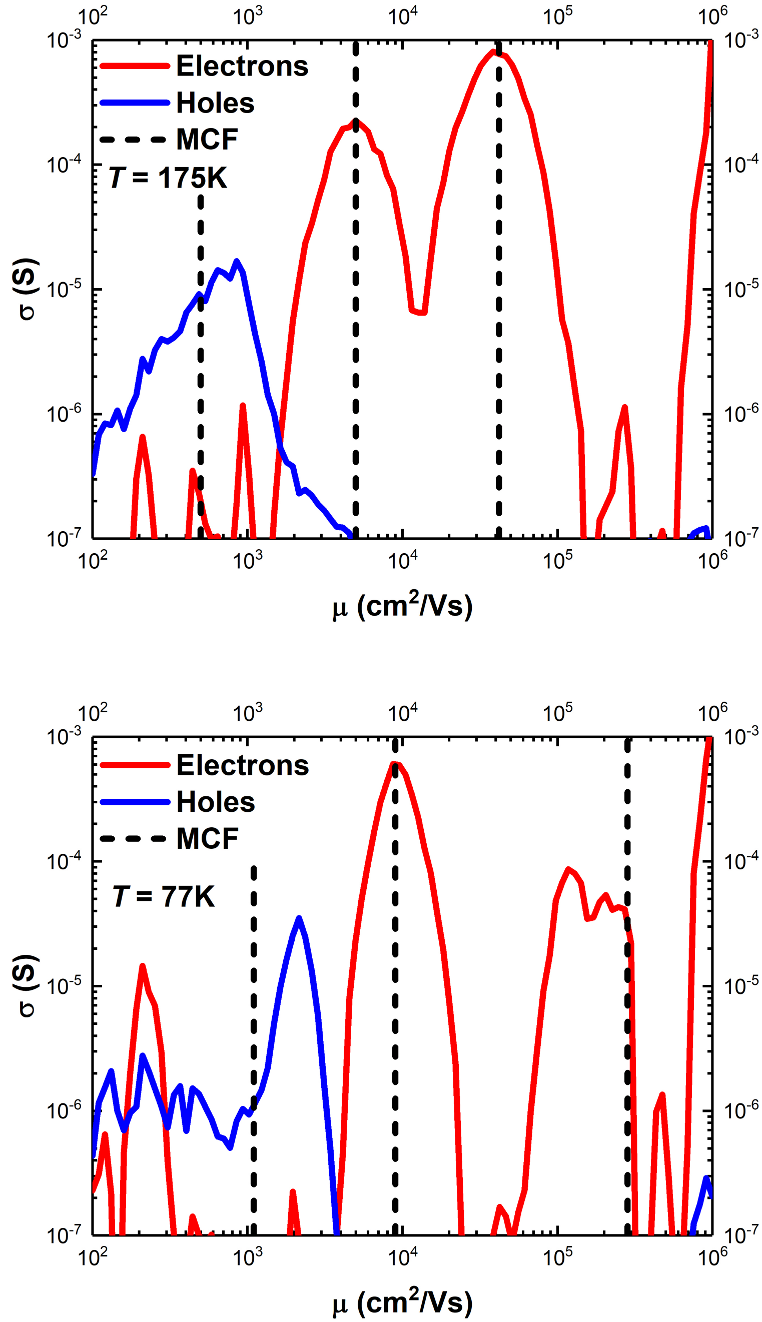

Figure 4.14: Mobility spectra for a representative sample taken at two different temperatures (175K and 77K). The two primary electron peaks correspond to the buffer and absorber layers, and a significant low mobility hole peak is also present. [8]

The carrier information obtained from the FMSA analysis is then used as an initial guess for the MCF procedure. The results of the MCF analysis are displayed in Table 4.2. Here, the hole density is displayed as a sheet density, as the exact location of these carriers can not be extracted from this analysis. The electron densities are reported as volume carrier densities, as the layer thicknesses have been verified from growth data and independently via Fourier transform infrared spectroscopy (FTIR).

77 K	n_1 (cm^{-3})	μ_1 (cm^2/Vs)	n_2 (cm^{-3})	μ_2 (cm^2/Vs)	p (cm^{-2})	μ_p (cm^2/Vs)
vdP	2×10^{15}	23400	n/a	n/a	n/a	n/a
FMSA	4×10^{15}	11000	1×10^{14}	150000	4.7×10^{11}	1800
FMSA + MCF	4.17×10^{15}	9000	1.43×10^{14}	284000	1.06×10^{12}	1100

Table 4.2: Comparison between Van der Pauw, FMSA, and MCF results for a representative low doped HgCdTe sample. [8]

Temperature dependent measurements were also conducted on a representative sample utilizing the MCF + FMSA procedure. The electron carrier density follows Equation 4.21 (Figure 4.15), but the mobility values are consistently higher than expected based on the empirical model in Equation 4.22. While a low mobility hole species is visible in the low temperature (77K) measurements, it is not clearly present at higher temperatures, likely due to an even lower mobility.

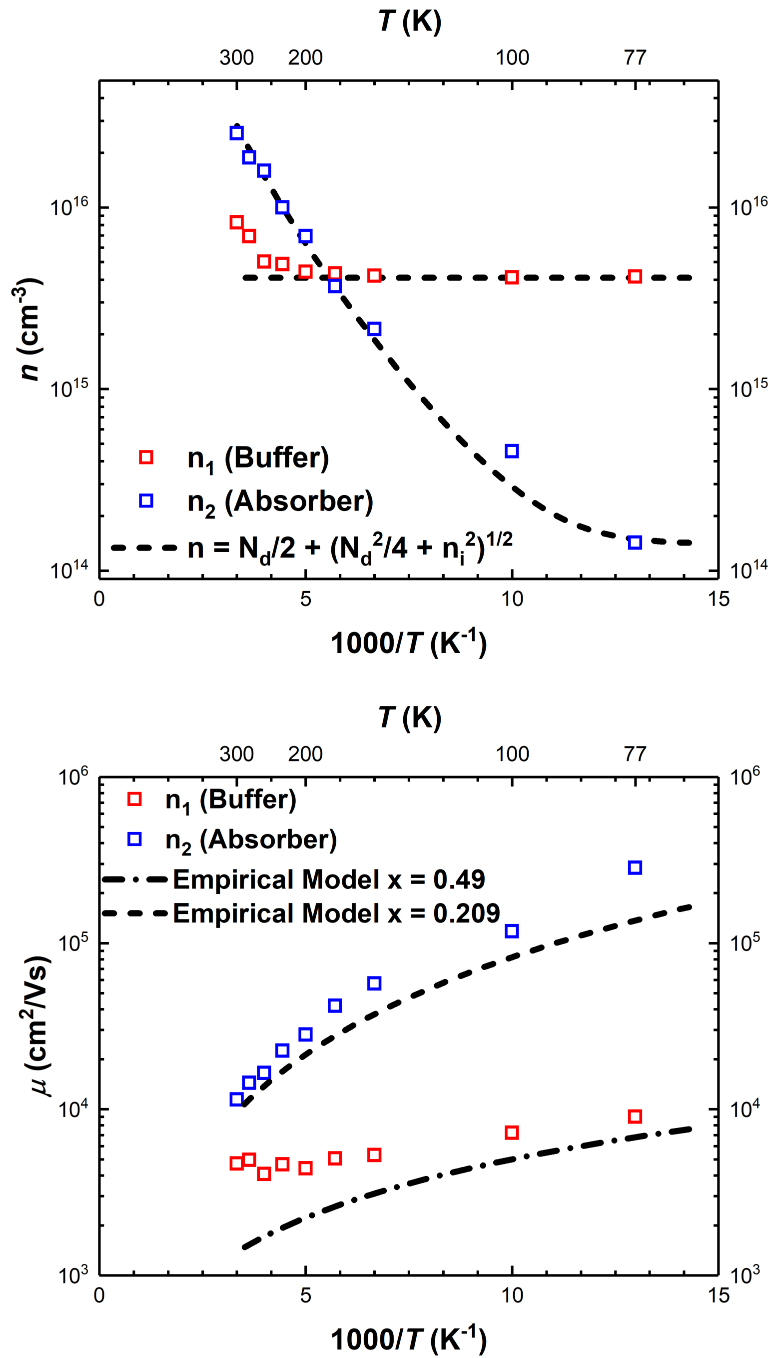

Figure 4.15: a) Carrier density vs reciprocal temperature and b) mobility versus reciprocal temperature [8]

4.2.4 Mobility Analysis

To understand the deviation from the mobility model, the empirical mode was examined in depth. The layers were bulk grown via liquid phase epitaxy (LPE), have a variety of compositions, and the doping levels are all approximately 10^{15} cm^{-3}. Modern material has higher quality, which may lead to better mobility at similar compositions to those used for the empirical model.

The mobility values were also compared against a values computed using a first principles model based on the various scattering mechanisms in HgCdTe. Polar optical phonon, neutral impurity, ionic impurity, and alloy scattering are all contributing factors to the mobility. Expressions for each mechanism are derived from Kinch [31]. At higher temperatures, the dominant scattering mechanism is polar optical phonon scattering, given by Stratton's expression [85]

$$\mu_{POP} = \left(\frac{k_B\Theta}{2m^*}\right)^{1/2} \left[\exp(\gamma_o) - 1\right] / F_0 \tag{4.24}$$

where $k_B\Theta = 0.0176$ eV is the optical phonon energy, $\gamma_o = \Theta/T$, and $F_0 = \left[\frac{1}{\epsilon_{inf}} - \frac{1}{\epsilon_s}\right] \frac{m^* q k_B \Theta \pi}{\epsilon_0 h^2}$. As the temperature is decreased near cryogenic temperatures ($\sim$ 77K), alloy scattering begins to limit the mobility. Alloy scattering arises due to atomic disorder between the Hg and Cd sites. In HgCdTe, composition dependent alloy scattering is defined by

$$\mu_{Alloy} = \frac{qh}{4\pi^2 x(1-x)\Delta E_c^2 \rho(E) m^*} \tag{4.25}$$

where where $\Delta E_c = 1.5eV$ is the different between the s atomic term values of the Hg and Cd atoms, and $\rho(E)$ is the density of states in the conduction band.

At very low temperatures, ionized impurity scattering is the dominant mechanism.

This mechanism is caused by carriers scattering off of the stationary ions that are present as a result of dopant ionization. This can play a major role in high doped materials, but is largely minimized in low doped HgCdTe. Mobility due to ionized impurity scattering is given by

$$\mu_{Ion} = \frac{3.2 \times 10^{‘5} \epsilon^2 T^{3/2}}{N(m^8/m_0)^{1/2}} \left[\frac{\ln(3.7 \times 10^{14} T^2 \epsilon (m^*/m_0))}{n} - 1 \right] \tag{4.26}$$

where N is the number of ionized impurities and n is the carrier density. Neutral impurity scattering was also considered, although it does not appear to be a limiting mechanism at any temperature. Scattering due to these impurities is given by Equation 4.27, where N_n is the density of neutral impurities. A comparison between all relevant scattering mechanisms is shown in Figure 4.16, and the maximum predicted mobility at 77K for low-doped, LWIR HgCdTe is 5.3×10^5 cm^2/Vs.

$$\mu_{Neutral} = \frac{1.44 \times 10^{22} (m^*/m_0)}{\epsilon N_n} \tag{4.27}$$

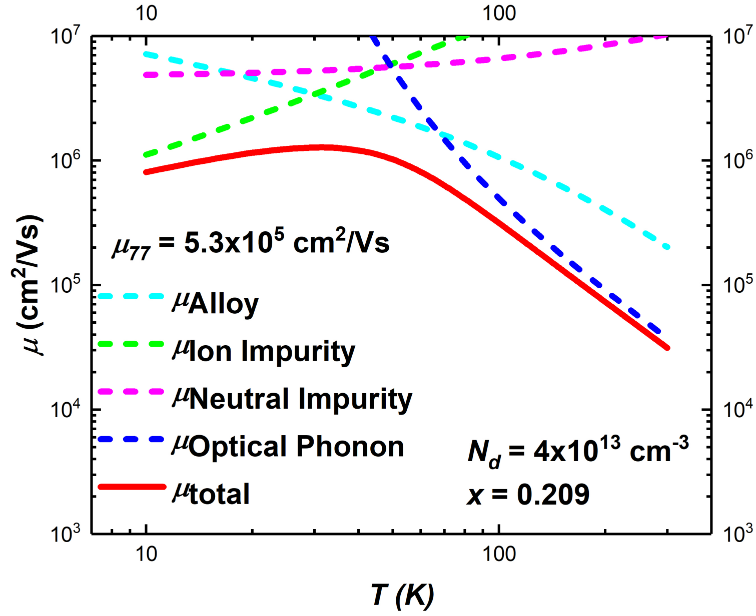

Figure 4.16: Mobility for LWIR HgCdTe with x=0.209 and $N_d = 4 \times 10^{13}$ cm^2/Vs based on alloy, ionized impurity, neutral impurity, and optical phonon scattering. [8]

While the mobility values measured in these low-doped HgCdTe layers are higher than anticipated based upon the empirical mobility model, they are still within the expected range based on scattering theory. This is demonstrated in Figure 4.17.

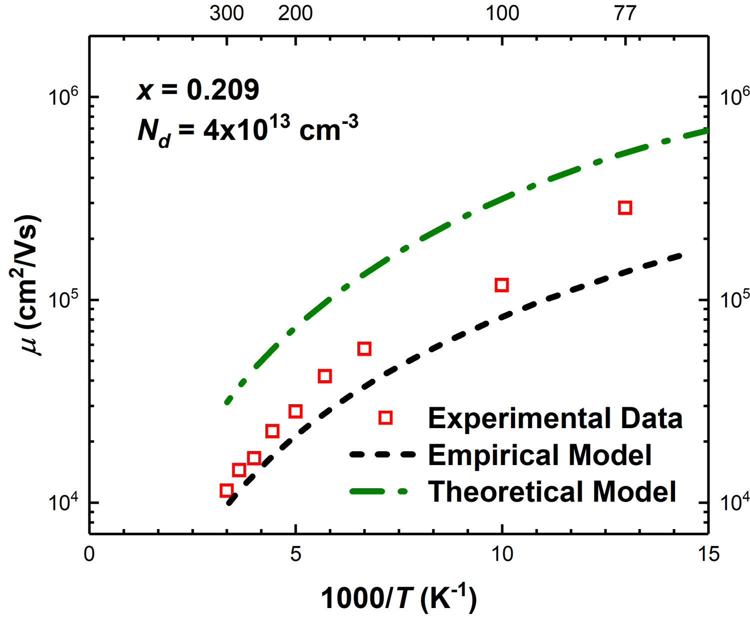

Figure 4.17: Comparison between measured mobility values, empirical model in Equation 4.22, and theoretical scattering model. [8]

4.2.5 Quantum Hall Effect

In order to gain more detailed information about the quality and accuracy of the HgCdTe structure, Hall measurements were conducted at very low temperatures (as low as T = 500 mK) on low-doped HgCdTe with similar layer structure. Figure 4.18 shows a calculated band diagram for the specific material structure utilized in these experiments. Electron confinement is possible at the absorber/buffer layer interface at 3 μm, resulting in the formation of a two-dimensional electron gas (2DEG). In a 2DEG, the allowed energy levels for electrons are quantized due to the quantum confinement. Additionally, an applied magnetic field also leads to further splitting of the energy levels. These combined effects lead to quantization of measured resistance values as well. The allowed resistance values correspond to plateaus in the measured

Hall resistivity as a function of magnetic field. The Hall resistance is quantized according to Equation 4.28, where ν is the Landau level [86].

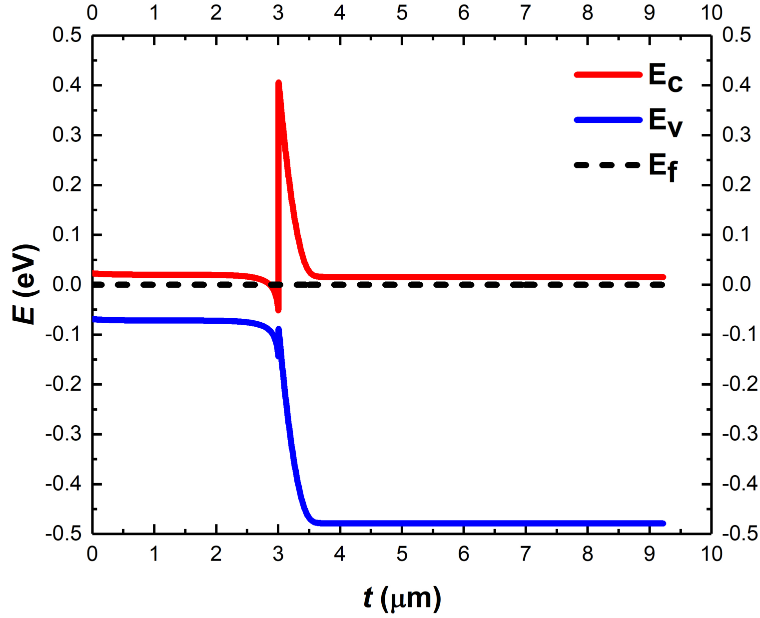

Figure 4.18: Calculated band diagram for low-doped, LWIR HgCdTe absorber layer on top of wide gap, HgCdTe buffer layer. 2DEG formation is possible at the interface at 3 μm. [8]

$$\rho_{xy} = h/\nu e^2 \tag{4.28}$$

The plots of transverse and longitudinal magnetoresistivity measurements were able to display the quantization of the Hall resistivity, as seen in Figure 4.19. This quantization was visible at temperatures as high as 5K. It is worth noting that although no explicit quantum well structure was defined and no gate voltage was applied, quantum confinement is still evident at the interface. Quantum oscillations were already apparently at a magnetic field of $B = 1T$, which corresponds to mo-

bility values of $\mu \approx 1/B = 1$ m^2/Vs $= 10,000$ cm^2/Vs. These properties indicate both excellent material quality and high crystallinity, as defects and disorder near the interface would lower the overall mobility.

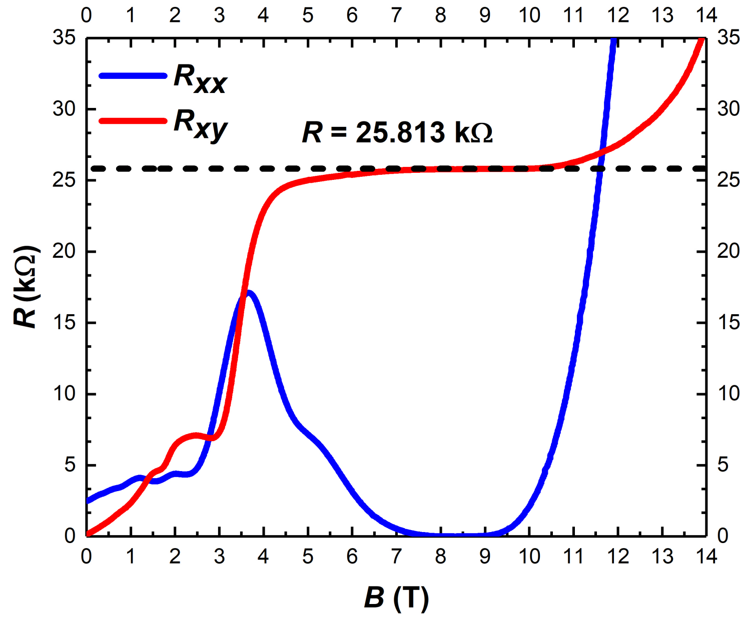

Figure 4.19: Measured resistance vs magnetic field at $T = 500mK$. [8]

Chapter 5

II-V T2SL Properties

Infrared detectors designed to operate in the Short Wave Infrared range (SWIR) have a wide variety of applications, including military and defense, ground and space based astronomy, and laboratory based spectroscopy and imaging. More recently, Light Detection and Ranging (LiDAR) experiments have developed a need for more advanced SWIR detectors, specifically for autonomous car applications. Traditional SWIR materials, such as InGaAs, and HgCdTe, are ideal for most applications, but have limitations in detection range and cost that limit certain uses. Type II superlattice detectors based on III-V material systems offer a novel way to extend the wavelength range of traditional III-V detectors, without the additional cost associated with HgCdTe.

5.1 SWIR Technology

5.1.1 InGaAs

Indium Gallium Arsenide (InGaAs) is a standard infrared detector material. Some of the earliest uses of InGaAs were for linear detector arrays in space-based imaging applications [87, 88]. The most common composition, $In_{0.53}Ga_{0.47}As$, can be grown

lattice matched to InP substrates, and has a bandgap of 0.73 eV at room temperature, corresponding to a cutoff wavelength of 1.7 μm [89]. In recent years, this wavelength range has made it a desirable material for the telecommunications industry, which requires detectors optimized for the 1.55 μm lasers utilized in fiber optic cables.

InGaAs is versatile not only due to it's convenient absorption range, but also due to the high quality of available material. It is easily grown via MOCVD [90] with low defect counts. Measured quantum efficiency is consistently as high as 80-90% across the entire wavelength range, and dark current densities are consistently below 1 μA/cm, as displayed in Figure 5.1 [22].

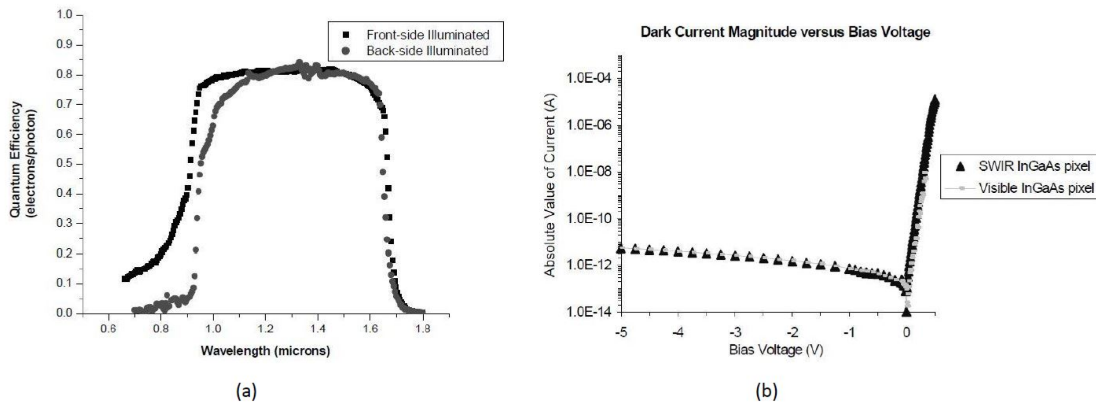

Figure 5.1: a) Quantum efficiency as a function of wavelength and b) Dark current as a function of bias voltage for standard SWIR InGaAs focal plane array [22]

One significant drawback of InGaAs detectors is difficulty covering the entire SWIR wavelength range. The SWIR band is defined by a transmission window in the atmospheric spectrum, which extends out to nearly 3 μm. Lattice matched InGaAs can only cover part of that range. InGaAs can be modified to absorb at the wavelength by altering the composition, utilizing "Extended-range InGaAs". However, as seen in Figure 5.2, altering the composition to reach wavelengths as long as 2.6

μm requires indium compositions greater than 80%, which leads to significant lattice mismatch on InP substrates, which can degrade material quality, decrease quantum efficiency, and increase the associated SRH dark current density. [30, 91]

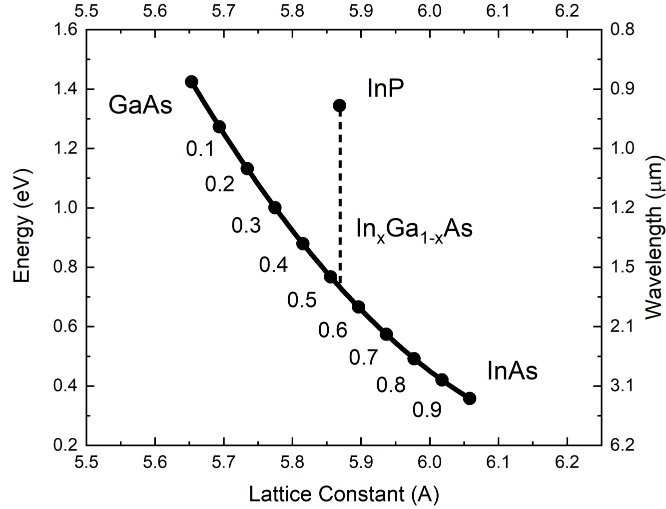

Figure 5.2: Tie diagram displaying lattice constant of InGaAs at various compositions, compared to lattice constant of InP

5.1.2 HgCdTe

Mercury Cadmium Telluride is also used for infrared detection in SWIR band. By varying the composition, the bandgap can be tuned to cover the entire SWIR range, giving MCT more versatility than other common SWIR materials. Typical HgCdTe has very high quantum efficiency and low dark current density in the SWIR regime, even at temperatures at or near room temperature. For very high performance applications, such as space based astronomy, HgCdTe is the material of choice because it is reliable and versatile. However, the significant cost of Cadmium Zinc Telluride (CdZnTe, or CZT) substrates ($ 5,000-10,000 per substrate) and the manufacturing limitations (only a handful of companies worldwide with ability to grow high quality

MBE HgCdTe) make the use of MCT detectors in small-scale applications not cost effective.

Many attempts have been made to reproduce the detector quality of MCT on CZT. Alternative substrates, such as Si or GaAs, have been considered due to the lower cost and availability of material. However, the lattice mismatch between $Hg_{0.7}Cd_{0.3}Te$ and GaAs is 14%, and 19% for Silicon. There is also a significant mismatch between the coefficient of thermal expansion in these alternative materials as well, as displayed in Figure 5.3 [23]. These discrepancies manifest as a decrease in material quality, yielding etch pit densities (EPDs) that are 2 orders of magnitude higher than those for traditional HgCdTe on CdZnTe substrates.

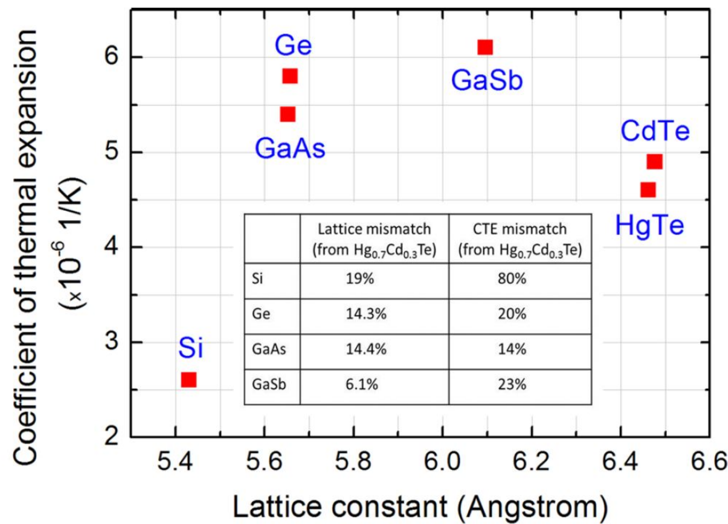

	Lattice mismatch (from $Hg_{0.7}Cd_{0.3}Te$)	CTE mismatch (from $Hg_{0.7}Cd_{0.3}Te$)
Si	19%	80%
Ge	14.3%	20%
GaAs	14.4%	14%
GaSb	6.1%	23%

Figure 5.3: Plot of Lattice Constants and Coefficient of Thermal Expansion (CTE) for various materials that have been considered as alternative substrates. [23]

Although SWIR HgCdTe on alternative substrates has decreased material quality, detectors have been fabricated and displayed performance comparable to other SWIR technologies. Detectors with quantum efficiency as high as 80-90% and dark current

density near 10^{-5} A/cm^2 (Figure 5.4) [24] have been realized on silicon substrates. While these alternative substrates decrease the total cost of MCT detectors, it still remains a significant challenge to mass produce MCT arrays in a cost effective manner, and other material systems for SWIR are being explored.

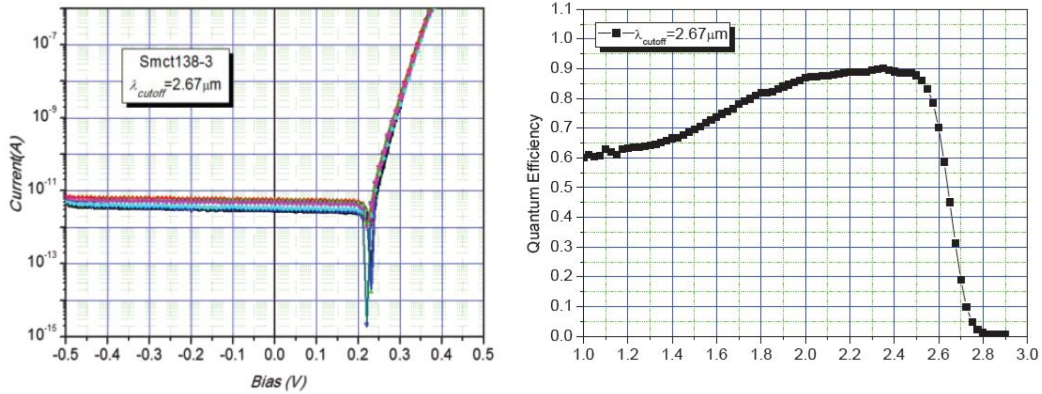

Figure 5.4: Plot of dark current density and quantum efficiency for HgCdTe/Si with $\lambda_c = 2.67\mu m$ fabricated into FPAs with a 30 μm pitch. [24]

5.2 Development of Type II Superlattices

A newer technology that has been utilized for infrared detection is based on a multi-quantum well structure, also known as a superlattice. A superlattice is a periodic array consisting of alternative layers of two different materials [92]. The thicknesses of these materials are typically on the order of nanometers, leading to a band structure consisting of periodic quantum wells, an example of which is seen in Figure 5.5 [25].

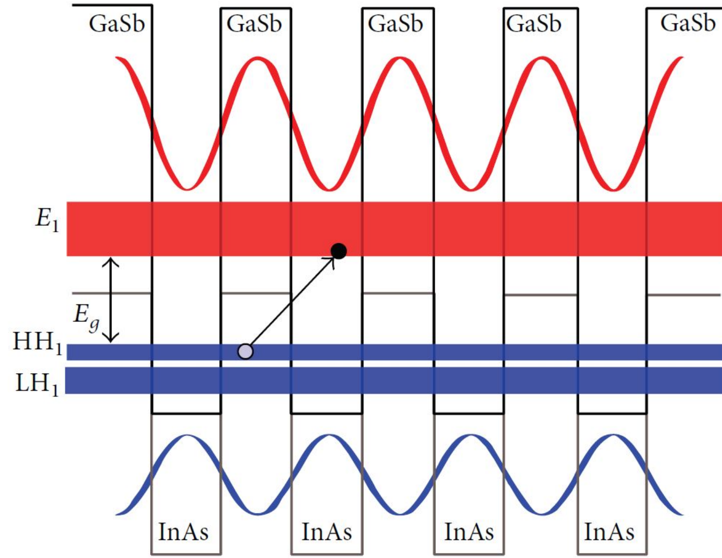

Figure 5.5: Band alignment for a standard InAs/GaSb superlattice. [25]

There are many key features of superlattice detectors that make them an attractive candidate as a replacement for existing technologies. They are fabricated using mature III-V growth technology, so there is not a significant technical challenge to overcome regarding growth. Also, these devices offer significant control over the effective bandgap. The bandgap is determined by transitions within energy levels in the quantum wells rather than by the bandgaps of the constituent materials. By simply varying the layer thicknesses, the bandgap can be varied significantly. Also, by utilizing a type-II band alignment, the effective bandgap can be significantly smaller than the gaps in the component materials, which is of significant relevance for MWIR and LWIR devices, or for extending the range of SWIR detectors.

However, superlattice materials do have drawbacks that require more research to overcome. In a multi-quantum well structure, the wavefunctions for electrons and holes peak in physically different locations, indicating that electrons and holes are spatially separated. This causes an indirect optical transition, leading to significantly

weaker absorption. Thicker superlattices are required to see comparable absorption to bulk materials, which can introduce additional defects and decrease the SRH lifetime. Also, since carriers must move vertically through the superlattice to be collected, transport is critical. However, depending on the geometry of the device, transport may occur via miniband conduction (with reasonable mobility) or other methods such as phonon-assisted tunneling or well-to-well carrier emission and capture.

5.2.1 InAs/GaSb based Superlattices

Some of the earliest superlattice detectors to be pursued are based on the InAs/GaSb material system. This structure was proposed in 1987 as an alternative for HgCdTe in the MWIR and LWIR regimes, using a superlattice of InAs/InGaSb. These superlattices were grown on GaSb substrates where they could be grown nearly lattice matched and leverage existing III-V technology. The previously mentioned properties of superlattices already presented an advantage over MCT, but the most significant advantage for the superlattice was the addition of strain, leading to strained-layer superlattices (SLS). Strain between individual layers in the superlattice leads to a splitting between the light and heavy hole valence bands. This is significant as it is an effective method for suppressing Auger recombination, the dominant source of dark current in the MWIR and LWIR IR detectors. Strain causes a separation in carriers in those bands, making momentum conservation in the 3 carrier Auger process much less likely, thus significantly decreasing the rate of Auger recombination. (Figure 5.6).

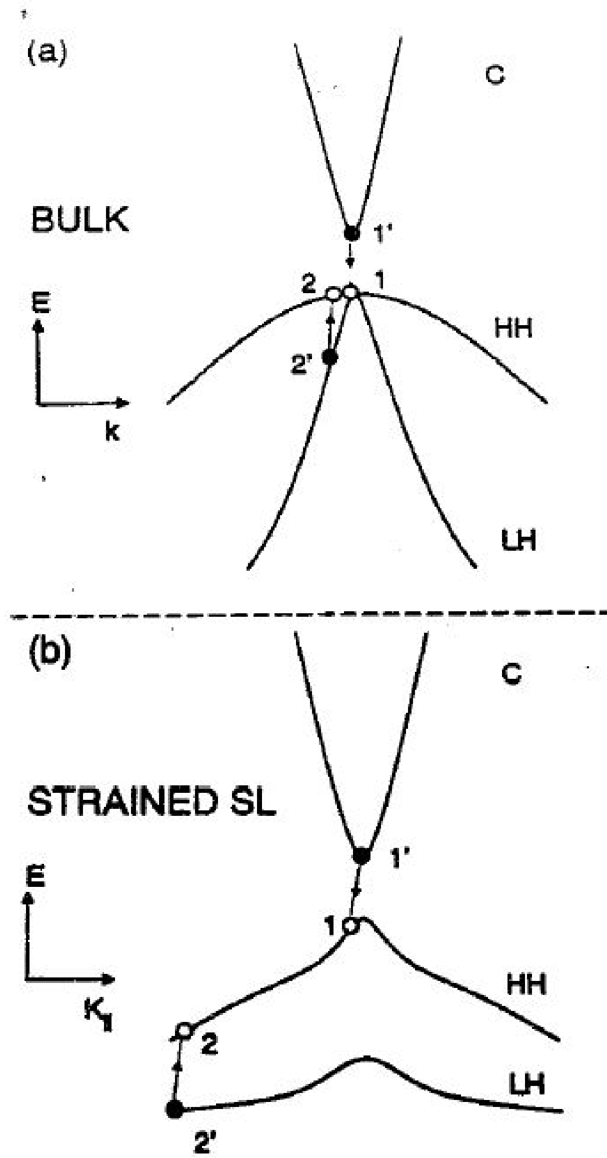

Figure 5.6: Dispersion relation comparison between bulk HgCdTe (a) and a strained InAs/InGaSb superlattice (b). [26]

Various architectures based on this system have been utilized. Superlattices consisting of InAs/GaSb [93, 94] and InAs/InGaSb [26, 95] have both been utilized successfully. Barrier detectors based on this III-V SLS technology have also been demonstrated [72]. Current drawbacks include fabrication issues related to surface roughness

and thickness variability across the full superlattice, especially among structures with many hundreds of periods [93].

5.3 SWIR Type II Superlattices

Infrared detectors based on superlattices have primarily been considered for MWIR and LWIR applications, but recently superlattices are being researched for SWIR detection as well. SWIR T2SL detectors offer the ability to tune the bandgap to access the entire SWIR wavelength range similar to HgCdTe, while being based on III-V materials lattice matched to InP that have a significant cost savings compared to HgCdTe.

The longer wavelength InAs/GaSb based SLS system was designed to reduce Auger recombination, but Auger is not the leading recombination source in SWIR devices. Short-wave devices are typically dominated by SRH recombination, although typical SWIR devices are still able to operate at or near room temperature. A comparison of the dark current sources in MWIR and LWIR HgCdTe is shown in Figure 5.7 [27].

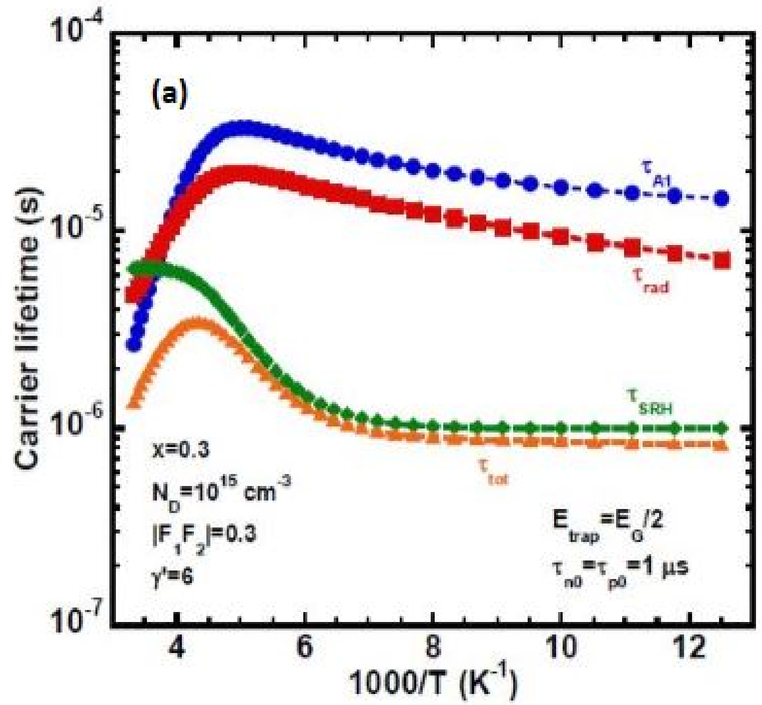

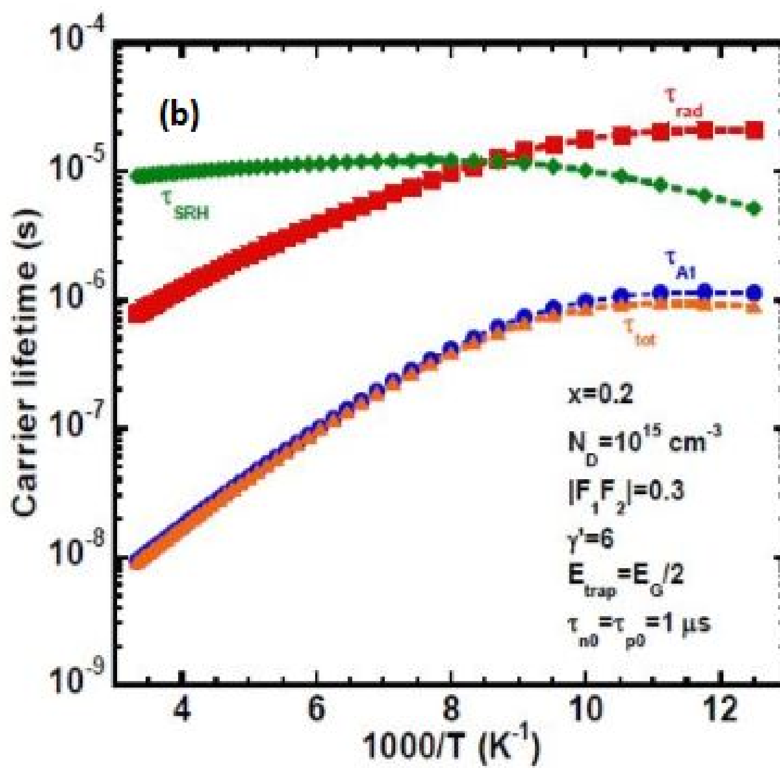

Figure 5.7: Comparison of carrier lifetime mechanisms in a) MWIR HgCdTe which is dominated by SRH recombination and b) LWIR HgCdTe which is dominated by Auger recombination [27]

While suppressing Auger recombination is not a primary concern for SWIR detectors, the other properties of superlattices can potentially be useful for SWIR detectors. Specifically, precise control of the bandgap is possible via bandgap engineering. This allows for III-V compounds to be able to absorb light at wavelengths greater than 2.5 μm. Also, the mature III-V growth technology allows for access to high quality material, in contrast to the limited number of high quality HgCdTe manufacturers. However, other challenges are present that are not apparent in standard SWIR materials. The absorption properties can vary in superlattices, and are generally lower than that of a bulk material. Also, similar to MWIR/LWIR SLS detectors, growth variability can lead to defects and increase SRH recombination.

Even with these challenges present, SWIR detectors based on superlattice technology are still a promising area of research. Various SWIR detectors have been fabricated using III-V growth technology. References [28, 96–101] provide a review of current SWIR T2SL technology. The majority of devices are based on InGaAs and GaAsSb superlattice layers, grown on InP substrates. Many of these devices are able to push the cutoff wavelength out to $2.4 - 2.6$ μ m while maintaining lattice matching to InP. Dark current values range from 10^{-4} to 10^{-3} A/cm^2, which is one to two orders of magnitude higher than MCT with a similar cutoff.

Due to decreased absorption, responsivity and quantum efficiency are lower in these devices, with QE values up to 50-60% at wavelengths longer than 2 μm. Also, unlike traditional InGaAs and HgCdTe, superlattice absorption is based on quantum well transitions, which leads less abrupt cutoff at the bandedge. Quantum efficiency drops significantly at wavelengths below λ_C, so while cutoff values are higher, a detector would not have suitable absorption across it's entire available wavelength range. Representative examples of dark current density and quantum efficiency for superlattice detectors are shown in Figure 5.8.

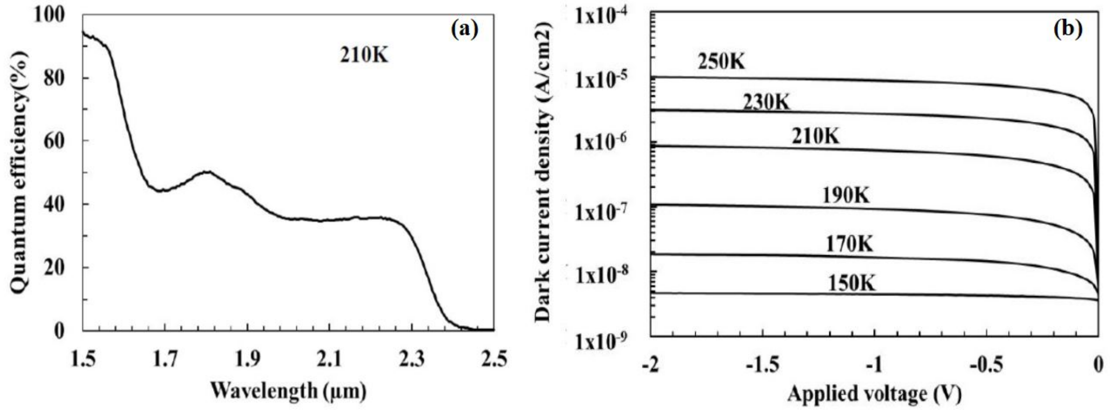

Figure 5.8: a) Quantum efficiency and b) dark current density of a InGaAs/GaAsSb type-II superlattice focal plane array with 200 μm diamater pixels. [28]

5.4 T2SL Device Modeling

In the following sections, details of a modeling study on SWIR T2SL infrared detectors is presented. Superlattices are comprised of alternating layers of Indium Gallium Arsenide (InGaAs) and Gallium Arsenide Antimonide (GaAsSb). Prior work on SWIR T2SL detectors has largely focused on these materials as they have mature growth and fabrication technology, and can also both be grown lattice matched to InP.

Two potential structures will be considered. The first set of simulations focuses on a superlattice composed of $In_{0.53}Ga_{0.47}As$ and $GaAs_{0.51}Sb_{0.49}$ layers, as both of these compositions are lattice matched to InP. The second set of simulations is comprised of strain balanced superlattices of varying InGaAs and GaAsSb compositions. Both structures are important as the latticed matched case is the simplest in terms of fabrication and should yield better material quality, while the strained-layer superlat-

tices offer more control over the bandgap and absorption properties. All superlattice simulations outlined in this study are performed in conjuction with the engineers at Princeton Infrared Technologies Inc.

To simulate device level performance, the superlattices were used as the absorbing layer a in p-i-n detector structure, as shown in Figure 5.9. The buffer and cap layers are comprised of $In_{0.53}Ga_{0.47}As$, and the substrate is InP. For comparison to other existing detectors, material parameters including effective bandgap, optical absorption spectrum, and recombination lifetimes were calculated and used to estimate the device quantum efficiency and dark current.

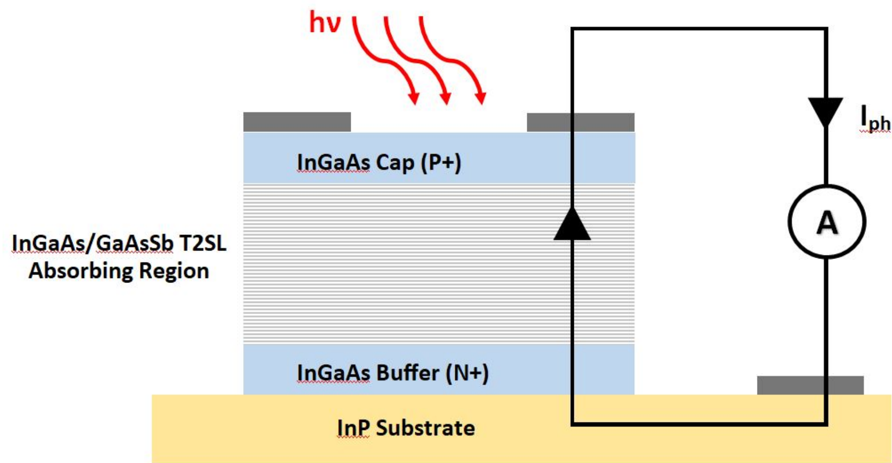

Figure 5.9: Standard device structure for simulating InGaAs/GaAsSb Type-II superlattice infrared detectors. Buffer and Cap layers are comprised of $In_{0.53}Ga_{0.47}As$, all grown on an InP substrate. [29]

5.5 InGaAs/GaAsSb T2SL Lattice Matched to InP

5.5.1 Effective Bandgap

The most critical parameter for superlattice detectors is the effective bandgap, E_g, which determines the final cutoff wavelength, λ_c. For T2SLs, the cutoff is not strictly determined by the the direct bandgap absorption of the two constituent materials, but rather by carrier transitions between allowed states of the quantum wells.

The allowed quantum states can be calculated via the use of 8 band **k·p** perturbation theory. This method takes into account the energy eigenstates of the conduction, heavy hole, light hole, and split off hole bands simultaneously. The **k·p** method is designed to solve the Schrodinger equation

$$H\Psi_n = E_n\Psi_n \tag{5.1}$$

for 8 different total states (accounting for the four bands previously mentioned, and also considering spin). The Hamiltonian describing this problem can be defined as an 8x8 matrix, and is generally solved via various numerical and computational techniques [102]. By determining the energy eigenstates, the effective bandgap, as well as all other allowed energy transitions, can be determined.

For the lattice matched case, the SWIR T2SL structure is comprised of alternating periods of 5 nm $In_{0.53}Ga_{0.47}As$/5 nm $GaAs_{0.51}Sb_{0.49}$. The electronic band structure of the superlattice was calculated using 8 band **k·p** perturbation theory. All **k·p** calculations were done using the nextnano++ software package (`www.nextnano.de`), developed by Dr. Stefan Birner [103]. Nextnano was used to calculate the energy eigenvalues and wavefunctions for the quantum well, and Figure 5.10 displays the energies and wavefunctions for the lowest electron level and highest hole level in each

well.

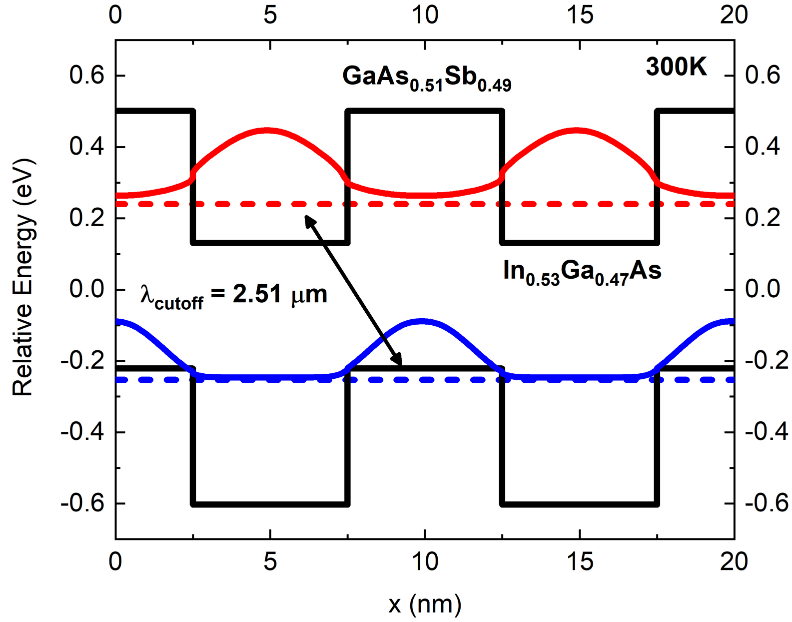

Figure 5.10: Band structure of the of 5 nm $In_{0.53}Ga_{0.47}As$/5 nm $GaAs_{0.51}Sb_{0.49}$ superlattice, displaying the lowest hole and higest electron energy level, as well as wavefunctions. The associated effective bandgap is 0.494 eV, corresponding to a cutoff wavelength of $\lambda_c = 2.51\mu$ m. [29]

The effective bandgap is calculated as the energy difference between the lowest electron energy level and highest hole energy level. For the 5 nm/5 nm lattice matched system at 300K, the effective bandgap is 0.494 eV, which corresponds to a cutoff wavelength of $\lambda_c = 2.51\mu m$. Nextnano was also used to calculate the energy-dispersion relation for the superlattice, which is displayed in Figure 5.11. The effective masses are calculated from the curvature of the bands at k=0, and values of $m_e^* = 0.045m_0$ and $m_h^* = 1.44m_0$ were extracted.

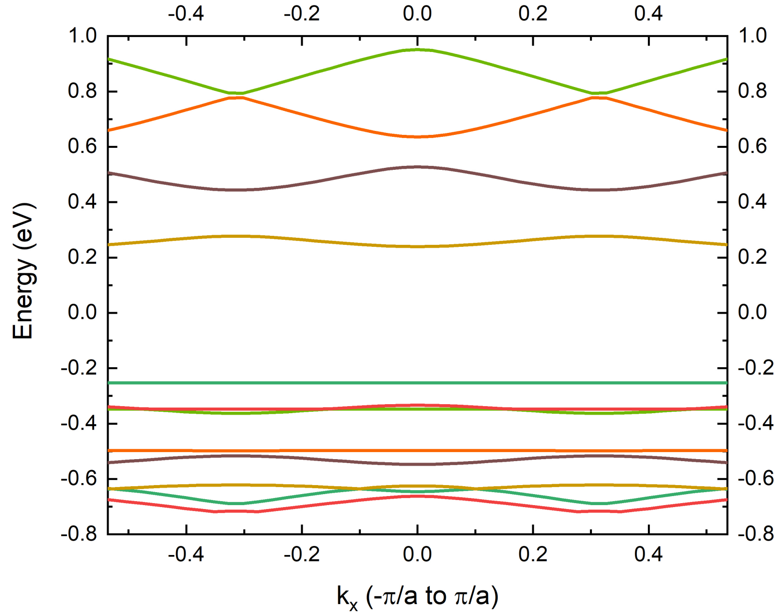

Figure 5.11: Calculated Energy dispersion relation for 5 nm $In_{0.53}Ga_{0.47}As$/5 nm $GaAs_{0.51}Sb_{0.49}$ T2SL.

5.5.2 Optical Absorption

The 8 band **k·p** method can also be used to determine the optical absorption spectrum for a superlattice structure. In a direct-gap, bulk material, optical absorption is typically very high for all energies above the bandgap, and abruptly drops to zero below the bandgap. Momentum changes are minimal as well, so there is very strong absorption as it is easy to generate electron hole pairs. In a superlattice, since absorption occurs via quantum well transitions, the overall absorption is weaker. Also, the absorption is generally weaker near the bandedge, as there are a limited number of electron and hole states available for each energy transition. This leads to lower quantum efficiency as well, as previously seen in Figure 5.8.

Obtaining the optical absorption spectrum can be accomplished in a similar man-

ner to the effective bandgap. After the energy levels have been determined from the 8 band **k·p** method, the absorption strength of each transition is determined by calculating the wavefunction overlap of the conduction and valence sub-band envelope wave functions [104]. Fermi's golden rule can then be used to calculate the full absorption versus energy spectrum via Equation 5.2, where E is the photon energy ($h\nu$), ϵ is the light polarization vector, and χ is the susceptibility tensor, which has components comprised of the wavefunction matrix elements.

$$\alpha = \frac{4\pi qE}{\hbar nc}\epsilon_i^* \chi_{ij} \epsilon_j^* \tag{5.2}$$

The optical absorption spectrum was also calculated using Nextnano's 8 band **k·p** simulator by assuming circularly polarized light normally incident onto the superlattice. The spectrum for the 5 nm/5 nm T2SL is displayed in Figure 5.12. The spectrum has a step function form, where each jump in absorption corresponds to a transition between different quantum well states.

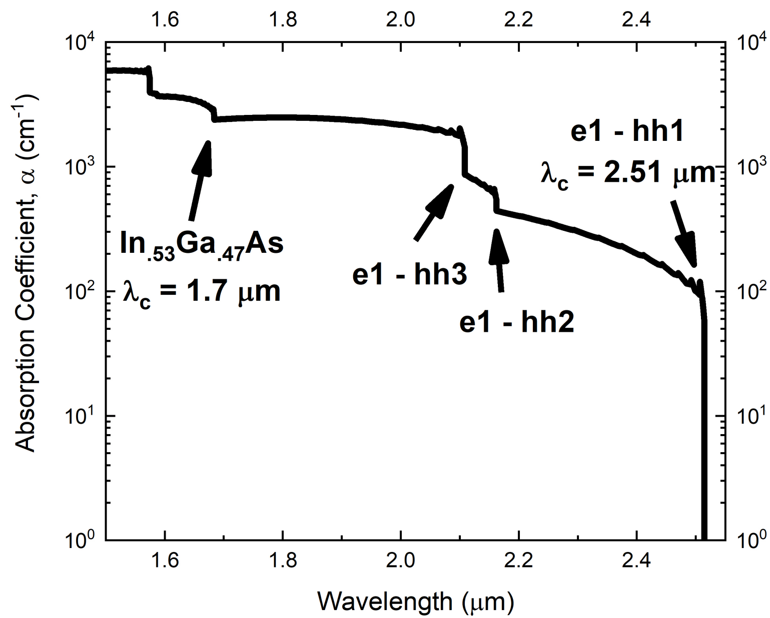

Figure 5.12: Absorption coefficient vs. wavelength diagram for 5 nm $In_{0.53}Ga_{0.47}As$/5 nm $GaAs_{0.51}Sb_{0.49}$ T2SL. Steps in the spectrum correspond to optical transitions between electron and hole energy levels. [29]

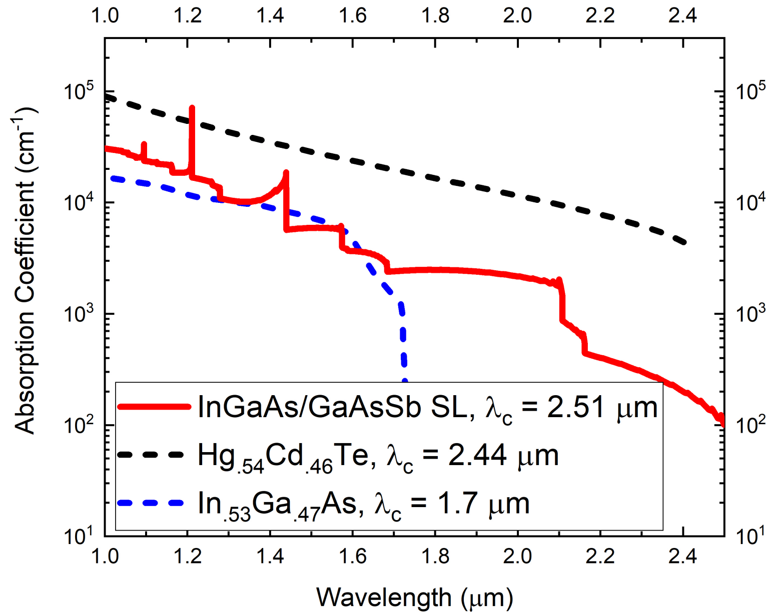

Figure 5.13: Absorption coefficient vs. wavelength diagram including InGaAs, HgCdTe and InGaAs/GaAsSb T2SL.

The relevant region of the absorption spectrum is $\lambda > 1.7\mu m$, as that is beyond the cutoff wavelength of standard $In_{0.53}Ga_{0.47}As$. Near it's cutoff, $In_{0.53}Ga_{0.47}As$ has an absorption coefficient between 10^3 and 10^4 cm^{-1}. Thus, in order to have reasonable quantum efficiency, the absorption coefficient for the superlattice must be of similar magnitude. Figure 5.13 displays a comparison of the absorption spectra for SWIR InGaAs, HgCdTe, and the InGaAs/GaAsSb superlattice. Beyond $\lambda = 1.7\mu m$, $\alpha \approx$ 2000 cm^{-1}, which allows for significant absorption until around 2 μm. The absorption drops significantly from 2 - 2.5 μm, but this result is promising for a SWIR T2SL that can absorb beyond standard InGaAs.

5.5.3 Carrier Transport

In order to understand the quality of a superlattice, carrier transport information is critical. At present, the carrier transport parameters are relatively uncertain in SWIR T2SL structures. If the wavefunction overlap between adjacent quantum wells is strong enough, then carriers form conduction and valence minibands, that operate similar to the conduction and valence bands in bulk semiconductors. Miniband conduction has the highest mobility values and is the desired conduction mechanism [105].

If miniband conduction is not present, the system is treated similar to a series of discrete quantum wells, and carriers can either move by tunneling mechanisms (such as phonon-assisted tunneling) or thermionic emission [106]. These have higher mobility as carrier transitions between wells are less probable via these methods. Figure 5.14 shows a summary of the various transport mechanisms.

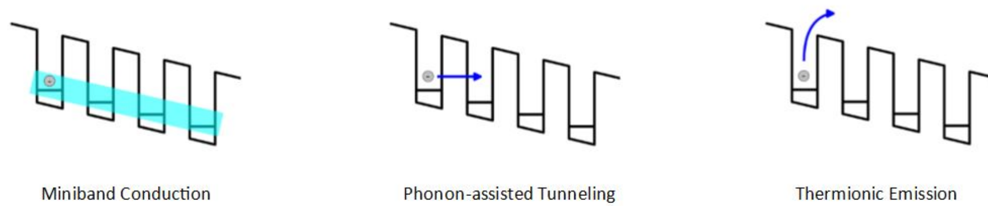

Figure 5.14: Diagram of various carrier transport mechanisms in a Type-II superlattice.

To determine what type of conduction may be present in SWIR T2SL detectors, the conditions necessary for miniband formation are considered. Minibands transport occurs through extended Bloch states that permeate through the various quantum

well layers. However, for miniband formation to be supported, the mean-free-path length of the carriers must be longer than the superlattice period [107], which is calculated via the inequality

$$\frac{\Delta d}{\hbar}\tau_h > d \tag{5.3}$$

where Δ is the miniband width, d is the superlattice period thickness, and τ_h is the scattering time, typically on the order of picoseconds. By extracting the miniband width from Fig 5.11 and using 10 nm as the period thickness, it was determined that miniband conduction is possible for electrons, but not for holes.

Although an exact calculation can not be made of the associated electron and hole mobility values cannot be made without more experimental data, approximations must be made in order to compute quantum efficiency via drift/diffusion models. For this study, mobility values of $\mu_e = 1,000$ cm^2/Vs and $\mu_h = 100$ cm^2/Vs were used, based on approximate values measured for MWIR and LWIR InAs/GaSb T2SL system [108, 109].

The effective mass can be calculated via 8 band **k·p** similar to the bandgap and absorption. Following the work of [110], the Hamiltonian used to calculate the bandgap can also be used to calculate an energy dispersion relation for the conduction and valence subbands in the superlattice, an example of which is shown in Figure **??**. The effective mass is extracted from the curvature of dispersion relation via Equation 5.4.

$$m^* = \left(\frac{\partial^2 E}{\partial^2 k}\right)^{-1} \tag{5.4}$$

5.5.4 Recombination Properties

The parameters necessary to understand dark current density are the minority carrier lifetimes due to Auger, Shockley-Read-Hall, and radiative recombination. In n-type semiconductors, the Auger recombination lifetime is dominated by the Auger 1 process, described in Equation 2.3.3. The carrier density in the superlattice was assumed to be $n = 1 \times 10^{16}$ cm^{-3}, and the overlap integral $|F_1 F_2|$ is taken to be 0.11. The calculated Auger recombination lifetime is $\tau_{A1} = 8x10^{-5}$ s, or $80\mu s$. For SWIR devices, Auger recombination is not predicted to be the dominant recombination source.

Radiative recombination is calculated via Equations 2.18 and 2.19. Unlike Auger and SRH which depend on growth and design, radiative recombination is largely fixed, and is generally considered a fundamental limit for carrier lifetime. The calculated radiative recombination lifetime is $\tau_R = 2.3 \times 10^{-6}$ s or 2.3 μs, over an order of magnitude shorter than the Auger lifetime.

Shockley-Read-Hall recombination is typically the limiting factor for SWIR IR detectors, as it requires very high quality material in order for the lifetime to be longer than the radiative lifetime. As SRH varies based on material quality, it is difficult to estimate a general value for τ_{SRH}. Equation 2.21 is generally used to estimate SRH lifetime, but in the absence of some of the necessary parameters, a simpler expression is used based on material properties that can be directly measured. The SRH lifetime is estimated by [59]

$$\tau_{SRH} = \frac{1}{\sigma v_{th} N_T} \tag{5.5}$$

where σ is the electron or hole capture cross section, and N_T is the SRH trap density. Since the trap density can vary significantly across different materials, τ_{SRH} is calculated for a variety of N_T values. Standard trap densities for InGaAs

($N_T = 5 \times 10^{14}$ cm^{-3}) [60, 111] are used as a starting point . Ji et. al also measured values for capture cross section in InGaAs ($\sigma_e = 5 \times 10^{-16}$ cm^{-2} and $\sigma_h = 2 \times 10^{-15}$ cm^{-2}) , which are used in the present simulation as well. Calculations were made for N_T ranging from 5×10^{12} to 5×10^{16} cm^{-3}, and the resulting τ_{SRH} vary by many orders of magnitude as a result. Figure 5.15 shows the temperature dependence of the SRH lifetime as a function of trap density, with the Auger and radiative lifetimes overlayed on top. It can be clearly seen that Shockley-Read-Hall will be the dominant recombination method unless very high quality material ($N_T \leq 10^{13}$ cm^{-3}) is achieved for the superlattice. Based on these calculations, the estimated minority carrier lifetime is 100 ns.

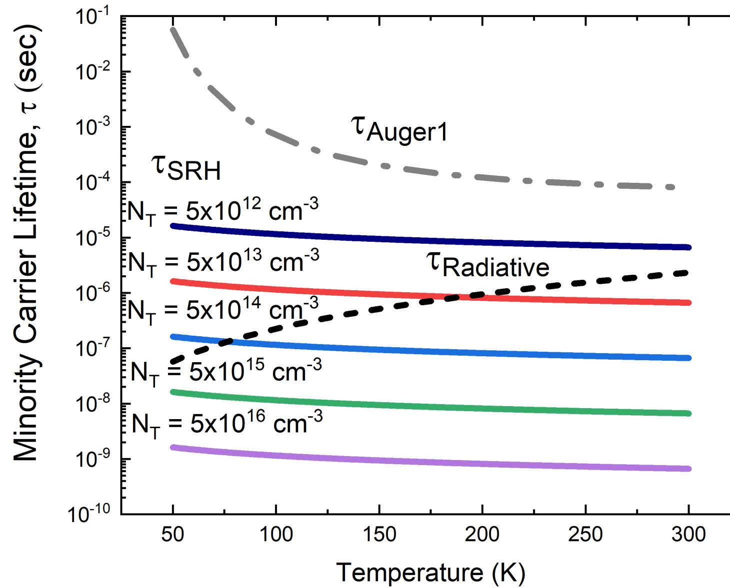

Figure 5.15: Minority carrier lifetime vs temperature including Auger, Radiative, and Shockley-Read-Hall recombination contributions. $\tau - SRH$ is plotted as a function of trap density, N_T [29]

5.5.5 Dark Current Density

Based on the minority carrier lifetime values, the associated dark current density for the superlattice can be estimated. For this SRH limited superlattice, the dark current density at room temperature is estimated to be 5×10^{-4} A/cm^2, which is more than an order of magnitude greater than the Rule 07 prediction for $\lambda_c = 2.2\mu m$, where $J_D = 1 \times 10^{-5}$ A/cm^2.

However, if the trap density is decreased below 10^{13} cm^{-3}, the device will become radiatively limited, and have a minority carrier lifetime at room temperature of more than 1 μs. A radiatively limited device would have a dark current density that is comparable to the Rule 07 prediction at room temperature, and is predicted to be lower than Rule 07 at temperatures near 250C, indicating that if material with high enough quality can be produced, a SWIR T2SL can theoretically match or outperform SWIR HgCdTe.

Figure 5.16 shows a visual comparison of SRH and radiatively limited T2SL dark current density compared with Rule 07 performance for $\lambda_c = 2.2\mu$m. For comparison, dark current data from an extended range $In_{0.83}Ga_{0.17}As$ detector ($\lambda_c = 2.6\mu$m) is included, and it has a dark density that is 3 orders of magnitude above the Rule 07 prediction [30]. This illustrates that although SRH limited SWIR T2SLs may not be comparable to Rule 07, they have the capability of outperforming other existing SWIR technology beyond $\lambda = 1.7\mu$m.

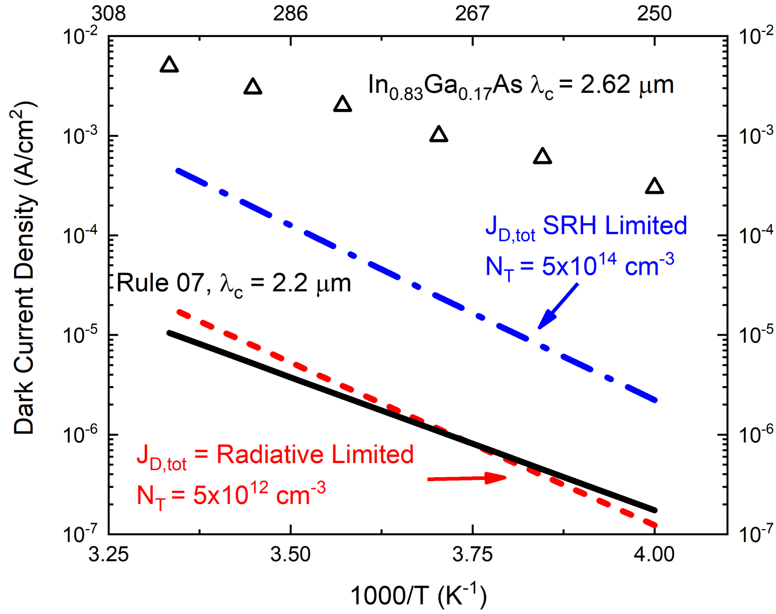

Figure 5.16: Dark current density vs inverse temperature including Shockley-Read-Hall and radiatively limited Type-II superlattices, extended range $In_{0.83}Ga_{0.17}As$, and the Rule 07 prediction for $\lambda_c = 2.2\mu m$ [29, 30]

5.5.6 Quantum Efficiency

Now that all relevant parameters (optical absorption, carrier transport, and minority carrier lifetime) have been calculated, the quantum efficiency of a T2SL device can be estimated. The InGaAs/GaAsSb T2SL is incorporated into a standard *p*-*i*-*n* device architecture. Simulations were conducted using the Synopsys Sentaurus TCAD software suite. To perform the simulations, the superlattice is treated as a bulk material with parameters described previously.

The simulations were performed for various T2SL absorber layer thicknesses, ranging from 2-6 μm. Results are shown in Figure 5.17 for the wavelength range beyond $\lambda = 1.7\mu m$. The quantum efficiency for a 3 μm absorber thickness ranges from 40-50%

out until near 2.1 μm, where the QE drops significantly, corresponding to the drop in absorption coefficient seen in Figure 5.12. For a thicker absorber (6 μm), more light is absorbed, leading to higher QE of 50-70%. For comparison, the quantum efficiency of a 2.2 μm cutoff $Hg_{0.51}Cd_{0.49}Te$ detector with a thickness of 4 μm is also plotted. Efficiency is very high for the MCT until the cutoff, where QE drops off rapidly.

The T2SL detector shows reasonable quantum efficiency for wavelengths between 1.7 and 2.1μm, especially for thicker absorbing layers. While this particular structure may not be suitable as a replacement for SWIR detectors beyond 2.1 μm, it has a lower dark current density than existing extended SWIR detectors, making it a viable alternative for certain SWIR applications.

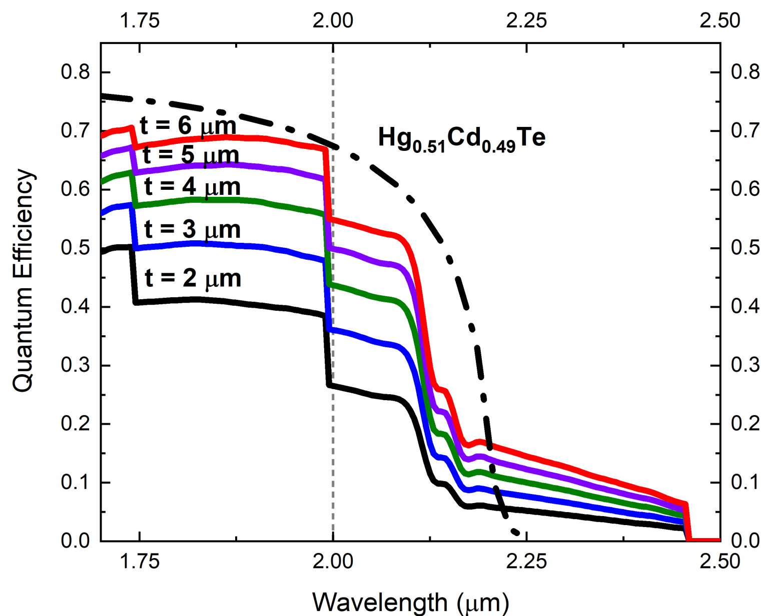

Figure 5.17: Quantum efficiency vs wavelength for 5 nm $In_{0.53}Ga_{0.47}As$/5 nm $GaAs_{0.51}Sb_{0.49}$ T2SL and $Hg_{0.51}Cd_{0.49}Te$ [29]

5.6 InGaAs/GaAsSb Strained-Layer Superlattice

InGaAs/GaAsSb type-II superlattices have been demonstrated to be a viable alternative for existing extended SWIR technologies. the superlattice composed of lattice matched InGaAs and GaAsSb shows improvement over other technologies, however the quantum efficiency drops significantly as you approach the cutoff wavelength, making the device only suitable for absorption out to wavelengths of around 2.2μm, even though the measured cutoff as 2.51μm. In order to alter the absorption and energy level properties, strain can be introduced between the individual layers in the superlattice.

5.6.1 Strain Balance

A strained-layer superlattice (SLS) is a structure where the lattice constant of each alternating constituent layer is different, introducing strain into the system. The layers alternate between tensile and compressive strain relative to the other, which can significantly alter the band diagram and material properties of a material.

In a standard material system where one material is grown epitaxially on another, if the lattice constants do not match, then the strain can lead to misfit dislocations and other defects, which degrade the material quality. To avoid this in the superlattice structure, strain balancing is utilized. By balancing out the compressive and tensile strain in each layer, the entire system will be grown with a single lattice constant.

In order for strain balance to occur, certain conditions must be satisfied. These conditions minimize the average strain energy of the superlattice, and more importantly provide zero average strain in the plane of the superlattice. The strain balance

conditions are given by

$$t_1 A_1 \epsilon_1 a_2 + t_2 A_2 \epsilon_2 a_1 = 0 \tag{5.6}$$

$$a_0 = \frac{A_1 t_1 a_1 a_2^2 + A_2 t_2 a_2 a_1^2}{A_1 t_1 a_2^2 + A_2 t_2 a_1^2} \tag{5.7}$$

$$A = C_{11} + C_{12} - \frac{2C_{12}^2}{C_{11}} \tag{5.8}$$

where a_0 is the substrate lattice constant, a_1 and a_2 are the superlattice lattice constants ($a_1 < a_0 < a_2$), t_1 and t_2 are the layer thicknesses, ϵ is the strain and A is an elastic parameter defined by C_{11} and C_{12} which are elastic stiffness coefficients for each material [112, 113].

For the InGaAs/GaAsSb system, in order to institute strain balance in a way that will extend the cutoff wavelength to longer values and increase overall absorption, the percentange of GaSb in GaAsSb must be increased, while the GaAs percentage in InGaAs must be decreased (Figure 5.18). If the thickness of each layer in the superlattice is known, then the strain balance equations can be used to calculate the required compositions for each material in order for the lattice constants to balance out the strain. Figure 5.19 depicts the composition combinations for various potential layer thicknesses.

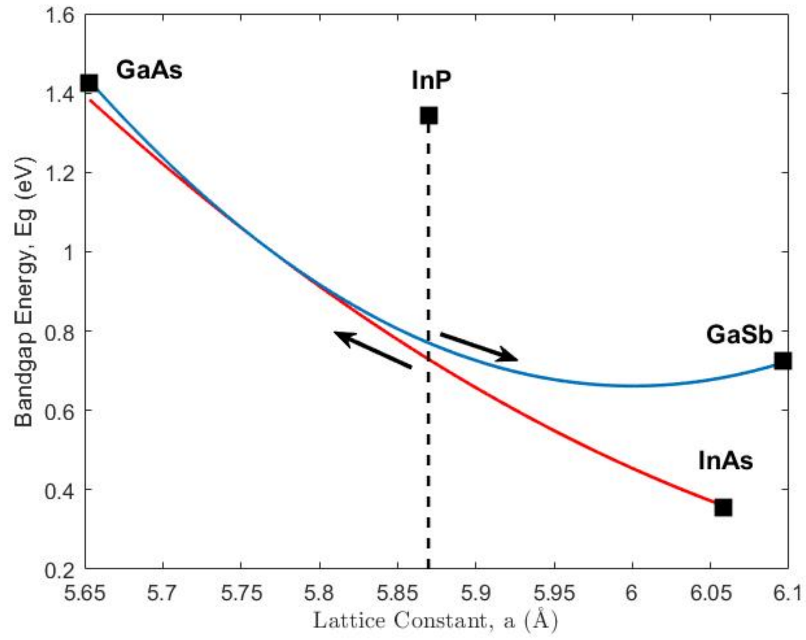

Figure 5.18: Tie diagram depicting the necessary changes for InGaAs and GaAsSb compositions in order to create a strained layer superlattice

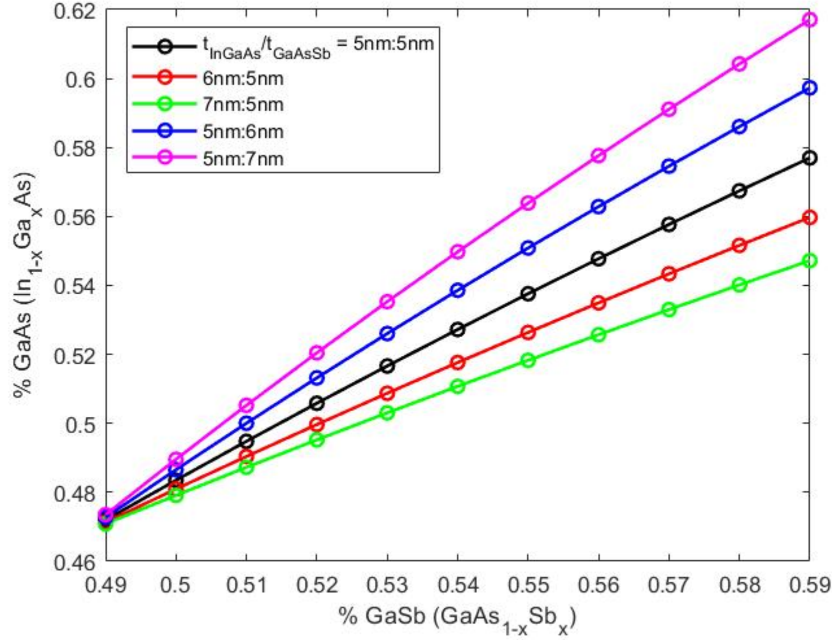

Figure 5.19: Allowed composition combinations for InGaAs/GaAsSb SLS with various layer thicknesses.

5.6.2 Desired SLS Structure

By utilizing the strain balance criteria, a plethora of potential superlattice structures are possible. The goal of choosing an SLS over a lattice matched superlattice is to extend the cutoff wavelength if possible, while increasing overall absorption near cutoff. This SLS structure has the additional constraint that as the lattice mismatch increases, the critical thickness, h_c, for pseudomorphic growth decreases, and beyond a certain composition, the critical thickness becomes smaller than the thickness of an individual layer.

To find a suitable material structure, 8 band $\mathbf{k}\cdot\mathbf{p}$ simulations were computed for all of the possible combinations, and the effective bandgap and optical absorption spectra were extracted in each case. Based on the measured lattice constants, the critical

thickness for each material combination was then calculated using the Matthews-Blakeslee model [114, 115]

$$h_c = \frac{b}{8\pi f}\frac{(1-\nu cos^2\theta)}{(1+\nu)cos\lambda}\left(\ln\frac{h_c}{b}+1\right) \quad (5.9)$$

where for a zincblende semiconductor, $b = a/\sqrt{2}$, $\nu = 1/3$ and $\theta = \lambda = 60\,\text{deg}$.

By comparison all of the possible structures, the optimal structure to balance absorption, effective bandgap, and critical thickness was determined to be 5 nm $In_{0.50}Ga_{0.50}As$ / 6 nm $GaAs_{0.49}Sb_{0.51}$. The effective bandgap of this system at 300K was calculated from Figure 5.20 to be 0.48 eV, corresponding to $\lambda_c = 2.58\mu m$.

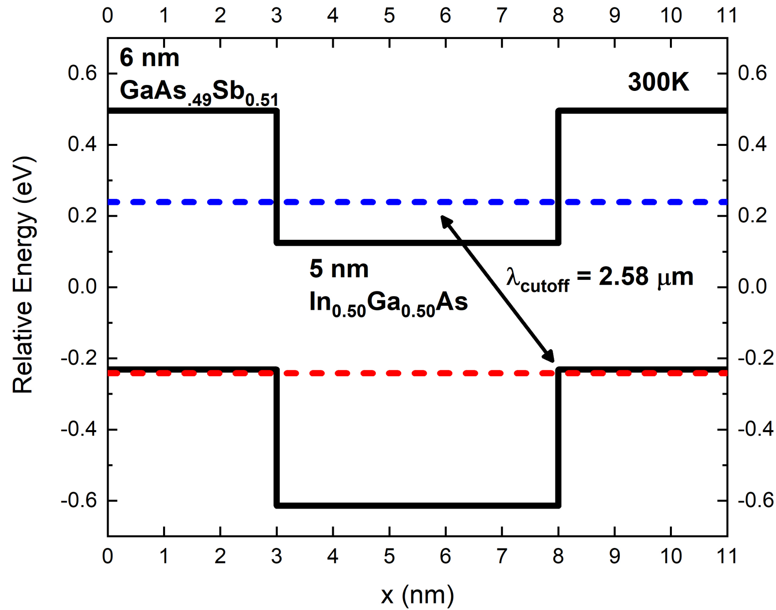

Figure 5.20: Calculated band diagram for 5 nm $In_{0.50}Ga_{0.50}As$ / 6 nm $GaAs_{0.49}Sb_{0.51}$ SLS system with $\lambda_c = 2.58\mu m$.

5.6.3 Optical Absorption

While the cutoff wavelength is not significantly longer than the lattice matched case, the absorption coefficient is higher, particularly in the region between 2-2.5 μm. The calculated absorption spectrum is displayed in Figure 5.21. The absorption coefficient is greater than 1000 cm^{-1} at all points up until the cutoff, indicating high quantum efficiency across the entire accessible wavelength range. Also, as this composition is not a significant deviation from the lattice matched composition, the strain is not significant enough to lower the critical thickness below the layer thickness. This is shown in Figure 5.22.

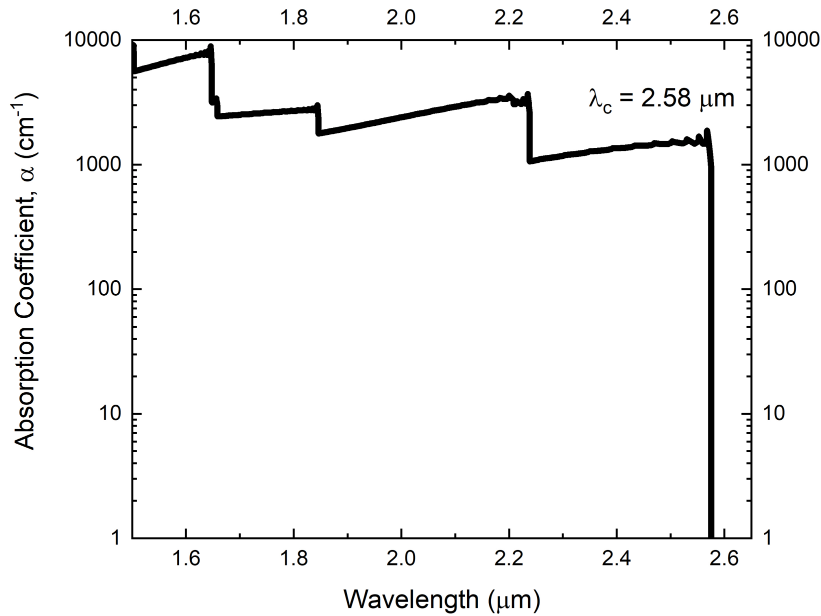

Figure 5.21: Calculated absorption spectrum for 5 nm $In_{0.50}Ga_{0.50}As$ / 6 nm $GaAs_{0.49}Sb_{0.51}$ SLS system with $\lambda_c = 2.58\mu$m.

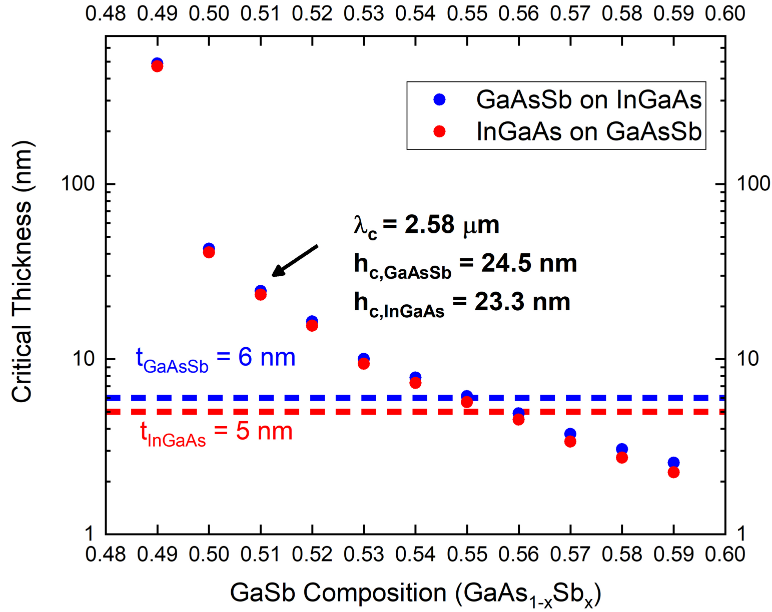

Figure 5.22: Critical thickness versus GaSb composition in $GaAs_{1-x}Sb_x$. Horizontal lines indicate SLS layer thicknesses.

5.6.4 Quantum Efficiency

The measured SLS structure and updated optical absorption spectrum were again input into a drift-diffusion simulator using Synopsis Sentaurus TCAD software. The detector architecture was still the standard *p-i-n* ddetector with $In_{0.53}Ga_{0.47}As$ buffer and cap layers. The measured quantum efficiency is displayed in Figure 5.23. The QE is similar just beyond the 1.7μm InGaAs cutoff, and although there are dips in the spectrum that correlate with the shape of the optical absorption spectrum, QE remains reasonably high (up to 40% for a 5μm thick absorber layer) all the way out to the 2.58 μm cutoff.

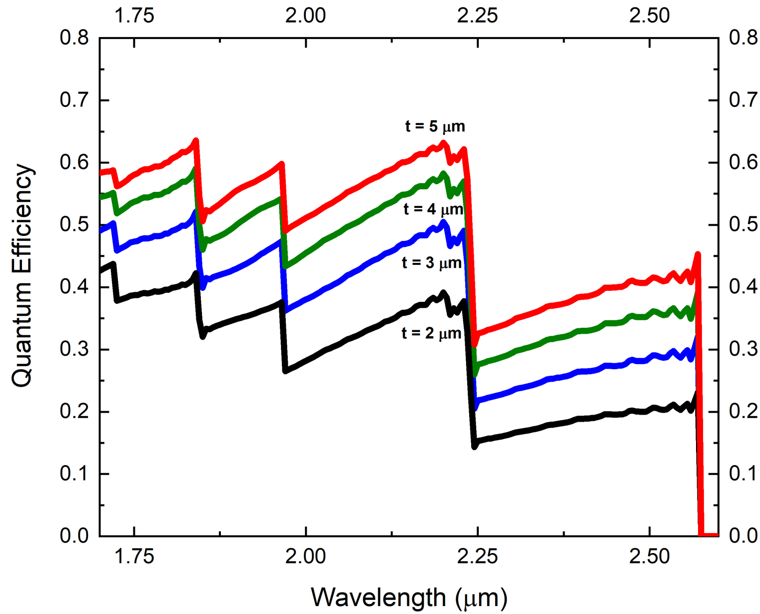

Figure 5.23: Quantum efficiency vs wavelength for the 5 nm $In_{0.50}Ga_{0.50}As$ / 6 nm $GaAs_{0.49}Sb_{0.51}$ SLS system. The quantum efficiency near the cutoff is significantly higher than in the similar, unstrained T2SL case.

Comparisons have been made between lattice matched and SLS systems for effective bandgap, optical absorption, and quantum efficiency, indicating superior performance for the SLS case. Based on the methods used to calculate recombination lifetimes and dark current information, the parameters show no differences between the unstrained and strained cases. However, practically the addition of strain to the system will affect carrier transport and material quality, which will ultimately affect the dark current density as well. This is information that will need to be measured experimentally in future work.

Chapter 6

Conclusions and Future Work

In this overall study, various aspects of carrier transport were measured and simulated to understand their effect on HgCdTe and III-V infrared material systems. The goal is to be able to manipulate these transport properties in an effort to improve the performance of infrared devices across SWIR,MWIR, and LWIR wavelength ranges. This was explored by examining the theory behind various material and transport parameters (Chapters 2 and 5), building those parameters into different device architectures (Chapter 3) and looking at how the transport properties allow for manipulation of device level performance (Chapters 3 and 6).

As discussed in Chapter 1, the primary goal of this study is to identify methods for making IR detectors more cost efficient across multiple technologies. In LWIR detectors, this can be achieved by increasing the device operating temperature, which requires lower dark current densities. Various device architectures are proposed to combat Auger recombination, which is the limiting factor for dark current. In SWIR devices, novel superlattice structures are proposed as a cheaper alternative to expensive SWIR HgCdTe that can also extend to wavelengths beyond standard 1.7μm InGaAs without increasing the dark current density.

In order to study how carrier transport affects plays a role in suppressing Auger re-

combination in LWIR HgCdTe, Hall effect measurements of HgCdTe layers with very low doping densities were made. To interpret and understand these measurements, a detailed description of the relevant material and device parameters was necessary, and that information is contained in Chapter 2. Details of the Auger suppression technique used in the double-layer planar heterojunction devices are described in Chapter 3, along with the Rule 07 metric that is used as a comparison standard for high quality IR detectors across all wavelength ranges.

The Hall effect experiments are described in Chapter 4. Standard van der Pauw Hall measurements were compared against the variable magnetic field Hall effect technique, and the latter produced much more detailed results, specifically for structures including multiple carriers and carrier types. Once the Hall data was compiled, the multi-carrier fitting procedure (MCF) was used in conjunction with Fourier-domain mobility spectrum analysis (FMSA) to extract the carrier density and mobility in each HgCdTe epilayer. Carrier density values of 10^{14} cm^{-3} or lower were extracted, indicating that the layers from Teledyne Imaging Sensors are doped sufficiently low enough to properly observe Auger suppression. Temperature dependence of these values was also studied to verify that results were physical, and low temperature measurements were able to confirm the presence of the integer quantum Hall effect as well, indicating that the HgCdTe layers were of exceptional quality. The mobility of these structures was measured to be extremely high (greater than 200,000 cm^2/Vs), and a detailed mobility study was conducted to understand the physical limits on high mobility in LWIR HgCdTe. Mobility values extracted in these studies are very close to the theoretical maximum values. These experiments indicate that by decreasing the doping level in LWIR HgCdTe, not only is Auger suppression and lower dark current possible, but higher mobility values can be achieved as well, leading to much more efficient and cheaper LWIR detector systems with lower cooling requirements.

The second approach to improving the overall economic viability of infrared devices focuses on the SWIR wavelength range. Chapter 5 details the existing SWIR device technologies, and explains certain gaps in the SWIR wavelength range that can not be accessed without either using expensive SWIR HgCdTe or cheaper III-V devices with significantly lower quality (lower QE and higher dark current). Type-II superlattices are presented as a cost effective alternative that can access wavelengths beyond 1.7μm without significant loss of quality. SWIR superlattices have been studied experimentally in the past, but a detailed theoretical study of specific III-V superlattice materials has not be conducted, and the theoretical limits on performance have not been previously detailed.

Simulations were conducted to understand the optimal device performance of both lattice matched and strained InGaAs/GaAsSb superlattices. Material properties including the quantum well band structure, effective bandgap, absorption coefficient, and minority carrier lifetimes were calculated from first principles via the use of 8 band $\mathbf{k}\cdot\mathbf{p}$ perturbation theory. These parameters were used to calculate device performance characteristics (quantum efficiency and dark current density) under various possible device thicknesses and carrier lifetime situations to understand what potential limits exist for these device architectures.

The lattice matched T2SL structure was shown to have quantum efficiency near 50% out to wavelengths near 2.2 μm, and a dark current density that is comparable to Rule 07 predictions for high quality, radiatively limited material. For the SLS case, there is not enough information at present to understand how the dark current density may change compared to the unstrained case. However, the absorption and quantum efficiency are both significantly improved in the SLS, leading to quantum efficiency near 50% all the way out to the cutoff wavelength of 2.58μm. This illustrates that SWIR T2SL detectors can potentially outperform existing extended range InGaAs,

while leveraging mature III-V fabrication technology to remain a cheaper alternative to SWIR HgCdTe.

The results of both the LWIR and SWIR studies show promising results for future devices that can be both cost effective and exhibit higher performance. Future work in the HgCdTe study should focus on connections between lower doping levels and higher mobility and device level performance such as dark current density, detectivity, and signal to noise ratio. This could create a fully detailed picture of exactly how Auger suppression techniques affect the end result of a device.

Also, decreasing the absorber layer doping is only one of the existing techniques utilized to implement Auger suppression. Structures have been proposed that utilize lower doping as well as nBn barrier architectures in the same device. Detailed theoretical and experimental studies on the effects of combined architectures may provide even further improvements on decreasing the effects of Auger recombination.

For the SWIR superlattice studies, the most critical steps moving forward are to correlate simulations with experimental data. Based on the results of the simulations, the engineers at Princeton Infrared Technologies are planning to fabricate devices in order to make measurements on device level parameters such as quantum efficiency and dark current, as well as material parameters like minority carrier lifetime. The simulations presented offer the maximum theoretical limits on device performance, but an understanding of how current growth and processing techniques affect superlattice properties is still lacking.

Significant research is still ongoing in both Auger suppression in HgCdTe detectors as well as SWIR type-II superlattices with the hope that these devices can show significant performance improvement and decreased manufacturing and operations costs. While HgCdTe is still currently the leading technology for high performance IR detectors across all wavelengths, this study shows that there is a potential for

even greater performance in LWIR devices. It is also seen that there exist application spaces where cheaper SWIR III-V devices like T2SL detectors can operate and thrive, while still maintaining exceptional device performance. These experiments are intended to provide an outline for new devices and applications for the next generation of infrared detector systems.

Bibliography

[1] K. Hyll. *Image-based quantitative infrared analysis and microparticle characterisation for pulp and paper applications.* PhD thesis, King's College London, January 2016.

[2] A. Rogalski. Hgcdte infrared detector material: history, status and outlook. *Rep. Prof. Phys.*, 68:2267, 2005.

[3] R. Hudson. *Infrared System Engineering.* Wiley, 1969.

[4] P. Bhattacharya. *Semiconductor Optoelectronic Devices.* Prentice Hall, 1997.

[5] J. Beletic, R. Blank, D. Gulbransen, D. Lee, M. Loose, et al. Teledyne imaging sensors: infrared imaging technologies for astronomy and civil space. *Proc. SPIE*, 7021, 2008.

[6] A. Rogalski. History of infrared detectors. *Opto-Electron. Rev.*, 20(3):279–308, 2012.

[7] A Itsuno, P Emelie, J Phillips, S Velicu, C Grein, and P Wijewarnasuriya. Arsenic diffusion study in hgcdte for low p-type doping in auger-suppressed photodiodes. *J. Electron. Mater.*, 39(7), 2010.

[8] J Easley, E Arkun, B Cui, M Carmody, L Peng, M Grayson, and J Phillips. Analysis of carrier transport in n-type $hg_{1-x}cd_x te$ with ultra-low doping concentration. *J. Electron. Mater.*, 47(10):5699–5704, 2018.

[9] P Capper. *Properties of Narrow Gap Cadmium-Based Compounds.* INSPEC/IEE, 1994.

[10] C. Jones, K. James, J. Merz, R. Braunstein, M. Burd, M. Eetemadi, S. Hutton, and J. Drumheller. Status of point defects in hgcdte. *J. Vac. Sci. Technol. A*, 3(1), 1985.

[11] P Capper. *Narrow-Gap II-VI Compounds for Optoelectronic and Electromagnetic Applications.* Chapman and Hall, 1997.

[12] A. Rogalski. *Infrared Detectors.* CRC Press, 2000.

[13] W Tennant, D Lee, M Zandian, E Piquette, and M Carmody. Mbe hgcdte technology: A very general solution to ir detection, described by "rule 07", a very convenient heuristic. *J. Electron. Mater.*, 37(9), 2008.

[14] W Tennant. "rule 07" revisited: Still a good heuristic predictor of p/n hgcdte photodiode performance? *J. Electron. Mater.*, 39(7), 2010.

[15] D. Lee et al. High-operating temperature hgcdte: A vision for the near future. *J. Electron. Mater.*, 45(9):4587–4595, 2016.

[16] S Maimon and G Wicks. nbn detector, an infrared detector with reduced dark current and higher operating temperature. *Appl. Phys. Lett.*, 89(151109), 2006.

[17] R Nave. Hall effect. `http://hyperphysics.phy-astr.gsu.edu/hbase/magnetic/Hall.html`. Accessed: 03-13-2019.

[18] Resistivity and hall measurements. https://www.nist.gov/pml/engineering-physics-division/popular-links/hall-effect/resistivity-and-hall-measurements. Accessed: 03-13-2019.

[19] M Gold and D Nelson. Variable magnetic field hall effect measurements and analyses of high purity, hg vacancy (p-type) hgcdte. *J. Vac. Sci. Technol. A*, 4(4), 1986.

[20] B Cui, Y Tang, and M Grayson. Introducing fourier-domain mobility spectrum analysis (fmsa) to deduce multi-component carrier mobility and density. *Proc. of SPIE*, 9370, 2015.

[21] J. Easley, E. Arkun, M. Carmody, and J. Phillips. Variable-field hall effect analysis of hgcdte epilayers with very low doping density. *J. Electron. Mater.*, 46(9):5479–5483, 2017.

[22] T. Martin, R. Brubaker, P. Dixon, M.A. Gagliardi, and T. Sudol. 640x512 ingaas focal plane array camera for visible and swir imaging. *Proc. of SPIE*, 5783, 2005.

[23] W. Lei, J. Antoszewski, and L. Faraone. Progress, challenges, and opportunities for hgcdte infrared materials and detectors. *Appl. Phys. Rev.*, 2(041303), 2015.

[24] X. Hu et al. Large format high snr swir hgcdte/si fpa with multiple-choice gain for hyperspectral detection. *Proc. of SPIE*, 10213, 2017.

[25] E. Plis. Inas/gasb type-ii superlattice detectors. *Advances in Electronics*, 2014, 2014.

[26] C Grein, P Young, M Flatte, and H Ehrenreich. Long wavelength inas/ingasb infrared detectors: Optimization of carrier lifetimes. *J. Appl. Phys.*, 78(12), 1995.

[27] P.Y. Emelie. *HgCdTe Auger-Suppressed Infrared Detectors Under Non-Equilibrium Operation*. PhD thesis, University of Michigan, 2009.

[28] H. Inada et al. Recent development of swir focal plane array with ingaas/gaassb type-ii quantum wells. *Proc. SPIE*, 9819, 2016.

[29] J. Easley, C. R. Martin, M. H. Ettenberg, and J. D. Phillips. Ingaas/gaassb type ii superlattices for swir detection. *J. Electron. Mater.*, 2019. Submitted.

[30] Y. Arslan, F. Oguz, and C. Besikci. Extended wavelength swir ingaas focal plane array: Characteristics and limitations. *Infrared Phys. Technol*, 70, 2015.

[31] M. Kinch. *Fundamentals of Infrared Detectors*. SPIE Press, 2007.

[32] R. Pierret. *Semiconductor Device Fundamentals*. Pearson, 1996.

[33] B Olson, C Grein, J Kim, E Kadlec, J Klem, S Hawkins, and Shaner E. Auger recombination in long-wave infrared inas/inassb type-ii superlattices. *Appl. Phys. Lett.*, 107, 2015.

[34] M Kinch. The future of infrared; iii-vs or hgcdte? *J. Electron. Mater.*, 44(9), 2015.

[35] A Itsuno, J Phillips, and S Velicu. Predicted performance improvement of auger-suppressed hgcdte photodiodes and p-n heterojunction detectors. *IEEE Trans. Electron Devices*, 58(2):501–507, 2011.

[36] V Srivastav, R Pal, and V Venkataraman. Performance study of high operating temperature hgcdte mid wave infrared detector through numerical modeling. *J. Appl. Phys.*, 108, 2010.

[37] P Norton. Hgcdte infrared detectors. *Opto-Electron. Rev*, 10(3), 2002.

[38] E.C. Piquette, W. McLevige, J. Auyeung, and A. Wong. Progress in development of h4rg-10 infrared focal plane arrays for wfirst-afta. *Proc. of SPIE*, 9154, 2014.

[39] Y. Chang, C. Fulk, J. Zhao, C.H. Grein, and S. Sivananthan. Molecular beam epitaxy growth of hgcdte for high performance infrared photon detectors. *Infrared Phys. Technol*, 50, 2007.

[40] J. Phillips, D. Edwall, D. Lee, and J. Arias. Growth of hgcdte for long-wavelength infrared detectors using automated control from spectroscopic ellipsometry measurements. *J. Vac. Sci. Technol. B*, 19:1580–1584, 2001.

[41] S. Price and P. Boyd. Overview of compositional measurement techniques for hgcdte with emphasis on ir transmission, energy dispersive x-ray analysis and optical reflectance. *Semicond. Sci. Technol.*, 8, 1993.

[42] S. Shin, J. Arias, M. Zandian, J. Pasko, and R. DeWames. Effect of the dislocation density on minority-carrier lifetime in molecular beam epitaxial hgcdte. *Appl. Phys. Lett.*, 59(21), 1991.

[43] A. Szilagyi and M. Grimbergen. Misfit and threading dislocation in hgcdte epitaxy. *J. Vac. Sci. Technol. A*, 4(4), 1986.

[44] H. Schaake and J. Tregilgas. Precipitation of tellurium in hgcdte alloys. *J. Electron. Mater.*, 12(6), 1983.

[45] Wijewarnasuriya and S Sivananthan. Arsenic incorporation in hgcdte grown by molecular beam epitaxy. *Appl. Phys. Lett.*, 72(14), 1998.

[46] G Hansen, J Schmidt, and T Casselman. Energy gap versus alloy composition and temperature in hgcdte. *J. Appl. Phys.*, 53(10), 1982.

[47] M.H. Weiler. *Semiconductors and Semimetals*. Academic Press, 1981.

[48] R. Dornhaus, G. Nimtz, and B. Schlict. *Narrow-Gap Semiconductors*. Springer Verlag, 1983.

[49] J. Wenus, J. Rutkoswki, and A. Rogalski. Two-dimensional analysis of double-layer heterojunction hgcdte photodiodes. *IEEE Trans. Electron Devices*, 48(7), 2001.

[50] G.L. Hansen and J.L. Schmit. Calculation of intrinsic carrier concentration in hgcdte. *J. Appl. Phys.*, 54(4), 1983.

[51] B.A. Bernevig, T.L. Hughes, and S. Zhang. Quantum spin hall effect and topological phase transition in hgte quantum wells. *Science*, 314, 2006.

[52] M. Konig et al. Quantum spin hall insulator state in hgte quantum wells. *Science*, 318, 2007.

[53] W. Scott. Electron mobility in $hg_{1-x}cd_xte$. *J. Appl. Phys.*, 43(3), 1972.

[54] P.N.J. Dennis and C.T. Elliott. A method for routine characterisation of the hole concentration in p-type cadmium mercury telluride. *Infrared Phys.*, 22, 1982.

[55] E. Finkman and S.E. Schacham. The exponential optical absorption band tail of $hg_{1-x}cd_xte$. *J. Appl. Phys.*, 56, 1984.

[56] C.A. Hougen. Model for infrared absorption and transmission of liquid-phase epitaxy hgcdte. *J. Appl. Phys.*, 66, 1989.

[57] K Moazzami, J Phillips, D Lee, D Edwall, M Carmody, Piquette, M Zandian, and J Arias. Optical-absorption model for molecular-beam epitaxy hgcdte and application to infrared detector photoresponse. *J. Electron. Mater.*, 33(6), 2004.

[58] A. M. Itsuno. *Bandgap-Engineered HgCdTe Infrared Detector Structures for Reduced Cooling Requirements*. PhD thesis, University of Michigan, 2012.

[59] B. Van Zeghbroeck. *Principles of Semiconductor Devices*. Prentice Hall, 2011.

[60] X Ji et al. 2.6 μm mbe grown ingaas detectors with dark current of srh and tat. *AIP Advances*, 4, 2014.

[61] T.N. Casselman. Calculation of the auger lifetime in p-type $hg_{1-x}cd_x te$. *J. Appl. Phys.*, 52, 1981.

[62] C.M. Ciesla et al. Auger recombination dynamics of $hg_{0.795}cd_{0.205}te$ in the high excitation regime. *Appl. Phys. Lett.*, 71, 1997.

[63] A.R. Beattie and P.T. Landsberg. Auger effect in semiconductors. *Proc. R. Soc. Lond. A Math. Phys. Sci.*, 249, 1959.

[64] A Slonopas and D Tomkinson. Study of the natural auger suppression mechanism in heterostructures through heteroboundary engineering. *J. Phys. Chem. a*, 121(40), 2017.

[65] P Zimmermann, M Reine, K Spignese, K Maschhoff, and J Schirripa. Surface passivation of hgcdte photodiodes. *J. Vac. Sci. Technol. A*, 8(2), 1990.

[66] D Ting, A Soibel, A Khoshakhlagh, and S Gunapala. Theoretical analysis of nbn infrared photodetectors. *Opt. Eng.*, 59(9), 2017.

[67] D Sidor et al. Mbe growth techniques for inas-based nbn ir detectors. *J. Vac. Sci. Technol. B*, 35(2), 2017.

[68] A Itsuno, J Phillips, and S Velicu. Mid-wave infrared hgcdte nbn photodetector. *Appl. Phys. Lett.*, 100(161102), 2012.

[69] N Akhavan, G Jolley, G Umana-Membreno, J Antoszewski, and L Faraone. Theoretical study of midwave infrared hgcdte nbn detectors operating at elevated temperatures. *J. Electron. Mater.*, 44(9), 2015.

[70] E Aifer et al. W-structured type-ii superlattice long-wave infrared photodiodes with high quantum efficiency. *Appl. Phys. Lett.*, 89(053519), 2006.

[71] M Razeghi et al. Recent advances in lwir type-ii inas/gasb superlattice photodetectors and focal plane arrays at the center for quantum devices. *Proc. IEEE*, 97(6), 2009.

[72] E Plis et al. Mid-infrared inas/gasb strained layer superlattice detectors with nbn design grown on a gaas substrate. *Semicond. Sci. Technol.*, 25(085010), 2010.

[73] D.D. Edwall, M. Zandian, A.C. Chen, and J.M. Arias. Improving material characteristics and reproducibility of mbe hgcdte. *J. Electron. Mater.*, 26(6), 1997.

[74] P.S. Wijewarnasuriya, M.D. Langer, S. Sivananthan, and J.P. Faurie. Analysis of low doping limitation in molecular beam epitaxially grown hgcdte(211)b epitaxial layers. *J. Electron. Mater.*, 24(9), 1995.

[75] L van der Pauw. A method of measuring specific resistivity and hall effect of discs of arbitrary shape. *Philips Tech. Rev.*, 20, 1958.

[76] L van der Pauw. A method of measuring the resistivity and hall coefficient on lamellae of arbitrary shape. *Philips Tech. Rev.*, 20(8), 1959.

[77] J Meyer, C Hoffman, F Bartoli, D Arnold, S Sivananthan, and J Faurie. Methods for magnetotransport characterization of ir detector materials. *Semicond. Sci. Technol.*, 8, 1993.

[78] J Kim, D Seller, and W Tseng. Multicarrier characterization method for extracting mobilities and carrier densities of semiconductors from variable magnetic field measurements. *J. Appl. Phys.*, 73(12), 1992.

[79] W Beck and J Anderson. Determination of electrical transport properties using a novel magnetic field-dependent hall technique. *J. Appl. Phys.*, 73(12), 1992.

[80] J Antoszewski, D Seymour, L Faraone, J Meyer, and C Hoffman. Magneto-transport characterization using quantitative mobility-spectrum analysis. *J. Electron. Mater.*, 24(9), 1995.

[81] I Vurgaftman et al. Improved quantitative mobility spectrum analysis for hall characterization. *J. Appl. Phys.*, 84(9), 1998.

[82] B Cui and M Grayson. Background subtraction in fourier-domain mobility spectrum analysis for resolving low-mobility carriers. *Proc. of SPIE*, 10111, 2017.

[83] A Ramadan, R Gould, and A Ashour. On the van der pauw method of resistivity measurements. *Thin Solid Films*, 239, 1994.

[84] J Rosbeck, R Starr, S Price, and K Riley. Background and temperature dependent current-voltage characteristics of hgcdte photodiodes. *J. Appl. Phys.*, 53(9), 1982.

[85] R Stratton. The effect of free electrons on lattice conduction at high temperatures. *Phil. Mag.*, 2(15), 1957.

[86] D Tong. Lectures on the quantum hall effect. *arXiv*, 2016. Accessed: 03-18-2019.

[87] A.M. Joshi, G.H. Olsen, S.M. Mason, M. Kazakia, and V.S. Ban. Near-infrared [1-3 micron] ingaas detectors and arrays - crystal growth leakage current and reliability. *Proc. SPIE 1715*, 585, 1993.

[88] R.W.M Hoogeveen et al. Extended wavelength ingaas infrared [1.0-2.4 μm] detector arrays on sciamachy for space-based spectrometry of the earth atmosphere. *InPhT*, 42, 2001.

[89] I. Vurgaftman, J.R. Meyer, and L.R. Ram-Mohan. Band parameters for iii-v compound semiconductors and their alloys. *J. Appl. Phys.*, 89(11), 2001.

[90] J.P. Vermeiren and P. Merken. Ingaas detectors and fpa's for a large span of applications: design and material considerations. *Proc. of SPIE*, 10563, 2014.

[91] L. Zhou et al. Dark current characteristics of gaas-based 2.6 μm ingaas photodetectors on different types of inalas buffer layers. *J. Phys. D Appl. Phys.*, 47(8), 2014.

[92] G Dohler. Solid-state superlattices. *Sci. Am.*, 249(5), 1983.

[93] Y. Huang et al. Strain-balanced inas/gasb type-ii superlattice structures and photodiodes grown on inas substrates by metalorganic chemical vapor deposition. *Appl. Phys. Lett.*, 99(011109), 2011.

[94] J.B. Rodriguez, P. Christol, L. Cerutti, F. Chevrier, and A. Joullie. Mbe growth and characterization of type-ii inas/gasb superlattices for mid-infrared detection. *J Cryst Growth*, 274, 2005.

[95] Y. Huang et al. Proposal for strained type ii superlattice infrared detectors. *J. Appl. Phys.*, 62(6), 1987.

[96] H. Inada, M. Miura, Y. Nagai, Y. Iguchi, and Y. Kawamura. Uncooled swir ingaas/gaassb type ii quantum wells focal plane array. *Proc. SPIE*, 7660, 2010.

[97] B. Chen, W. Jiang, J. Yuan, A. L. Holmes, and B. Onat. Swir/mwir inp-based p-i-n photodiodes with ingaas/gaassb type-ii quantum wells. *IEEE J. Quantum Electron*, 47(9), 2011.

[98] N. Cohen and O. Aphek. Extended wavelength swir detectors with reduced dark current. *Proc. SPIE*, 2015.

[99] T. Kawahara et al. Ingaas/gaassb type-ii quantum-well focal plane array with cutoff-wavelength of 2.5 μm. *Proc. SPIE*, 10111, 2017.

[100] C. Jin, J. Chen, Q. Xu, C. Yu, and L. He. Electrical and optical performances of ingaas/gaassb superlattice short-wavelength infrared detectors. *Opt. Eng.*, 56(5), 2017.

[101] Y. Uliel, D. Cohen-Elias, N. Sicron, I. Grimberg, N. Snapi, Y. Paltiel, and M. Katz. Ingaas/gaassb type-ii superlattice based photodiodes for short wave infrared detection. *Infrared Phys. Technol*, 84, 2017.

[102] P. Sengupta, H. Ryu, S. Lee, Y. Tan, and G. Klimeck. Numerical guidelines for setting up a general purpose k.p simulator with applications to quantum dot heterostructures and topological insulators. *arXiv*, 2014. Accessed: 04-04-2019.

[103] S. Birner. *Modeling of semiconductor nanostructures and semiconductor-electrolyte interfaces*. PhD thesis, Technische Universitat Munchen, November 2011.

[104] D. Miller. Optical physics of quantum wells. `https://ee.stanford.edu/~dabm/181.pdf`. Accessed: 04-04-2019.

[105] L. Esaki and R. Tsu. Superlattice and negative differential conductivity in semiconductors. *IBM J. Res. Develop.*, 14(61), 1970.

[106] B. Chen. *InP Based Type-II Quantum Wells PIN Photodiodes*. PhD thesis, University of Virginia, May 2013.

[107] B.V. Olson et al. Vertical hole transport and carrier locatlization in inas/inassb type-ii superlattice heterojunction bipolar transistors. *Phys. Rev. Applied*, 7, 2017.

[108] G.A. Umama-Membreno, B. Klein, H. Kala, J. Antoszewski, N. Gautam, M.N. Kutty, E. Plis, S. Krishna, and L. Faraone. Vertical minority carrier electron transport in p-type inas/gasb type-ii superlattices. *Appl. Phys. Lett.*, 101(253515), 2012.

[109] D. Benyahia, L. Kubiszyn, K. Michalczewski, J. Boguski, A. Keblowski, P. Martyniuk, J. Piotrowski, and A. Rogalski. Electrical properties of midwave and longwave inas/gasb superlattices grown on gaas substrates by molecular beam epitaxy. *Nanoscale Res. Lett.*, 13(196), 2018.

[110] S. Franceschi, J. Jancu, and F. Beltram. Boundary conditions in multiband k.p models: A tight-binding test. *Phys. Rev. B*, 59(15), 1991.

[111] X. Ji et al. Deep-level traps induced dark currents in extended wavelength ingaas/inp photodetector. *J. Appl. Phys.*, 114(224502), 2013.

[112] N.J. Ekins-Daukes, K. Kawaguchi, and J. Zhang. Strain-balanced criteria for multiple quantum well structures and it's signature in x-ray rocking curves. *Cryst. Growth Des.*, 2(4), 2002.

[113] J. Hwang and J.D. Phillips. Band structure of strain-balanced gaasbi/gaasn superlattices on gaas. *Phys. Rev. B*, 83(195327), 2011.

[114] S.M. Hu. Misfit dislocations and critical thickness of heretoepitaxy. *J. Appl. Phys.*, 69(7901), 1991.

[115] J.W. Matthews and A.E. Blakeslee. Defects in epitaxial multilayers i. misfit dislocations. *J. Cryst. Growth*, 27, 1974.